Vol. 22 No. 01
March 2025

p-ISSN 1412-2960
e-ISSN 2579-521X

Indonesian Physics Communication

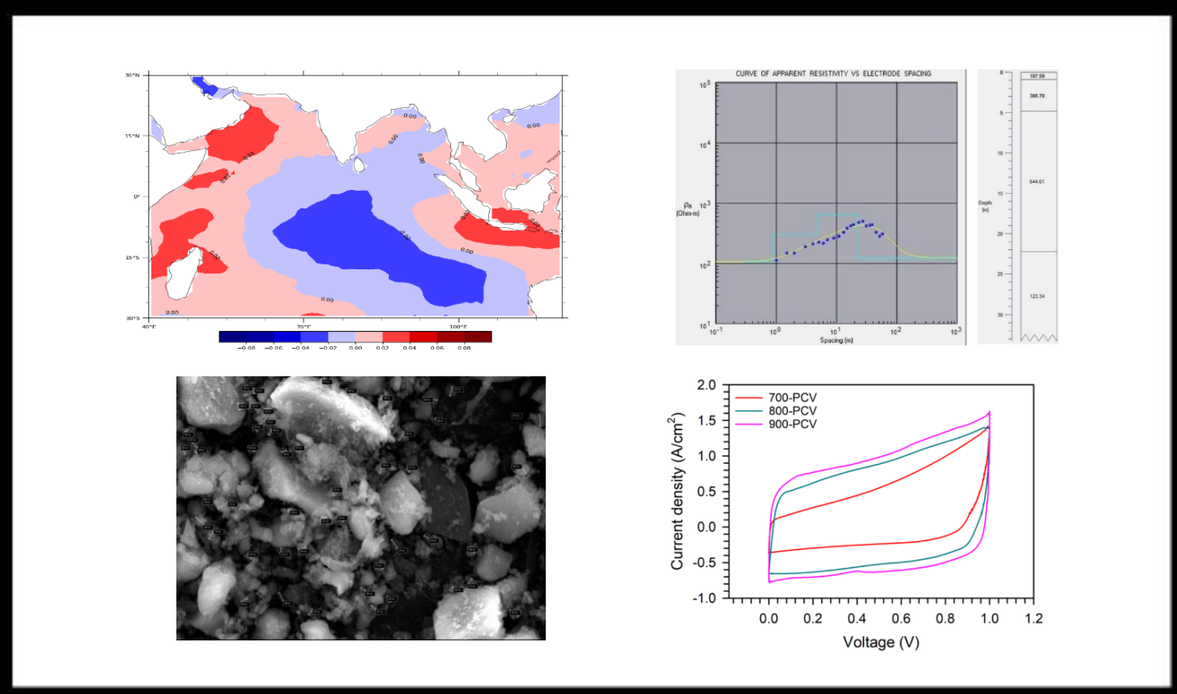

ISSN 1412 2960

Indonesian Physics Communication
Vol. 22 No. 01
March 2025
Department of Physics, Universitas Riau
Pekanbaru

Department of Physics
Faculty of Mathematics and Natural Sciences
Universitas Riau
Kampus Bina Widya Jl. HR. Soebrantas Km. 12.5
Simpang Baru Panam, Pekanbaru 28293

Vol. 22 No. 01
March 2025

p-ISSN 1412-2960
e-ISSN 2579-521X

Indonesian Physics Communication

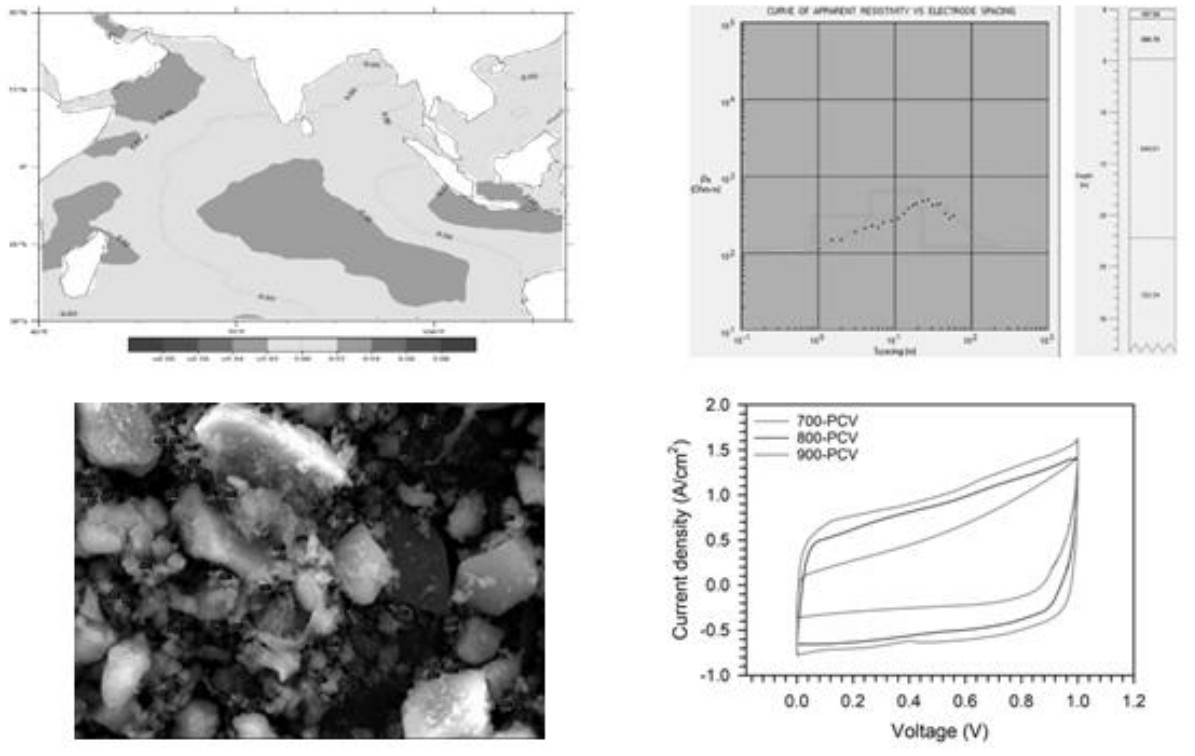

Department of Physics
Faculty of Mathematics and Natural Sciences
Universitas Riau
Kampus Bina Widya Jl. HR. Soebrantas Km. 12.5
Simpang Baru Panam, Pekanbaru 28293

Indonesian Physics Communication
Department of Physics, Universitas Riau, Pekanbaru, Indonesia
p-ISSN 1412-2960 | e-ISSN 2579-521X
Web: https://kfi.ejournal.unri.ac.id
E-mail: kfi@ejournal.unri.ac.id

Editorial Board of the Indonesian Physics Communication (IPC) Journal
Department of Physics, Faculty of Mathematics and Natural Sciences, Universitas Riau

Editorial Address:

Department of Physics, Faculty of Mathematics and Natural Sciences, Universitas Riau
Kampus Bina Widya Km 12.5 Simpang Baru Pekanbaru
Homepage: https://kfi.ejournal.unri.ac.id/index.php/JKFI
E-mail: kfi@ejournal.unri.ac.id

LIST OF CONTENTS

IPC

Indonesian Physics Communication

Department of Physics, Universitas Riau, Pekanbaru, Indonesia
p-ISSN 1412-2960 | e-ISSN 2579-521X

Vol. 22 | No. 1
March 2025

Web: https://kfi.ejournal.unri.ac.id
E-mail: kfi@ejournal.unri.ac.id

Volumetric-gravimetric synergy in biomass-derived carbon supercapacitors: A case study on dried banana leaf waste

Apriwandi
Department of Physics, Universitas Riau, Pekanbaru 28293, Indonesia

Corresponding author: apriwandi@lecturer.unri.ac.id

ABSTRACT

Biomass-derived carbon-based supercapacitors are a compelling solution for environmentally friendly electrochemical energy storage, playing a crucial role in the transition to sustainable energy. Despite this potential, much of the existing research has overly concentrated on theoretical evaluations, hindering practical application. This study decisively addresses the performance of supercapacitors on both a volumetric and practical scale, underscoring their global applicability. The carbon material utilized in this research was expertly produced from dried banana leaf biomass, converted into solid carbon through a process of chemical activation with NaOH and high-temperature pyrolysis. The pyrolysis was carried out in an integrated fashion, combining carbonization and physical activation stages within a carbon dioxide (CO_2) gas atmosphere at temperatures of 700°C, 800°C, and 900°C. Initial characterization focused on density analysis to assess the structural integrity of the porous carbon electrodes. Electrochemical performance was rigorously evaluated using cyclic voltammetry (CV) for volumetric capacitance and galvanostatic charge-discharge (GCD) for gravimetric capacitance within a two-electrode system using a 1000 mmol/L Na_2SO_4 electrolyte. The results are compelling: the carbon material activated at 900°C achieved an exceptional volumetric capacitance of 198 F/cm³ and a gravimetric capacitance of 181 F/g. These results clearly demonstrate that banana leaf-derived activated carbon is not only viable but also a highly promising electrode material for supercapacitors, paving the way for practical applications in the field.

Keywords: Biomassa; carbon; gravimetric performance; supercapacitor; volumetric performance

Received 20-02-2025 | Revised 12-03-2025 | Accepted 23-03-2025 | Published 31-03-2025

INTRODUCTION

Supercapacitors have emerged as one of the most promising energy storage technologies due to their advantages, including high power density, long cycle life, and fast charge/discharge times. Unlike conventional batteries, which rely on electrochemical reactions to store energy, supercapacitors utilize electric double-layer capacitance and pseudocapacitive reactions for energy storage [1, 2]. The performance of supercapacitors is significantly influenced by the choice of electrode materials. Recently, research has focused on natural-based carbons because of their abundant availability, sustainability, and capability to be synthesized into porous structures with high surface areas [3, 4]. However, most studies tend to concentrate on gravimetric-scale evaluations, often neglecting the important volumetric aspect, which is critical for practical applications, particularly in miniaturized devices and energy storage systems with limited space.

Natural-based carbons, such as activated carbon derived from biomass, graphene, and cellulose-based carbons, have garnered extensive attention in supercapacitor applications [5, 6]. For instance, a study by Liu et al. (2023) demonstrated that carbon obtained from agricultural waste, such as rice husk and oil branch, can be transformed into high-porosity electrode materials using potassium hydroxide (KOH)-based chemical activation [7, 8]. This research revealed that materials with high specific surface areas could achieve a specific capacitance of 320 F/g; however, their energy density on a volumetric scale was still

limited due to an uncontrolled porous structure. Meanwhile, Shao et al. (2022) successfully synthesized carbon from peanut shell waste using a hydrothermal method followed by activation with $ZnCl_2$ [9]. This approach resulted in a material with better volumetric energy density compared to conventional methods. The findings confirmed that engineering the pore structure is crucial for optimizing the volumetric performance of supercapacitors. Another study by Wang et al. (2023) highlighted that combining heteroatom doping with a nano-hierarchical pore structure could significantly enhance volumetric capacitance [10]. The researchers found that doping nitrogen and boron into the carbon matrix derived from palm fiber improved electronic conductivity and provided additional pseudocapacitance, leading to an increase in specific capacitance up to 450 F/g. Furthermore, a study by Kim et al. (2024) demonstrated that marine algae-based carbon could be developed into a high-volumetric-density electrode material using a compression-densification technique [11]. This method resulted in a volumetric energy density of 25 Wh/L while maintaining excellent cycle stability.

Evaluating the performance of supercapacitors at a volumetric scale is crucial in various practical applications, including electric vehicles, flexible electronic devices, and portable energy storage systems [12, 13]. Many studies focus on gravimetric capacitance while overlooking the space limitations in real-world applications. For instance, although graphene-based carbon boasts a very high surface area and excellent electrochemical performance, it often has a low density, which restricts its volumetric energy density [14, 15]. To address these challenges, innovative approaches in carbon structure engineering [16], such as compression techniques, hybrid coatings [17], and heteroatom doping [18], have emerged as promising strategies to enhance volumetric performance without sacrificing the electrochemical characteristics of the materials. As the demand for more efficient and compact energy sources increases, the volumetric performance of supercapacitors warrants further exploration [9, 19]. While numerous studies have tackled the optimization of natural material-based carbon for supercapacitor applications, there remains a gap in strategies specifically designed to improve volumetric performance.

This study aims to fill this gap by systematically analyzing the latest methods in carbon structure optimization, synthesis techniques aimed at increasing volumetric energy density, and the effects of morphology engineering and heteroatom doping on the overall performance of supercapacitors. This research focuses on utilizing banana leaf waste as the carbon source, synthesized through a novel sodium hydroxide (NaOH) chemical catalyst in a bi-atmosphere gas integrated pyrolysis system. By gaining a deeper understanding of the electrochemical evaluation of these factors, the study aims to develop new strategies for designing natural carbon-based electrode materials that achieve both high specific capacitance and optimal volumetric energy density for future applications.

MATERIAL AND METHOD

Synthesis of Banana Leaf-Derived Solid Carbon Using Chemical Catalysts

This investigation approach involves synthesizing solid carbon using chemical catalysts derived from dried banana leaf biomass waste collected from traditional plantations in the Pekanbaru area. The process begins with thoroughly washing the banana leaves to remove any contaminants. Next, the leaves are cut into smaller pieces and dried for two days in open air conditions. After drying, the precursor material undergoes pre-carbonization in an oven at 200°C for 240 minutes to reduce volatile content and enhance the stability of the carbon structure. The results of the pre-carbonization are then ground and refined to achieve a uniform particle size of less than 60 μm.

The chemical activation process utilizes a NaOH solution at a concentration of 500 mmol/g, which is evenly mixed with the pre-carbonized powder. This mixture is stirred on a hotplate stirrer at a temperature of 78°C – 81°C and a rotation speed of 300 rpm to ensure homogeneous catalyst distribution. Once mixing is complete, the sample is dried in an oven at 90 °C to remove excess solvent, producing a precursor that is ready for the next stage.

The resulting activated carbon powder is then formed into a monolith using a hydraulic press mold at a pressure of 8 metric tons. The pyrolysis process consists of a single stage that includes both carbonization and physical activation. Carbonization occurs at a temperature of 600°C in a nitrogen gas atmosphere (N_2) to prevent uncontrolled oxidation, while physical activation is conducted by exposing the material to carbon dioxide gas (CO_2) for 250min in 700, 800, and 900°C to enhance the surface area and develop an optimal pore structure.

The final step of this methodology involves fabricating a supercapacitor cell in a coin configuration. The electrodes are made from the synthetic carbon created from banana leaf waste, and the electrolyte used is a sodium sulfate solution (Na_2SO_4) with a concentration of 1 mol/L. Additional components of the supercapacitor cell include a stainless-steel current collector and a separator made from duck eggshell membrane. The entire synthesis and assembly process of the supercapacitor cell is designed to produce carbon materials with optimal electrochemical properties, thereby improving energy storage performance in supercapacitor applications.

Precursor Density Characteristics

The evaluation of solid carbon designs prepared without external adhesives demonstrated their significant density properties. We conducted a thorough examination of density behavior by measuring the mass, diameter, and thickness of the precursors. This dimensional data allowed for precise calculation of precursor density using the standard density formula widely recognized in the field [20]. Additionally, we rigorously analyzed dimensional changes during the bi-atmosphere pyrolysis process.

Preparation of Working Electrodes and Supercapacitor Cells

This effectively fabricated the working electrodes as thin cylinders with dimensions of 9 mm in diameter and 0.2 mm in thickness, ensuring each electrode maintained a consistent loading mass of 9 mg. The assembly of the test cells was executed without the need for any additional conductive materials or adhesives. The supercapacitor cells were strategically assembled in a symmetrical configuration, comprising two electrodes separated by a thin membrane. A robust stainless steel current collector, supported by a polymer glass cell body, was utilized to enhance performance.

Supercapacitor Cell Performance

We assessed the electrochemical properties of the solid carbon-based supercapacitor cell, derived from dried banana leaves, using both theoretical and practical approaches through advanced techniques such as cyclic voltammetry (CV) and galvanostatic charge-discharge (GCD). These measurements were conducted in a 1 mol/L Na_2SO_4 electrolyte solution, ensuring accuracy. The volumetric electrochemical properties—including capacitance, energy, and power—were meticulously calculated using established general formulas [21, 22].

RESULTS AND DISCUSSION

Density-Porosity Analysis

Changes in porosity of prepared carbon materials are crucial for enhancing the performance of supercapacitors. However, traditional methods for evaluating porosity can

lead to a decrease in material density, ultimately reducing its effectiveness in industrial applications [23]. Therefore, a balanced evaluation is necessary, considering both porosity and volumetric density to ensure that the resulting carbon material retains its optimal density without compromising its pore characteristics. In this work, the carbon material was designed to have high porosity while still maintaining sufficient density to ensure electrode efficiency in practical applications.

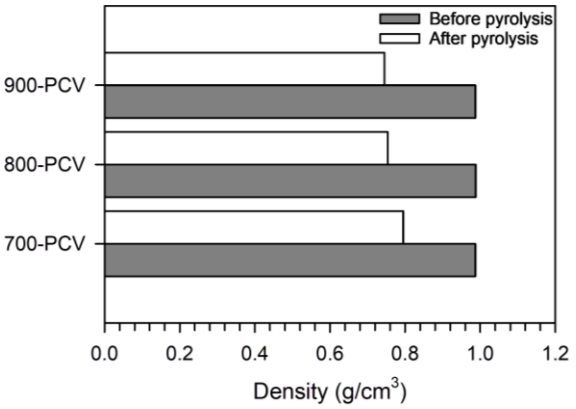

Figure 1. Density of x-PCV.

The formation of porosity in the carbon material was achieved by maintaining a solid state during the pyrolysis and activation stages using NaOH in a horizontal furnace. Prior to thermal treatment, the x-PCV precursor material had a density close to 1 g/cm³. After pyrolysis and activation, the material retained a solid cylindrical form, with a density reduction ranging from 10% to 12%. This decrease is primarily due to the chemical reactions occurring during the activation process with NaOH, carbonization in a nitrogen atmosphere, and physical activation in carbon dioxide gas [24]. The reaction between NaOH and carbon leads to structural degradation, contributing to pore formation, while physical activation interacts with the material's surface and expands its pore structure, resulting in an overall decrease in density [25]. During the pyrolysis process, volatile compounds, minerals, and moisture present in the precursors evaporate, directly affecting the changes in the monolithic dimensions of the material, including mass, volume, and density [26, 27]. The 40 samples were treated for each parameter variation, with carbonization and physical activation conducted in one stage using NaOH as a chemical activator and activation temperatures of 700°C, 800°C, and 900°C. The results indicated that all samples experienced a reduction in density after pyrolysis, which became more pronounced as the physical activation temperature increased. As the temperature rose from 700°C to 900°C, there was a consistent decrease in density, explainable by two main mechanisms. First, during carbonization from room temperature to approximately 600°C, complex organic compounds such as hemicellulose, cellulose, and lignin decompose into pure carbon [28, 29]. While carbonization increases the carbon content of the material, the solid tar generated can clog the pores that are beginning to form, necessitating further activation [29]. Second, physical activation at temperatures exceeding 600°C in a CO_2 atmosphere removes the tar that blocks the pores and enlarges the pore structure by eroding carbon atoms from the material's surface, leading to a further reduction in density. Experimental analysis shows that materials subjected to chemical activation with NaOH can experience a decrease in density of up to 10% to 12%, highlighting NaOH's role in increasing porosity. Additionally, raising the physical activation temperature significantly affects the final density of the material. The recorded density reduction values were 9.7%, 12.3%, and 12.4% for samples activated at 700-PCV, 800-PCV, and 900-PCV, respectively. This phenomenon can be attributed to the reaction between carbon and NaOH that produces carbonate compounds at around 600°C [30]. As the temperature increases further, the carbonate decomposes, leaving voids that form microscopic pores. Consequently, increasing the activation temperature from 700°C to 900°C results in a more developed pore structure, but with a corresponding decrease in density. After the pyrolysis process, the densities of the resulting carbon monoliths were 0.8650 g/cm³ for 700-PCV, 0.8544 g/cm³ for 800-PCV, and 0.8501

g/cm³ for 900-PCV. These results align with previous studies using different biomass precursors, such as *Syzygium oleana* leaves [31] and coconut fiber [32], which reported a trend of decreasing density due to similar carbonization and activation processes. Thus, this mechanism can be considered a general approach for processing biomass into porous carbon materials with adjustable density for supercapacitor applications.

The results of this analysis highlight the crucial role that the combination of chemical and physical activation plays in determining the porosity and density properties of carbon materials. Activation with NaOH effectively enhances porosity by inducing chemical reactions within the carbon structure. Meanwhile, physical activation at high temperatures further enlarges the pores by removing carbonization residues.

While increasing the activation temperature can expand the pore structure, it may also lead to a decrease in the material's density. This trade-off is important to consider for the practical applications of supercapacitors. Therefore, achieving a balance between porosity and density should be a primary focus in the design of supercapacitor electrode materials to ensure optimal performance in industrial applications.

Volumetric Scale Analysis

The previously discussed density-porosity properties were evaluated in the context of their electrochemical behaviors on a volumetric scale. This analysis utilized a cyclic voltammetry approach at a graded scan rate. The x-PCV carbon-based electrode, prepared in a symmetrical configuration, was tested using cyclic voltammetry at a scan rate of 1 mV/s in a 1000 mmol/L sulfuric acid electrolyte medium, as shown in Figure 2 (a). The cyclic voltammogram of the x-PCV carbon electrode exhibited a typical rectangular profile with minimal perturbation, indicating that the charge storage mechanism was dominated by electric double-layer capacitance, with low pseudocapacitive effects observed [33].

The area enclosed by the cyclic voltammogram reflects the volumetric performance per unit area. Additionally, the 700-PCV electrode showed the smallest cyclic area, with an almost linear current increase, confirming the predominance of the capacitive charge storage mechanism and very low faradaic effects. This behavior can be attributed to the presence of oxygen functional groups naturally occurring in biomass-based carbon [34]. Carbon derived from natural materials through pyrolysis tends to bind oxygen in its carbon chain, which can disrupt the cyclic voltammogram profile of natural carbon-based supercapacitors. This oxygen functionality primarily arises from the oxidation process that occurs during the pyrolysis and activation stages in carbon synthesis from biomass. As the physical activation temperature increases from 700°C to 900°C, the current spike in the voltammogram gradually weakens, reflecting a decrease in oxygen functional content and a diminishing pseudocapacitance effect. This reduction in oxygen content is due to the high pyrolysis temperature, which causes the decomposition and evaporation of non-carbon components, thereby increasing the carbon purity. These findings align with the previously discussed density analysis, which indicates that a rise in physical activation temperature leads to a gradual decrease in density [35]. Moreover, the enclosed area in the voltammogram confirms the volumetric specific capacitance of the x-PCV carbon electrode. The 900-PCV electrode has the largest covered area, followed by the 800-PCV and 700-PCV electrodes. This indicates that volumetric capacitance increases with higher activation temperatures. Based on calculations using the standard equation, the volumetric capacitance for each electrode is 119, 176, and 198 F/cm³, respectively. Notably, the application of NaOH as a chemical catalyst and the increase in physical activation temperature for banana leaf waste-based materials successfully raised the volumetric capacitance from 119 F/cm³ to 198 F/cm³. This

capacitance increase is attributed to changes in the physical properties of the sample resulting from the NaOH catalytic treatment and variations in physical activation temperature. Several studies have shown that NaOH can alter the surface morphology to become more porous, increase carbon content, and reduce both heteroatom content and oxygen functionality. These characteristics enhance the interaction between ions and electrodes, ultimately improving the electrode material's performance. Furthermore, increasing the physical activation temperature from 700°C to 900°C significantly affects the electrochemical properties of supercapacitors. This temperature rise results in modifications to the pore structure and density of the material, which shortens the ion transfer path, improves ion flow, and maintains a high level of conductivity. These effects collectively contribute to the enhanced electrochemical performance of supercapacitors. The reduction of oxygen functionality also plays a role in increasing the specific capacitance of the electrodes. The x-PCV carbon electrodes were also evaluated at various scan rates: 1, 2, and 5 mV/s, as shown in Figures 2 (b), (c), and (d). The voltammetric results demonstrate that all electrodes retain a rectangular shape with minimal disorder, confirming that the electric double-layer capacitance mechanism predominates, with negligible faradaic reaction effects. Additionally, the scan rate influences the volumetric capacitance of the carbon electrodes. Increasing the scan rate from 1 mV/s to 5 mV/s results in a decline in the volumetric capacitance across all x-PCV samples. However, the 900-PCV electrode managed to maintain a volumetric capacitance of 61.2 F/cm³ at 5 mV/s, indicating superior electrochemical stability compared to the other electrodes.

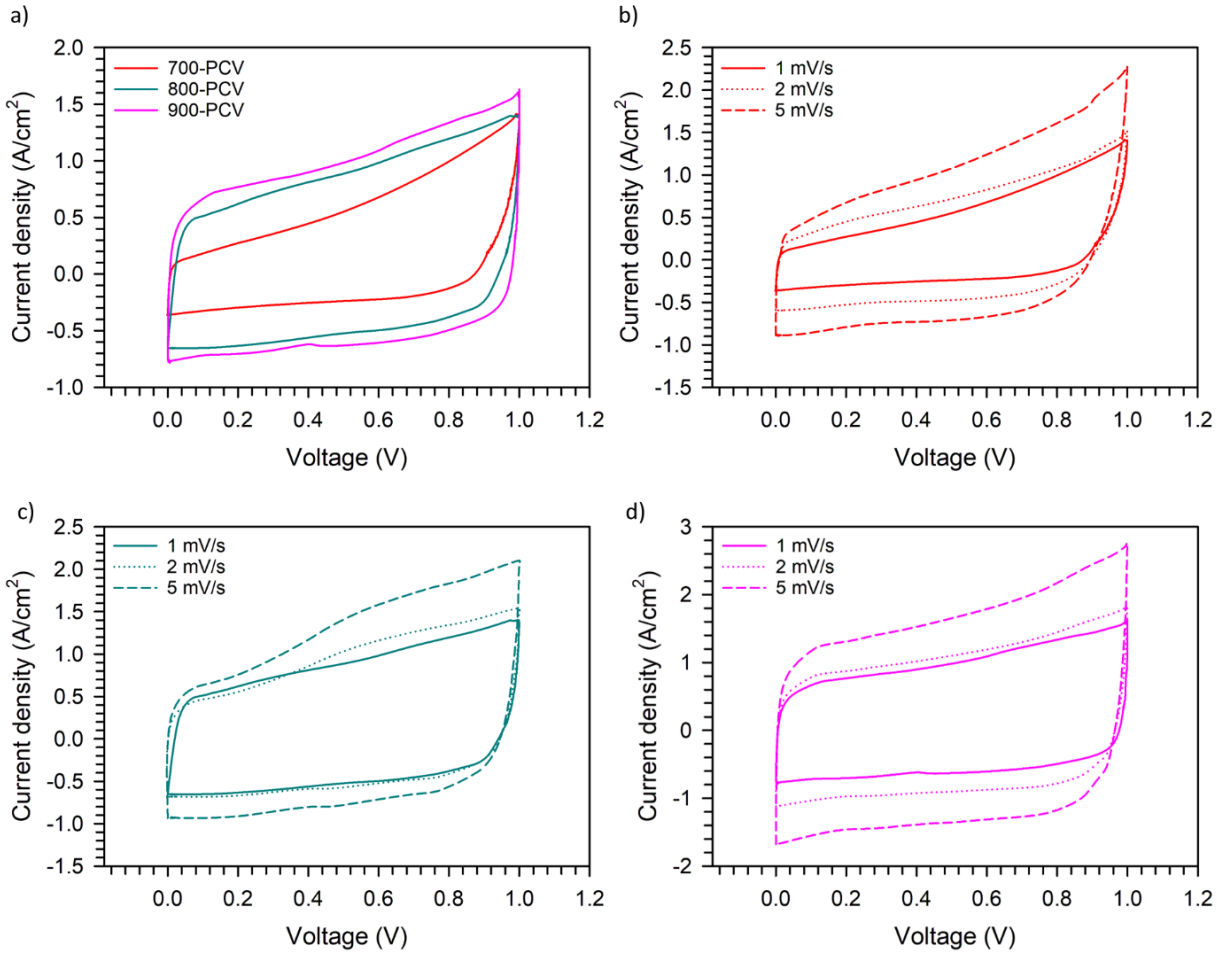

Figure 2. (a) CV profile of x-PCV in 1 mV/s, CV profile in 1-5mV/s of (b) 700-PCV, (c) 800-PCV, and (d) 900-PCV.

Gravimetric Scale Analysis

A gravimetric scale evaluation decisively confirms the electrochemical properties of the x-PCV carbon electrode. Figure 3 clearly illustrates the GCD profiles of the x-PCV material at a current density of 1 A and a scan rate of 5 mV/s. The GCD profiles reveal an imperfect symmetrical triangular shape with non-linear characteristics, which undeniably indicates a dual-electric layer charge storage mechanism alongside faradaic reactions associated with the distribution of oxygen functional groups. This establishes the presence of pseudocapacitance properties in each sample [36].

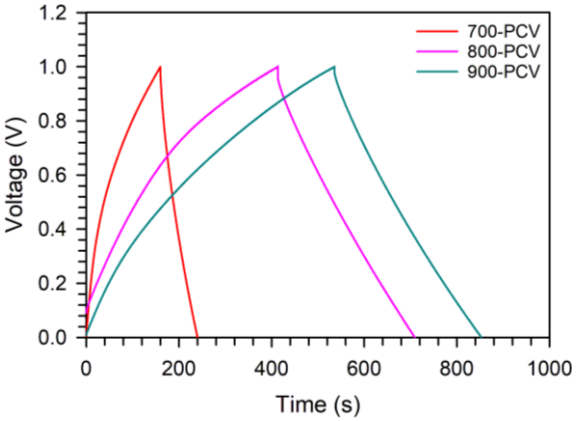

Figure 3. GCD profile of x-PCV.

Moreover, these findings align perfectly with the voltammetry results shown in Figure 2. Furthermore, the sudden potential drop observed at the beginning of the discharge profile varies distinctly among the x-PCV materials. This variation arises from the resistance to ion diffusion into the pores of the electrode material and the conductivity of the carbon electrode [37]. The measured resistance values for the materials, 700-PCV, 800-PCV, and 900-PCV, stand at 6 mΩ, 8 mΩ, and 12 mΩ, respectively. This resistance consistently increases with rising activation temperatures from 700°C to 900°C. Higher temperatures facilitate the growth of smaller pores, which markedly reduces ion accessibility on the surface of the supercapacitor electrode [4]. According to standard equations, the GCD profile shows that the specific capacitance of the carbon electrode peaks at 181 F/g for the 900-PCV sample, followed by 800-PCV at 167 F/g and 700-PCV at 101 F/g. These results emphatically corroborate the cyclic voltammetry (CV) analysis presented earlier in Figure 2. The energy density and power density derived from this GCD technique are comprehensively summarized in Figure 3. Remarkably, the superior electrochemical performance of 900-PCV eclipses the other samples and stands as comparable to previously reported biomass-based carbon materials [38, 39]. Additionally, the capacitance values obtained through the GCD method exceed those from the CV method. This difference is attributed to variations in current, as higher currents typically result in smaller capacitance values due to kinetic factors. While both methods are useful for measuring capacitance, they deliver distinct insights; CV can pinpoint non-capacitive redox reactions, while GCD effectively reveals cell or electrode resistance [40].

CONCLUSION

Evaluating supercapacitor performance at a volumetric scale is essential for demonstrating the real-world applicability of developed materials. This study decisively presents the volumetric evaluation of banana leaf-derived porous carbon materials for supercapacitor use, emphasizing the voltammographic cycling technique while distinctly comparing it to the gravimetric scale assessed through the galvanostatic charge-discharge method. The carbon electrodes were expertly prepared in a dual configuration within a symmetric system using sulfuric acid electrolyte media. Initial density analysis unequivocally showcased the porosity properties of the electrode materials. Following the pyrolysis process, we observed a significant density reduction of 10-12%, confirming the high porosity of each x-PCV precursor. Moreover, the CV technique achieved an impressive volumetric capacitance of 198 F/cm³ for the 900-PCV material, while

the GCD technique yielded a gravimetric capacitance of 181 F/g from the same material. These outstanding capacitive properties strongly indicate that utilizing banana leaf waste as activated carbon, combined with the preparation method implemented, holds remarkable potential as a fundamental electrode material to significantly enhance supercapacitor performance as a cutting-edge electrochemical energy storage solution.

REFERENCES

1. Tadesse, M. G., Ahmmed, A. S., & Lübben, J. F. (2024). Review on conductive polymer composites for supercapacitor applications. *Journal of Composites Science*, **8**(2), 53.
2. Khan, H. A., Tawalbeh, M., Aljawrneh, B., Abuwatfa, W., Al-Othman, A., Sadeghifar, H., & Olabi, A. G. (2024). A comprehensive review on supercapacitors: Their promise to flexibility, high temperature, materials, design, and challenges. *Energy*, 131043.
3. Yuan, C., Xu, H., El-khodary, S. A., Ni, G., Esakkimuthu, S., Zhong, S., & Wang, S. (2024). Recent advances and challenges in biomass-derived carbon materials for supercapacitors: A review. *Fuel*, **362**, 130795.
4. Hu, H., Yan, M., Jiang, J., Huang, A., Cai, S., Lan, L., Ye, K., Chen, D., Tang, K., Zuo, Q., Zeng, Y., Tang, W., Fu, J., Jiang, C., Wang, Y., Yan, Z., He, X., Qiao, L., & Zhao, Y. (2024). A state-of-the-art review on biomass-derived carbon materials for supercapacitor applications: From precursor selection to design optimization. *Science of The Total Environment*, **912**, 169141.
5. Tiwari, S. K., Sahoo, S., Wang, N., & Huczko, A. (2020). Graphene research and their outputs: Status and prospect. *Journal of Science: Advanced Materials and Devices*, **5**(1), 10–29.
6. Saini, S., Chand, P., & Joshi, A. (2021). Biomass derived carbon for supercapacitor applications. *Journal of Energy Storage*, **39**, 102646.
7. Liu, D., Zhang, W., & Huang, W. (2019). Effect of removing silica in rice husk for the preparation of activated carbon for supercapacitor applications. *Chinese Chemical Letters*, **30**(6), 1315–1319.
8. Liu, B., Wang, X., Chen, Y., Xie, H., Zhao, X., Nassr, A. B., & Li, Y. (2023). Honeycomb carbon obtained from coal liquefaction residual asphaltene for high-performance supercapacitors in ionic and organic liquid-based electrolytes. *Journal of Energy Storage*, **68**, 107826.
9. Shao, Y., Liu, Y., Guan, Q., & Ding, C. (2022). Nitrogen doped layered porous carbon derived from peanut shell for high volumetric performance supercapacitors. *Materials Letters*, **323**, 132580.
10. Wang, Q., Yan, J., & Fan, Z. (2016). Carbon materials for high volumetric performance supercapacitors: design, progress, challenges and opportunities. *Energy and Environmental Science*, **9**(3), 729–762.
11. Kim, J., Wi, S. M., Son, S., Lim, H., Park, Y., Jang, A. R., Park, J. B., Cho, Y., Song, Y. C., Pak, S., & Lee, Y. W. (2024). Rationally engineered interdigitated electrodes with heteroatom doped porous graphene and improved surface wettability for flexible micro-supercapacitors. *Journal of Energy Storage*, **86**, 111271.
12. Taer, E., Apriwandi, A., Andriani, D., Fudholi, A., Citraningrum, N., Deraman, M., & Taslim, R. (2024). Self-doped N, P, O heteroatoms carbon nano-hollow-fiber derived aromatic bio-organic for advanced gravi-volumetric supercapacitors. *Journal of Physics D: Applied Physics*, **57**(46), 465501.
13. Yu, T., Zhou, Q., Chen, J., Ma, W., Wang, C., Fan, S., & Zhang, Y. (2024). The synthesis of nanocellulose/B, N, F tri-doped graphene composite hydrogels for supercapacitor applications. *Vacuum*, **222**, 113036.

14. Long, C., Chen, X., Jiang, L., Zhi, L., & Fan, Z. (2015). Porous layer-stacking carbon derived from in-built template in biomass for high volumetric performance supercapacitors. *Nano Energy*, **12**, 141–151.
15. Zhang, Y., Yu, Y., Xiao, R., Du, C., Wan, L., Ye, H., Chen, J., Wang, T., & Xie, M. (2022). Faradaic-active N-doped reduced graphene as electrode for supercapacitor with high-volumetric performances. *Journal of Energy Storage*, **54**, 105299.
16. Yakaboylu, G. A., Jiang, C., Yumak, T., Zondlo, J. W., Wang, J., & Sabolsky, E. M. (2021). Engineered hierarchical porous carbons for supercapacitor applications through chemical pretreatment and activation of biomass precursors. *Renewable Energy*, **163**, 276–287.
17. Lu, Z., Foroughi, J., Wang, C., Long, H., & Wallace, G. G. (2018). Superelastic hybrid CNT/graphene fibers for wearable energy storage. *Advanced Energy Materials*, **8**(8), 1702047.
18. Gopalakrishnan, A. & Badhulika, S. (2020). Effect of self-doped heteroatoms on the performance of biomass-derived carbon for supercapacitor applications. *Journal of power sources*, **480**, 228830.
19. Li, Q., Jiang, Y., Jiang, Z., Zhu, J., Gan, X., Qin, F., Tang, T., Luo, W., Guo, N., Liu, Z., Wang, L., Zhang, S., Jia, D., & Fan, Z. (2022). Ultrafast pore-tailoring of dense microporous carbon for high volumetric performance supercapacitors in organic electrolyte. *Carbon*, **191**, 19–27.
20. Taer, E., Pratiwi, L., Apriwandi, A., Mustika, W. S., Taslim, R., & Agustino, A. (2020). Three-dimensional pore structure of activated carbon monolithic derived from hierarchically bamboo stem for supercapacitor application. *Communications in Science and Technology*, **5**(1), 22–30.
21. Gabookolwe, M. K., Onisuru, O. R., Odisitse, S., Meijboom, R., Muiva, C., & King'ondu, C. K. (2024). Biomass Nanoarchitectonics of abattoir waste to high coulombic efficient mesoporous carbon materials for supercapacitors. *Journal of Energy Storage*, **104**, 114541.
22. Yardım, Y., Genel, İ., & Saka, C. (2025). Enhanced supercapacitor performance of hierarchical mesoporous sulfur-doped carbon particles from biomass waste for energy storage. *International Journal of Hydrogen Energy*, **99**, 383–393.
23. Julnaidi, Amri, A., Saputra, E., Nofrizal, & Taer, E. (2023). High well-matched energy gravimetric–volumetric symmetric super-capacitor derived from hollow paper stack-like biomass-based functional carbon. *Journal of Chemical Technology & Biotechnology*, **98**(9), 2330–2342.
24. Miller, E. E., Hua, Y., & Tezel, F. H. (2018). Materials for energy storage: Review of electrode materials and methods of increasing capacitance for supercapacitors. *Journal of Energy Storage*, **20**, 30–40.
25. Ayinla, R. T., Dennis, J. O., Zaid, H. M., Sanusi, Y. K., Usman, F., & Adebayo, L. L. (2019). A review of technical advances of recent palm bio-waste conversion to activated carbon for energy storage. *Journal of cleaner production*, **229**, 1427–1442.
26. Taer, E., Apriwandi, A., Ningsih, Y. S., & Taslim, R. (2019). Preparation of activated carbon electrode from pineapple crown waste for supercapacitor application. *International Journal of Electrochemical Science*, **14**(3), 2462–2475.
27. Taer, E., Dewi, P., Sugianto, S., Syech, R., Taslim, R., Salomo, S., Susanti, Y., Purnama, A., Apriwandi, A., Agustino, A., & Setiadi, R. N. (2018). The synthesis of carbon electrode supercapacitor from durian shell based on variations in the activation time. *AIP conference proceedings*, **1927**(1), 030026.
28. Fan, Y., Cai, Y., Li, X., Jiao, L., Xia, J., & Deng, X. (2017). Effects of the cellulose, xylan and lignin constituents on biomass pyrolysis characteristics and bio-oil composition using the Simplex Lattice

Mixture Design method. *Energy Conversion and Management*, **138**, 106.
29. González, J. F., Román, S., Encinar, J. M., & Martínez, G. (2009). Pyrolysis of various biomass residues and char utilization for the production of activated carbons. *Journal of Analytical and Applied Pyrolysis*, **85**(1-2), 134–141.
30. Wang, Y., Qu, Q., Gao, S., Tang, G., Liu, K., He, S., & Huang, C. (2019). Biomass derived carbon as binder-free electrode materials for supercapacitors. *Carbon*, **155**.
31. Taer, E., Apriwandi, A., Taslim, R., Agutino, A., & Yusra, D. A. (2020). Conversion Syzygium oleana leaves biomass waste to porous activated carbon nanosheet for boosting supercapacitor performances. *Journal of Materials Research and Technology*, **9**(6), 13332.
32. Taer, E., Taslim, R., Putri, A. W., Apriwandi, A., & Agustino, A. (2018). Activated carbon electrode made from coconut husk waste for supercapacitor application. *International Journal of Electrochemical Science*, **13**(12), 12072.
33. Xu, H., Dong, L., Zhang, B., Wang, K., Meng, J., Tong, Y., & Wang, H. (2024). Heteroatom self-doped graphitic carbon materials from Sargassum thunbergii with improved supercapacitance performance. *Advanced Sensor and Energy Materials*, **3**(2), 100102.
34. Yumak, T., Yakaboylu, G. A., Oginni, O., Singh, K., Ciftyurek, E., & Sabolsky, E. M. (2020). Comparison of the electrochemical properties of engineered switchgrass biomass-derived activated carbon-based EDLCs. *Colloids and Surfaces A: Physicochemical and Engineering Aspects*, **586**, 124150.
35. Liu, F., Wang, Z., Zhang, H., Jin, L., Chu, X., Gu, B., Huang, H., & Yang, W. (2019). Nitrogen, oxygen and sulfur co-doped hierarchical porous carbons toward high-performance supercapacitors by direct pyrolysis of kraft lignin. *Carbon*, **149**, 105–116.
36. Wei, H., Wang, H., Li, A., Li, H., Cui, D., Dong, M., Lin, J., Fan, J., Zhang, J., Hou, H., Shi, Y., Zhou, D., & Guo, Z. (2020). Advanced porous hierarchical activated carbon derived from agricultural wastes toward high performance supercapacitors. *Journal of Alloys and Compounds*, **820**, 153111.
37. Riyanto, C. A., Ampri, M. S., & Martono, Y. (2020). Synthesis and characterization of nano activated carbon from Annatto Peels (*Bixa orellana L.*) viewed from temperature activation and impregnation ratio of H_3PO_4. *EKSAKTA: Journal of Sciences and Data Analysis*, 44–50.
38. Taer, E., Tampubolon, D. K. H., Farma, R., Setiadi, R. N., & Taslim, R. (2021). Longan Leaves biomass-derived renewable activated carbon materials for electrochemical energy storage. *Journal of Physics: Conference Series*, **2049**(1), 012009.
39. Taer, E. & Taslim, R. (2021). High Potential of Averrhoa bilimbi Leaf Waste as Porous Activated Carbon Source for Sustainable Electrode Material Supercapacitor. *Journal of Physics: Conference Series*, **2049**(1), 012051.
40. Stoller, M. D. & Ruoff, R. S. (2010). Best practice methods for determining an electrode material's performance for ultracapacitors. *Energy and Environmental Science*, **3**(9), 1294–1301.

IPC

Indonesian Physics Communication

Department of Physics, Universitas Riau, Pekanbaru, Indonesia
p-ISSN 1412-2960 | e-ISSN 2579-521X

Vol. 22 | No. 1
March 2025

Web: https://kfi.ejournal.unri.ac.id
E-mail: kfi@ejournal.unri.ac.id

The effect of reaction time and oil-to-methanol ratio on the calorific value of biodiesel produced from chicken fat oil

Alltop Amri Ya Habib[1,*], Tengku Emrinaldi[2], Yogi Yolanda[1], Yelmida Azis[1]
[1]Department of Chemical Engineering, Universitas Riau, Pekanbaru 28293, Indonesia
[2]Department of Physics, Universitas Riau, Pekanbaru 28293, Indonesia

*Corresponding author: alltopamri@lecturer.unri.ac.id

ABSTRACT

The energy content of a fuel is represented by its calorific value. When biodiesel combusts in the presence of air or oxygen, the heat released during the combustion process is expressed as the calorific value. This study aims to analyze the effect of reaction time (60, 120, and 180 minutes) and the volume ratio of chicken fat oil-to-methanol (OM) (25:30 and 25:50) in the transesterification process on the calorific value of the produced biodiesel. The transesterification process was conducted using MgO as a catalyst under various reaction times and OM ratios. The produced biodiesel was then analyzed to determine its calorific value as a key fuel quality parameter. The results indicate that a longer reaction time and a higher OM volume ratio lead to an increase in the calorific value. The highest calorific value obtained in this study was 9952 kcal/kg, achieved at a reaction time of 180 minutes and an OM volume ratio of 25:50.

Keywords: Biodiesel; calorific value; chicken fat oil; oil-to-methanol ratio; reaction time

Received 23-02-2025 | Revised 21-03-2025 | Accepted 27-03-2025 | Published 31-03-2025

INTRODUCTION

The demand for alternative energy sources is increasing as fossil fuel reserves continue to deplete and awareness of their environmental impact grows. Biodiesel is a promising alternative fuel derived from renewable resources such as vegetable oils and animal fats. Compared to fossil fuels, biodiesel offers several advantages, including greater environmental friendliness, biodegradability, and lower greenhouse gas emissions [1-2].

One of the potential feedstocks for biodiesel production is chicken fat oil [3-4]. Chicken fat waste generated from the poultry processing industry has not been optimally utilized, despite its high triglyceride content, which makes it suitable for conversion into biodiesel through the transesterification process. This process involves a reaction between oil and methanol in the presence of a catalyst to produce methyl esters (biodiesel) and glycerol as a by product.

The efficiency and quality of the produced biodiesel are influenced by several factors, including the type of catalyst, reaction temperature, reaction time, and the oil-to-methanol (OM) ratio [5-6]. A reaction time that is too short may result in an incomplete reaction, leading to suboptimal oil-to-biodiesel (OB) conversion. Conversely, an excessively long reaction time can cause product degradation. Additionally, the oil-to-methanol ratio plays a crucial role in determining conversion efficiency. An optimal methanol ratio enhances biodiesel formation, while excess methanol can produce excessive glycerol, which may interfere with the biodiesel purification process [1, 3, 5].

Based on this background, this study was conducted to evaluate the effect of reaction time and the OM ratio on the calorific value of biodiesel produced from chicken fat oil. The calorific value is a crucial parameter for assessing fuel quality, as it determines the amount of energy generated during biodiesel combustion. By understanding the relationship between process parameters and the resulting calorific value, this research aims to contribute to the optimization of biodiesel production from chicken fat waste.

LITERATURE REVIEW

Biodiesel (Methyl Ester)

Biodiesel is an alternative fuel for diesel engines derived from renewable resources, specifically alkyl esters of fatty acids. It can be produced from vegetable oils, animal fats, or recycled waste cooking oil. As an environmentally friendly fuel, biodiesel consists of various fatty acid esters obtained from plant-based oils, such as palm oil, coconut oil, *Jatropha* oil, and kapok seed oil, as well as from animal fats, including lard, chicken fat, beef tallow, and fish oil [1].

As a substitute for conventional diesel fuel, biodiesel is produced from renewable feedstocks, including vegetable oils and animal fats. Compared to fossil fuels, biodiesel offers several advantages, such as being biodegradable, non-toxic, and having lower CO_2 and sulfur gas emissions. These characteristics make biodiesel a more environmentally sustainable fuel option. Table 1 presents the biodiesel quality standards based on SNI 7182-2015.

Table 1. Biodiesel quality standards based on SNI 7182-2015.

Parameter	Unit	Value	Test method
Density (40ºC)	kg/m^3	850 – 890	ASTM D 1298
Viscosity (40ºC)	mm^2/s (cSt)	2.3 – 6.0	ASTM D 445
Cetane number	min	51	ASTM D 613
Flash point	ºC, min	100	ASTM D 93
Fog point	ºC, max	18	ASTM D 2500
Water and sediments	%-volume, max	0.05	ASTM D 2709 / ASTM D 1796
Acid number	KOH/g, max	0.5	AOCS Cd 3d-63
Iodine number	%-massa (g-I_2/100 g), max	115	AOCS Cd 1-25
Calorific value	kcal/kg, max	9938.76	ASTM D240

The Calorific Value

The calorific value of biodiesel refers to the amount of energy released during complete combustion. Generally, biodiesel has a lower calorific value compared to fossil diesel due to its higher oxygen content. This is attributed to the chemical structure of methyl esters that make up biodiesel, where the presence of oxygen reduces the energy content per unit mass. Despite this, biodiesel remains an attractive alternative fuel as it produces cleaner emissions and excellent lubricant properties [7].

Several factors influence the calorific value of biodiesel, including fatty acid composition, feedstock type, and transesterification process parameters such as the methanol-to-oil molar ratio and reaction time. Saturated fatty acids tend to have a higher calorific value than unsaturated ones due to their more stable combustion properties. Additionally, optimizing the methanol ratio in the transesterification process is crucial to ensuring complete conversion of oil into methyl esters. If the methanol ratio is too low, the reaction may be incomplete, leading to lower energy content, whereas excessive methanol requires additional separation steps increasing production costs [8].

Besides the methanol ratio, reaction time also plays a crucial role in determining biodiesel quality and its calorific value. A reaction time that is too short can result in incomplete conversion, leaving behind higher glyceride content and reducing energy output. On the other hand, excessive reaction time may lead to the formation of unwanted by-products, such as soap or peroxides, which negatively affect combustion efficiency. Therefore, optimizing process parameters is essential in biodiesel production to achieve a calorific value comparable to conventional diesel fuels.

RESEARCH METHODS

Materials and Tools

The materials used in this study include animal oil extracted from chicken fat, MgO,

methanol (CH_3OH), oxalic acid, phenolphthalein indicator, and distilled water. The equipment utilized in this research consists of beakers, a separatory funnel, a funnel, filter paper, a two-neck flask, a heating mantle, a condenser, clamps and a stand, an Erlenmeyer flask, an oven, a dropper pipette, an analytical balance, a thermometer, a pycnometer, an Ostwald viscometer, a burette, a stirring rod, a graduated cylinder, and a volumetric flask.

Procedure Reasearch

Preparation of Chicken Fat Oil

Chicken fat is first cleaned and placed in a container before being heated in an oven at 80°C for 24 hours. After the heating process, the fat is separated and filtered to obtain chicken fat oil. The extracted oil is then analyzed for its free fatty acid (FFA) content, density, moisture content, and viscosity.

Biodiesel Transesterification

A total of 25 ml of chicken fat oil is placed into a two-neck flask and heated to 60°C. Once the desired temperature is reached, 30 ml of methanol and 0.5 grams of MgO catalyst are added. The reaction is allowed to proceed for 60 minutes. After completion, the mixture is transferred to a separatory funnel and left undisturbed until two distinct layers are formed. The upper layer consists of crude biodiesel, while the lower layer contains the residual methanol and catalyst. The upper layer is separated and further purified using hot water to remove impurities. The procedure is repeated for reaction times of 120 minutes and 180 minutes, as well as for a variation in the oil-to-methanol ratio of 25:50 ml. Finally, the calorific value of the biodiesel is analyzed.

RESULTS AND DISCUSSION

The calorific value of combustion refers to the amount of heat or energy released during the burning process of a specific quantity of fuel in the presence of air or oxygen. Based on the SNI 7182-2015 standard, the maximum calorific value of biodiesel is 9938.76 kcal/kg. The calorific values obtained in this study can be observed in Figure 1, which presents the results for different reaction times (60, 120, and 180 minutes) and an OM ratio of 25:30.

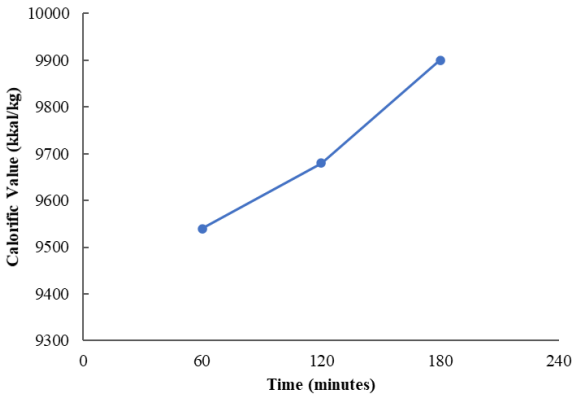

Figure 1. Calorific value at different reaction times with an OM ratio of 25:30.

Based on Figure 1, the calorific value of biodiesel increases with longer reaction times. This phenomenon occurs because extended reaction durations facilitate a more complete transesterification process, enhancing the conversion of triglycerides into methyl esters. As a result, the biodiesel produced has a lower concentration of unreacted components, such as glycerides and free fatty acids, which can negatively impact its energy content. A more complete reaction improves the purity of biodiesel, leading to a higher calorific value [9], [10]. Furthermore, optimizing reaction time minimizes the formation of undesirable by-products that could reduce combustion efficiency. However, excessively long reaction times may promote secondary reactions or biodiesel degradation, necessitating careful control to maintain fuel quality [11].

Based on Figure 2, it is evident that, in addition to reaction time, the OM ratio significantly influences the resulting calorific value. This effect can be attributed to the role of methanol in the transesterification process, where an optimal molar ratio ensures efficient conversion of triglycerides into biodiesel. Studies have demonstrated that varying the methanol-to-oil (MO) molar ratio impacts the

yield and quality of biodiesel produced. For instance, research indicates that increasing the MO molar ratio can enhance biodiesel yield up to an optimal point, beyond which the yield may plateau or even decrease due to factors such as glycerol solubility in methanol and difficulties in phase separation. Therefore, selecting an appropriate OM ratio is crucial for maximizing the calorific value of biodiesel, as it ensures a more complete transesterification reaction and minimizes the presence of unreacted components that could lower the energy content of the final product [8].

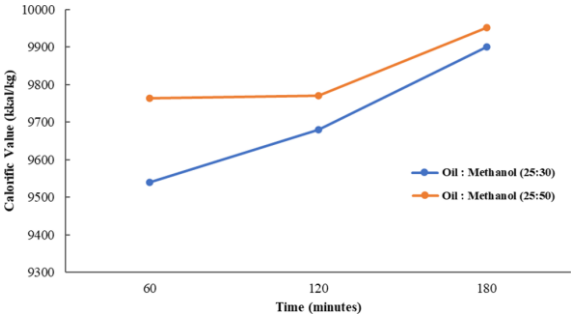

Figure 2. Calorific value at different reaction times with an OM ratio (25:30 and 25:50).

CONCLUSION

The findings indicate that both reaction time and the OM ratio play crucial roles in determining the calorific value of biodiesel. A longer reaction time enhances the transesterification process, leading to a more complete conversion of triglycerides into methyl esters, which increases the calorific. The optimal OM ratio is critical to maximize biodiesel yield and energy content, as it ensures efficient conversion while minimizing the presence of unreacted components. However, exceeding the optimal ratio may lead to a decline in biodiesel quality due to issues such as glycerol solubility and phase separation challenges. Therefore, careful optimization of these parameters is necessary to produce high-quality biodiesel with superior energy content, making it a viable and sustainable alternative to conventional diesel fuels.

REFERENCES

1. Nirmala, R. L. (2019). Pengaruh katalis CaO dari cangkang bekicot pada pembuatan biodiesel dari lemak sapi. *Jurnal Crystal*, **1**(01), 39–54.
2. Aziz, A., Mukhsin, M., & Aulia, F. (2024). Interesterifikasi biodiesel non alcohol dengan bahan baku minyak bekas. *Pros. Politeknik Negeri Lhokseumawe*, 7.
3. Habib, A. A. Y. & Suhendri, S. (2024). Pengaruh waktu reaksi transesterifikasi biodiesel dari minyak lemak ayam. *J. Bioprocess Chem. Environ. Eng. Sci.*, **5**(2).
4. Pratama, R. V., Mardiana, M., & Niawanti, H. (2019). Pemanfaatan limbah lemak ayam broiler (*Gallus domesticus*) sebagai bahan baku. *Jurnal Chemurgy*, **2**(2), 6–14.
5. Mukminin, A., Megawati, E., & Sapril, S. (2023). Pengaruh waktu reaksi pembuatan biodiesel dari minyak jelantah dengan bantuan katalis. *J. Educ*, **5**(2), 5119–5127.
6. Muarif, A., Fatnia, F., & Bahri, S. (2024). Pengaruh suhu dan waktu reaksi terhadap hasil sintesis biodiesel dari minyak. *Jurnal Teknologi Kimia Unimal*, **13**(1), 58–71.
7. Putra, R., Supriyadi, S., & Suheli, S. (2021). Analisa pembuatan biodiesel minyak jelantah dengan katalis. *J. Vocat. Educ. Automot. Technol.*, **3**(1), 137–145.
8. Prihanto, A. & Irawan, T. B. (2018). Pengaruh temperatur, konsentrasi katalis dan rasio molar metanol-minyak terhadap yield biodisel. *Metana*, **13**(1), 30–36.
9. Foroutan, R., Mohammadi, R., & Ramavandi, B. (2021). Waste glass catalyst for biodiesel production from waste chicken fat. *Fuel*, **291**, 120151.
10. Kirubakaran, M. & Selvan, V. A. M. (2018). A comprehensive review of low cost biodiesel production. *Renew. Sustain. Energy Rev.*, **82**, 390–401.
11. Banga, S. & Pathak, V. V. (2023). Biodiesel production from waste cooking oil. *Energy Nexus*, **10**, 100209.

IPC

Indonesian Physics Communication

Department of Physics, Universitas Riau, Pekanbaru, Indonesia
p-ISSN 1412-2960 | e-ISSN 2579-521X

Vol. 22 | No. 1
March 2025

Web: https://kfi.ejournal.unri.ac.id
E-mail: kfi@ejournal.unri.ac.id

Evaluation of the Arima-Kalman model in predicting rainfall in Medan City in 2023 using observation data from 2013 – 2022

Alva Josia Lumbantoruan, Yahya Darmawan*, Munawar Munawar, Nardi Nardi, Fendy Arifianto, Ervan Ferdiansyah
Indonesia College of Meteorology, Climatology and Geophysics (STMKG), Tangerang 15221, Indonesia

*Corresponding author: yahya.darmawan@bmkg.go.id

ABSTRACT

This paper aims to evaluate the ARIMA-Kalman model in predicting rainfall in Medan City for the year 2023. The data used are historical observation data of rainfall from 2013 to 2022 that have been tested for stationary and homogeneity, which proved not to require additional correction. The analysis results show that the ARIMA-Kalman model can capture the general pattern of rainfall well, and shows superiority in producing predictions that are closer to the actual data, with a mean absolute error (MAE) value of 54.11, which is lower than the MAE of the ARIMA model which reaches 55.66. Although the ARIMA model has a smaller root mean square error (RMSE) (66.67 compared to 69.75 for ARIMA-Kalman), the ARIMA-Kalman model shows better consistency, especially in capturing significant fluctuations, such as the peak rainfall that occurred in July 2023. Therefore, ARIMA-Kalman is proven to be more accurate and reliable for predicting rainfall in Medan city, making it a better choice to support water resources planning and management.

Keywords: ARIMA; Kalman filter; model; prediction; rainfall

Received 27-01-2025 | Revised 08-03-2025 | Accepted 24-03-2025 | Published 31-03-2025

INTRODUCTION

Rainfall is one of the variables determining climatic conditions which is directly related to the success of various fields, including agriculture and plantations. In Indonesia, rainfall is the main factor influencing the climate in tropical areas. However, the level of rainfall is often difficult to predict, so many people still lack strategies for dealing with fluctuations in rainfall [1].

Medan City, as one of the big cities in Indonesia, is not immune to the impact of changes in rainfall [2]. Most of the activities of the Medan City population depend on rainfall, from farmers, fishermen, transportation users, to food production. Therefore, accurate rainfall predictions are needed to help various sectors prepare for weather changes [1].

In an effort to improve the accuracy of rainfall predictions, various forecasting methods have been developed. One of the commonly used methods is the autoregressive integrated moving average (ARIMA) model [3]. The ARIMA model is effective for time series data and can produce accurate short-term forecasts [4]. However, to improve prediction accuracy, several studies have combined the ARIMA model with other methods, such as the Kalman Filter.

The Kalman filter is a model of part of the state space that can be applied in forecasting models. This model uses a recursive technique to integrate the latest observation data into the model, correct previous predictions, and make further predictions optimally based on past information and current data [5]. The combination of ARIMA and Kalman filter has shown promising results in improving the accuracy of rainfall predictions [6].

Evaluation of the ARIMA-Kalman model in predicting rainfall in Medan City in 2023 is important to do. This aims to determine the extent to which the model can provide accurate and reliable predictions. The results of this evaluation are expected to help parties affected by rainfall in establishing strategies to deal with the ups and downs of rainfall in the future.

LITERATURE REVIEW

Time Series Analysis

Time series analysis is a statistical method used to analyze data collected over a period of time. It is essential in various fields, including meteorology, economics, and engineering, as it allows researchers to understand patterns and trends in time-related data. In the context of rainfall, time series analysis helps in identifying seasonal patterns, long-term trends, and fluctuations that can affect water resource planning and management [4].

A time series consists of a series of observations taken at regular time intervals. One of the main objectives of time series analysis is to forecast future values based on historical data. To achieve this goal, it is important to identify whether the data is stationary or not [7]. Data is said to be stationary if its mean and variance are constant over time [8]. If the data is not stationary, then a transformation, such as differencing, needs to be performed to make it stationary. Stationarity tests can be performed using the autocorrelation function (ACF) and partial autocorrelation function (PACF), which help in determining the relationship between the current observation and the previous observations.

ARIMA Model

The ARIMA model is one of the methods most commonly used in time series analysis. This model was introduced by Box and Jenkins and is a generalization of the autoregressive moving average (ARMA) model with the addition of an integration component to deal with non-stationary data. ARIMA combines three main components: autoregressive (AR), integrated (I), and moving average (MA) [9].

Autoregressive

AR is a component that shows that current values are influenced by previous values. This reflects the relationship between current observations and past observations. In the context of rainfall, this means that rainfall in a particular month can be influenced by rainfall in previous months.

Integrated

I is a process that involves differentiating the data to remove trends and make the data stationary. This is important because many time series analysis methods, including ARIMA, require stationary data to generate accurate results. The differentiation process can be carried out one or more times, depending on the level of data non-stationarity.

Moving Average

MA is a component that shows that the current value is influenced by the prediction error of previous values. This helps in reducing the variability in the data. In the context of rainfall, this means that the error in the rainfall prediction in the previous month can affect the rainfall prediction in the current month.

The ARIMA model is expressed in the notation ARIMA (p, d, q), where p is the order of the autoregressive component, d is the amount of differentencing performed to make the data stationary, and q is the order of the MA component. The selection of parameters p, d, and q is done through ACF and PACF analysis, as well as parameter significance tests [10]. The ARIMA model has proven effective in capturing temporal patterns in time series data, so it is often used in rainfall forecasting.

Kalman Filter

The Kalman filter is a method used to estimate the state of a dynamic system from a series of measurements containing noise. This method is very useful in situations where the available data has uncertainty, such as in rainfall measurements which are often influenced by external factors. The Kalman filter works by combining previous estimates with the latest observation data to produce a more accurate estimate.

The basic concept of the Kalman Filter involves two main steps: prediction and updating. In the prediction step, the model is used to estimate the state of the system at a later time, while in the updating step, the estimate is updated based on the latest observation data. This process is recursive, meaning that the Kalman Filter can continue to update the estimate as new data is added.

The main advantage of the Kalman Filter is its ability to provide more accurate estimates by minimizing prediction errors. This method can also be adapted for various applications, including system control, signal processing, and time series analysis. In the context of rainfall forecasting, the Kalman filter can be used to improve the accuracy of the ARIMA model by correcting the prediction based on the latest observation data.

Application of the ARIMA-Kalman Model in Rainfall Forecasting

In this study, the ARIMA model is used to analyze rainfall data in Medan City, while the Kalman filter is used to improve the accuracy of ARIMA model predictions [11]. The rainfall data used covers a fairly long period to a long time, allowing for in-depth analysis of existing patterns and trends.

The results of this study are expected to provide a significant contribution to water resources management and agricultural planning in Medan City, especially in facing the challenges of climate change and increasingly frequent extreme weather. By using the ARIMA-Kalman model, it is expected to reduce uncertainty in rainfall predictions, so that decision making in water resources management can be done better.

RESEARCH METHODS

Research Location

This research is located in Medan City, which is the capital of North Sumatra Province, Indonesia. Medan City is located in the northern part of Sumatra Island and is one of the largest cities in Indonesia with unique rainfall characteristics. The city is geographically located at coordinates 3°35′N (north latitude) and 98°40′E (east longitude).

Figure 1. Research location in Medan City.

Research Data

The data used in this study are divided into two parts, namely training data and test data.

Training Data

The training data consists of monthly rainfall observation data for Medan City from 2013 to 2022. This data was obtained from the Meteorology, Climatology, and Geophysics Agency (BMKG). The data collected will include the total rainfall for each month during that period. This Training Data will be used to build ARIMA and Kalman filter models.

Test Data

The test data consists of monthly rainfall observation data for Medan City for 2023. This data will be used to test the accuracy of the model that has been built using the training data.

Research Tools

In this study, several tools and software used for data analysis and processing are as follows:

R Studio

R Studio is an integrated development environment (IDE) for the R programming language used for statistical analysis and data modeling. In this study, R Studio will be used to build ARIMA and Kalman filter models, as well as to perform the necessary statistical analysis.

Microsoft Word

Microsoft Word is used to compile research journals, including text processing, and compiling tables and graphs.

ArcGIS

ArcGIS is used to map rainfall data and analyze rainfall distribution patterns in the Medan City area.

Mendeley

Mendeley is used to manage and organize references and citations in research.

Research Stages

Stationary Test of Rainfall Data

Before building the ARIMA model, a data stationarity test is carried out. Time series data is said to be stationary if its statistics do not change over time, meaning there is no clear trend or seasonal pattern. A common test used to test stationarity is the augmented Dickey-fuller (ADF) test. The ADF Test formula is as follows:

$$\Delta y_t = \alpha + \beta t + \varphi y_{t-1} + \sum_{i=1}^{p} \gamma_i \Delta y_{t-i} + \varepsilon_t \qquad (1)$$

If the p-value of the ADF test is less than the significance level (for example, 0.05), then the null hypothesis (non-stationary data) is rejected, and the data is considered stationary.

Rainfall Data Homogeneity Test

The homogeneity test aims to ensure that the rainfall data used comes from the same population and is not affected by systematic changes. One common method used to test homogeneity is the Pettitt Test. The Pettitt Test calculates the K statistic to determine whether there is a significant change in the data. The Pettitt test formula is as follows:

$$K = \sum_{i=1}^{n} \sum_{j=1+1}^{n} sgn(y_j - y_i) \qquad (2)$$

If the K value exceeds the specified critical value, then the data is considered non-homogeneous.

ARIMA Modeling

The ARIMA model is one of the common methods used in time series analysis for forecasting. This model combines three main components, namely AR, I, and MA.

Autoregressive

AR is an ARIMA component that shows that the current value is influenced by previous values. The AR model can be expressed by the formula:

$$y_t = c + \sum_{i=1}^{p} \theta_j y_{t-j} + \varepsilon_t \qquad (3)$$

Integrated

I is the differentencing process used to make data stationary, namely eliminating trends and seasonality. The differentencing process can be expressed as:

$$y_t{}' = y_t - y_{t-1} \qquad (4)$$

Moving Average

MA is a component that shows that the current value is influenced by prediction errors from previous values. The MA model can be expressed by the formula:

$$y_t = c + \sum_{i=1}^{q} \theta_j \varepsilon_{t-j} + \varepsilon_t \quad (5)$$

From equations (3), (4) and (5), the overall ARIMA model can be expressed as:

$$y_t = c + \sum_{i=1}^{p} \theta_j y_{t-j} + \sum_{i=1}^{q} \theta_j \varepsilon_{t-j} + \varepsilon_t \quad (6)$$

ARIMA-Kalman Filter Prediction

According to Kalman (1960), the Kalman filter can be used to predict the state of a system that changes over time by minimizing estimation errors. This process involves two main steps: prediction and updating.

Prediction Steps

State Estimation at Time

To estimate the state at time, you can use the following formula:

$$\hat{x}_t^- = F\hat{x}_{t-1} + Bu_t \quad (7)$$

Error Covariance Estimation

To estimate the error covariance, you can use the following formula:

$$P_t^- = FP_{t-1}F^T + Q \quad (8)$$

Update Steps

Calculating Kalman Gain

To calculate the Kalman gain, you can use the following formula:

$$K_t = P_t^- H^T (HP_t^- H^T + R)^{-1} \quad (9)$$

Updating State Estimates

To estimate the state, you can use the following formula:

$$\hat{x}_t = \hat{x}_t^- + K_t(z_t - H\hat{x}_t^-) \quad (10)$$

Updating Error Covariance

To update the error covariance, you can use the following formula:

$$P_t = (I - K_t H)P_t^- \quad (11)$$

Model Evaluation

The three evaluation metrics that will be used are mean absolute error (MAE) and root mean squared error (RMSE).

Mean Absolute Error

MAE measures the average absolute error between the predicted and actual values, giving a clear picture of how much the prediction is wrong in the same units as the data.

$$MAE = \frac{1}{n} \sum_{t=1}^{n} |y_t - \hat{y}_t| \quad (12)$$

Root Mean Squared Error

RMSE calculates the square root of the average of the squared errors between the actual and predicted values. RMSE imposes a larger penalty for larger errors, making it more sensitive to outliers.

$$RMSE = \sqrt{\frac{1}{n} \sum_{t=1}^{n} |y_t - \hat{y}_t|} \quad (13)$$

RESULTS AND DISCUSSION

Stationary Test of Rainfall Data

The results of the Augmented Dickey-Fuller (ADF) test in Figure 2 on the time series data of rainfall in Medan City in 2013 – 2023 show that the statistical value of the ADF test is -6.5853 with a lag order of 5 and a p-value of 0.01. Because the p-value is smaller than the significance level of 0.05, the null hypothesis (H0), which states that the data is not stationary, is rejected. Thus, the data can be considered stationary. This means that the time series data does not have a trend or seasonal pattern that significantly affects the mean, variance, or autocorrelation, making it suitable for further analysis to carry out a prediction model.

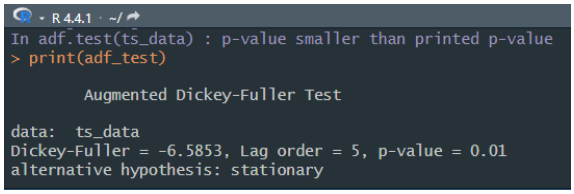

Figure 2. Stationary test using ADF.

Homogeneity Test of Rainfall Data

The results of the homogeneity test using Pettitt's Test in Figure 3 on the time series data of rainfall in Medan City in 2013 – 2023 show that the U* statistic value is 1305 with a p-value of 0.02433, which is smaller than the significance level of 0.05. This indicates that the null hypothesis (H0), which states that there is no change point in the data, can be rejected, so that there is a significant change point in the distribution of rainfall. The change point was detected at time 63, which showed a significant change in the rainfall pattern at that time. Therefore, the data is homogeneous data.

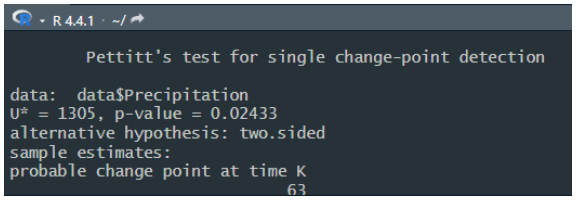

Figure 3. Homogeneity test using Pettitt's test.

ARIMA Modeling

Based on the output results from auto ARIMA, the models selected for the rainfall time series data are ARIMA (0,1,1) and (1,0,0). This model consists of a non-seasonal component (0,1,1), indicating no AR component, one differentiation to achieve stationarity, and one MA component. In addition, there is a seasonal component (1,0,0), reflecting one seasonal AR component, without seasonal differentiation, and without a seasonal MA component, with an annual seasonal pattern of 12 periods/month. The model will be used in ARIMA prediction and filtered by the Kalman filter method.

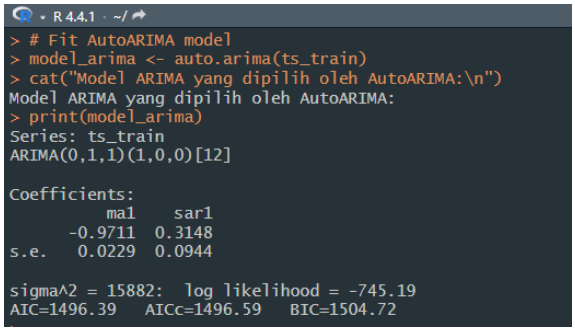

Figure 4. ARIMA modeling using AutoARIMA.

ARIMA-Kalman Prediction

Based on the graphs in Figure 5 and Table 1, the prediction results using the ARIMA and ARIMA-Kalman models show that both models can follow the actual rainfall pattern, but ARIMA-Kalman is more accurate in capturing fluctuations. In the graph, the green line (ARIMA-Kalman) is closer to the blue line (actual) than the red line (ARIMA), especially in periods with significant changes in rainfall. This can also be seen in the table, where the ARIMA-Kalman prediction value is closer to the actual data in almost every month. For example, in July 2023, the actual rainfall of 302.8 mm is predicted to be 241.6 mm by ARIMA and 265.4 mm by ARIMA-Kalman, indicating that ARIMA-Kalman provides closer results to reality.

Overall, the combination of ARIMA with the Kalman algorithm has been proven to be able to improve prediction accuracy compared to ARIMA alone. In months such as December 2023, where actual rainfall reaches 326.5 mm, ARIMA predicts 295.4 mm, while ARIMA-Kalman provides a closer prediction, namely 292.3 mm. By using historical data on Medan city rainfall from 2013 – 2022 as a basis, ARIMA-Kalman successfully captures complex rainfall patterns, making it a superior method for prediction.

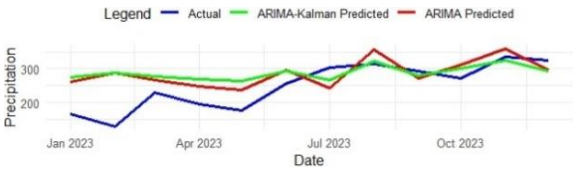

Figure 5. Plot of actual rainfall vs ARIMA vs ARIMA-Kalman.

Table 1. Prediction results using ARIMA and ARIMA-Kalman.

Month	Year	Actual	ARIMA prediction	ARIMA-Kalman prediction
1	2023	164.5	261.4100122	275.303027
2	2023	128.4	287.5098831	288.3529624
3	2023	228.3	267.4548556	278.3254487
4	2023	196.1	247.5887295	268.3923856
5	2023	175.1	236.6324508	262.9142463
6	2023	256.4	294.7825854	291.9893136
7	2023	302.8	241.6383368	265.4171893
8	2023	315.7	355.9866253	322.5913335
9	2023	293.4	270.6976623	279.946852
10	2023	271	312.7596979	300.9778699
11	2023	335.5	359.8591032	324.5275725
12	2023	326.5	295.4122566	292.3041492

Prediction Result Validation

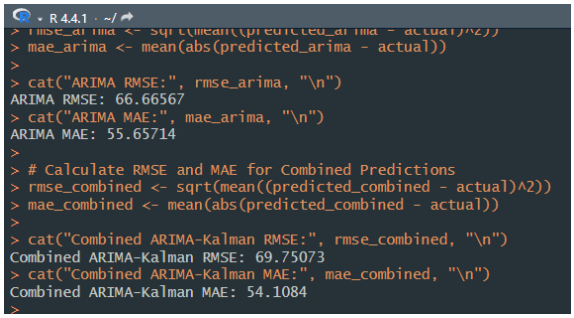

Figure 6. Validation of ARIMA and ARIMA-Kalman prediction results.

The validation results in Figure 6 show that the RMSE and MAE values for the ARIMA model are 66.67 and 55.66, respectively, while for the ARIMA-Kalman model they are 69.75 and 54.11, respectively. Although ARIMA has a lower RMSE than ARIMA-Kalman, the MAE value of ARIMA-Kalman is smaller, indicating that the average prediction of ARIMA-Kalman is closer to the actual value. The higher RMSE of ARIMA-Kalman is likely due to its sensitivity to large prediction errors at some data points.

Overall, ARIMA-Kalman can be considered superior because the smaller MAE value indicates that this model is more consistent and provides prediction results that are closer to the actual data, making it a better choice for rainfall prediction in Medan City.

CONCLUSION

Based on the research discussion, it can be concluded that the monthly rainfall data from BMKG for 2013 – 2023 is stationary and homogeneous. The models used in this ARIMA-Kalman study are ARIMA (0,1,1) and (1,0,0). The ARIMA-Kalman prediction model is superior to the ARIMA model alone.

REFERENCES

1. Siregar, N. A. (2022). Peramalan curah hujan di Kota Medan menggunakan

metode support vector regression. *J. Informatics Data Sci.*, **1**(1), 7–9.
2. Anggraini, N., Pangaribuan, B., Siregar, A. P., Sintampalam, G., Muhammad, A., Damanik, M. R. S., & Rahmadi, M. T. (2021). Analisis pemetaan daerah rawan banjir di Kota Medan Tahun 2020. *Jurnal Samudra Geografi*, **4**(2), 27–33.
3. Selamat, I. K. & Setyawan, Y. (2023). Prediksi curah hujan perbulan di Kota Yogyakarta Periode 2015 – 2019 menggunakan metode *autoregressive integrated moving average* (ARIMA) dan Kalman filter (Studi kasus : Data curah hujan Tahun 2015 – 2019). *J. Stat. Ind. dan Komputasi*, **8**(1), 15–31.
4. Aprilia, M. & Desviona, N. (2021). The implementation of a filter Kalman method forecasting rainfall obtained through model ARIMA in Kota Jambi. *Nucleus*, **2**(2), 69
5. Zulfi, M., Hasan, M., & Purnomo, K. D. (2018). The development rainfall forecasting using Kalman filter. *Journal of Physics: Conference Series*, **1008**(1), 012006.
6. Ananda, E. Y. P. & Wahyuni, M. S. (2021). Rainfall forecasting model using ARIMA and Kalman filter in Makassar, Indonesia. *Journal of Physics: Conference Series*, 2123(1), 012044.
7. Rusdi, R. (2011). Uji Akar-Akar Unit dalam Model Runtun Waktu Autoregresif. *Statistika*, **11**(2), 67–78.
8. Ruhiat, D., Andiani, D., & Kamilah, W. N. (2020). Forecasting data runtun waktu musiman menggunakan metode singular spectrum analysis (SSA). *Teorema: Teori dan Riset Matematika*, **5**(1), 47–60.
9. Samsiah, D. N. (2008). Analisis data runtun waktu menggunakan model ARIMA (p, d, q). *Skripsi UIN Sunan Kalijaga, Yogyakarta*.
10. Laamena, N. S. (2019). Prakiraan harga rumah di Kota Semarang dengan model deret waktu. *Jurnal Satya Informatika*, **4**(01), 41–52.
11. Rianto, M. & Yunis, R. (2021). Analisis runtun waktu untuk memprediksi jumlah mahasiswa baru dengan model random forest. *Paradigma*, **23**(1), 70–74.

IPC

Indonesian Physics Communication

Department of Physics, Universitas Riau, Pekanbaru, Indonesia
p-ISSN 1412-2960 | e-ISSN 2579-521X

Vol. 22 | No. 1
March 2025

Web: https://kfi.ejournal.unri.ac.id
E-mail: kfi@ejournal.unri.ac.id

Empirical orthogonal functions (EOF) analysis of spatial patterns of dominant variability in the Indian Ocean

Willy Bonanja Manik, Yahya Darmawan*, Munawar Munawar, Nardi Nardi, Fendy Arifianto, Ervan Ferdiansyah
Indonesia College of Meteorology, Climatology and Geophysics (STMKG), Tangerang 15221, Indonesia

*Corresponding author: yahya.darmawan@bmkg.go.id

ABSTRACT

The Indian Ocean plays a crucial role in the global climate system, particularly in influencing the seasons in Indonesia. Sea surface temperature (SST) variability in the Indian Ocean affects rainfall patterns, extreme events, such as droughts and floods, in Indonesia. This study analyzes SST variability during the dry season (June – July – August, JJA) and rainy season (December – January – February, DJF) using satellite and reanalysis data from 1981 to 2023 with the empirical orthogonal function (EOF) method. The analysis shows that the dominant SST variability pattern during JJA is related to the Indian Ocean dipole (IOD), which influences rainfall and temperature patterns in Indonesia. In DJF, SST variability is more associated with the Asian-Australian monsoon, affecting rainfall patterns and the potential for floods. This research enhances the understanding of climate dynamics in the Indian Ocean and its impact on Indonesia, and it can be used to predict extreme climate events associated with SST variability.

Keywords: EOF; Indian Ocean; IOD; sea surface temperature (SST)

Received 29-01-2025 | Revised 10-03-2025 | Accepted 26-03-2025 | Published 31-03-2025

INTRODUCTION

The Indian Ocean is the third largest ocean in the world and plays an important role in the global climate system. Sea surface temperature (SST) in the Indian Ocean shows significant variability, influenced by various factors such as monsoon winds, ocean currents, and atmosphere-ocean interactions [1]. Climate phenomena such as the Indian Ocean dipole (IOD) and el niño-southern oscillation (ENSO) also contribute to SST variability in this region. SST variability in the Indian Ocean has a broad impact on weather and climate conditions in various parts of the world, including Indonesia.

Indonesia, as an archipelagic country located between the Indian Ocean and the Pacific Ocean, is very vulnerable to the impacts of SST variability in the Indian Ocean. Changes in SST can affect monsoon wind patterns, rainfall intensity and distribution, and extreme events such as floods and droughts in Indonesia [2]. Therefore, a deep understanding of SST variability in the Indian Ocean, especially during periods that affect the seasons in Indonesia, is very important to improve climate prediction and disaster mitigation capabilities.

This study aims to analyze SST variability in the Indian Ocean with a focus on the dry season (June – July – August, JJA) and rainy season (December – January – February, DJF) using data from 1981 to 2023. This period was chosen because it represents the contrast of climate conditions in Indonesia which are influenced by the monsoon. In the month of JJA, the dry eastern monsoon dominates causing a decrease in rainfall in Indonesia. Conversely, the western monsoon brings moist air from the Indian Ocean which causes an increase in rainfall in Indonesia in the month of DJF.

The empirical orthogonal function (EOF) method will be used to identify the dominant patterns of SST variability in that month. The EOF method is effective in reducing data dimensions and revealing the dominant spatial patterns of SST variability [3]. As shown by Dipo in 2011, the EOF method can be used to analyze the characteristics of physical

oceanography in the Indian Ocean, including SST variability [4]. It also shows that SST variability in the Indian Ocean, especially IOD, can be influenced by global warming [5].

By identifying the dominant patterns of SST variability in the Indian Ocean in DJF and JJA, this study is expected to improve understanding of climate dynamics in the Indian Ocean and its impacts on Indonesia, as well as to develop adaptation and mitigation strategies against climate change.

RESEARCH METHODS

Research Method This study aims to analyze the variability of SST in the Indian Ocean with a focus on the rainy season (DJF) and dry season (JJA) in Indonesia using the EOF method. This method was chosen because of its ability to reduce the dimensions of complex data and reveal the dominant spatial patterns of SST variability, as has been proven in various studies [1, 3, 4].

The data used in this study are monthly SST data from 1981 to 2023 obtained from the National Oceanic and Atmospheric Administration (NOAA). The SST data used has a spatial resolution of $1^{o} \times 1^{o}$.

Data Processing

- Data selection: Monthly SST data will be selected and grouped based on the DJF and JJA seasons.
- Seasonal average calculation: Monthly SST data will be averaged for each DJF and JJA season period each year.

Data Analysis

EOF Analysis

- The EOF method will be applied to the seasonal mean SST data (DJF and JJA) to identify the dominant patterns of SST variability in the Indian Ocean.
- EOF will generate a series of orthogonal modes, where each mode represents an independent pattern of variability.
- The eigenvalues correlated with each EOF mode will be calculated to determine how much the mode contributes to the total variance of the data.
- The EOF modes with the largest eigenvalues will be further analyzed, as these modes are the dominant modes that explain most of the SST variability.

Interpretation of Spatial Patterns

- The spatial patterns of the dominant EOF modes will be visualized in the form of maps to identify areas in the Indian Ocean that have similar SST variability.
- These spatial patterns will be interpreted to understand the characteristics of SST variability in the Indian Ocean during the DJF and JJA periods.

Data processing and EOF analysis will be carried out using Python software using the Pycharm application with appropriate libraries for data analysis and visualization.

RESULTS AND DISCUSSION

EOF in statistics is a multivariate analysis technique used to identify dominant patterns in a dataset spatially and temporally. The EOF method determines dominant patterns in three stages, namely;

- Covariance Matrix: This matrix shows the correlation between SST anomalies at each pair of grid locations.
- Eigenvalue Decomposition: The covariance matrix is decomposed into eigenvalues and eigenvectors. Eigenvalues represent variance by each EOF mode, while eigenvectors represent spatial patterns
- Dominant Mode Selection: Then the EOF modes will be sorted based on the eigenvalue value. The largest eigenvalue explains the largest variance in the data and is considered the dominant mode.

So that finally this EOF analysis will produce a percentage of dominant variants,

spatially dominant patterns and temporally dominant patterns.

June – July – August (JJA)

Dominant Pattern I

This dominant pattern I EOF shows a dominant variant percentage of 45.8% with an average increase in SST in the western Indian Ocean. This is indicated by the solid red color pattern in Figure 1. This pattern indicates a positive IOD which results in an increase in SST in the western Indian Ocean.

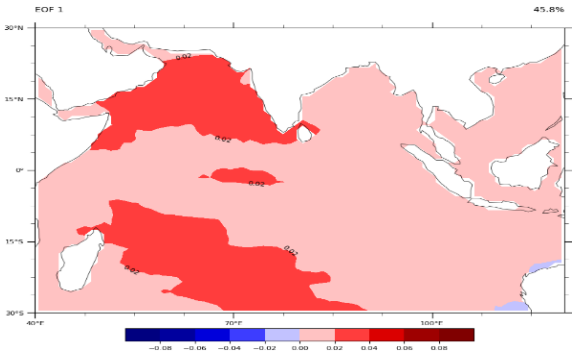

Figure 1. Spatial dominance pattern I of the Indian Ocean EOF in JJA (1981 – 2023).

Dominant Pattern II

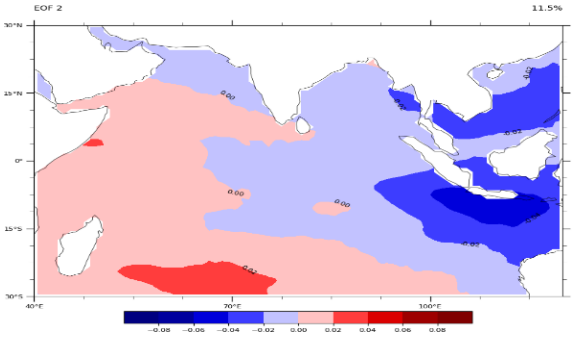

Figure 2. Spatial dominance pattern II of the Indian Ocean EOF in JJA (1981 – 2023).

This dominant pattern II EOF has a dominant variant percentage of 11.5%. There is a high decrease in SST in the eastern Indian Ocean and the southern parts of Arabia and India. This pattern is more complex than the previous pattern because it can be caused by various factors. These factors can be due to the presence of the Asian moonsun, ocean currents or even the presence of equatorial currents.

Dominance Pattern III

This pattern shows a percentage of variance of 7.9% with a significant decrease in SST in the central area of the Indian Ocean, while around it there is a significant increase in SST. This pattern can be caused by local atmospheric circulation or even the influence of the Pacific Ocean, for example the influence of ENSO.

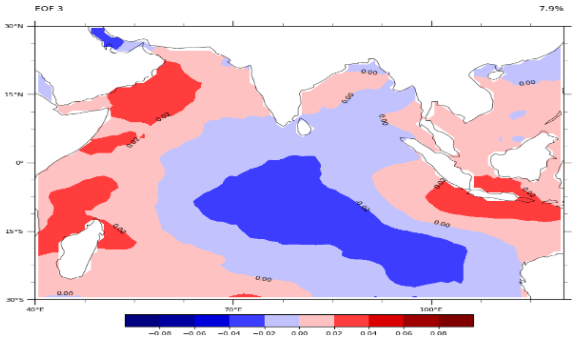

Figure 3. Spatial dominance pattern III of the Indian Ocean EOF in JJA (1981 – 2023).

December – January – February (DJF)

Dominance Pattern I

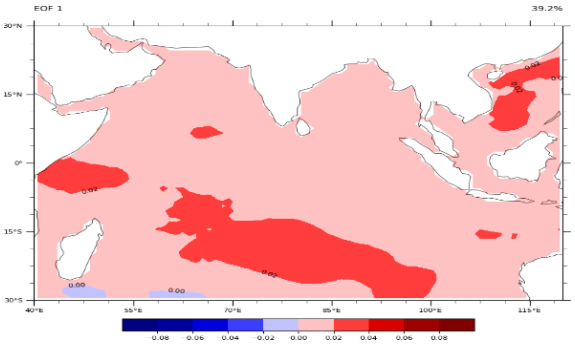

Figure 4. Spatial dominance pattern I of the Indian Ocean EOF in DJF (1981 – 2023).

Figure 4 shows a dominant percentage of variance of 39.2% with a significant and even increase in SST in the central Indian Ocean. This pattern likely indicates the influence of the Asian-Australian Monsoon. During the DJF season, this monsoon is in its active phase, which is characterized by strong westerly winds in the Indian Ocean. Another possibility is the influence of the sun's position, because in the DJF month the sun is in the southern hemisphere (BBS).

Dominance Pattern II

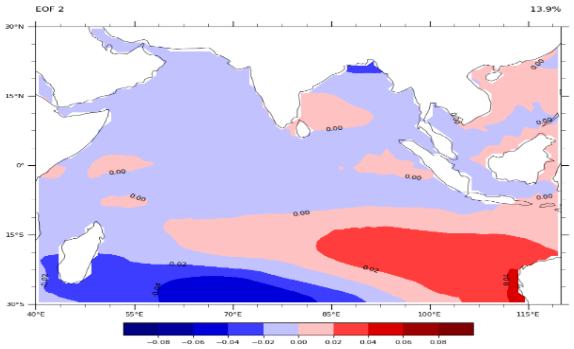

Figure 5. Spatial dominance pattern II of the Indian Ocean EOF in DJF (1981 – 2023).

Figure 5 shows a dominant percentage of 13.9% and a more localized SST distribution. This pattern shows variations in the intensity and pattern of the monsoon winds from year to year. Although the Asia-Australia monsoon is in its active phase, these variations can affect ocean circulation and SST distribution. Other factors that may play a role are local atmospheric interactions and the influence of other climate phenomena such as IOD and ENSO.

Dominance Pattern III

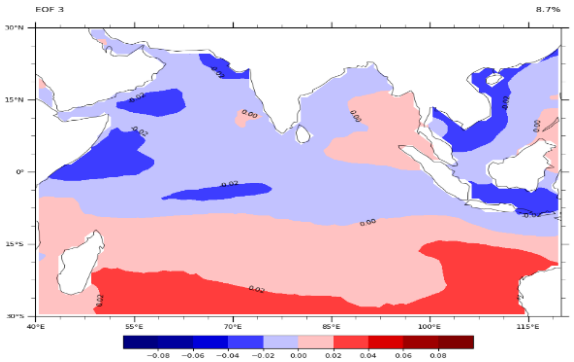

Figure 6. Spatial dominance pattern III of the Indian Ocean EOF in DJF (1981 – 2023).

Figure 6, EOF 3 shows a dominant percentage of 8.7%. It is seen that the dominant decrease in SST occurs in the northern part of the ocean while there is a significant increase in SST evenly in the southern part of the Indian Ocean. This pattern is likely influenced by the Madden-Julian Oscillation (MJO), which can modulate rainfall and wind patterns in the Indian Ocean and have an impact on SST.

CONCLUSION

EOF analysis of SST in the Indian Ocean produces dominant patterns of variability in both JJA and DJF months. In JJA, the IOD pattern is more dominant, while in DJF the Asia-Australia monsoon pattern is more prominent. In addition to these dominant patterns, there are also other more complex and localized patterns of variability. This is influenced by various factors such as variations in the west and east monsoons, ocean currents, atmospheric interactions, and large-scale climate phenomena such as ENSO and MJO.

REFERENCES

1. Sukresno, B. (2010). Empirical orthogonal functions (EOF) analysis of SST variability in Indonesian water concerning with ENSO and IOD. *ISPRS Arch.*, **38**(8), 116–121.
2. Balbeid, N., Atmadipoera, A. S., & Koropitan, A. F. (2015). Response of sea surface temperature (SST) and chlorophyll-a on Madden Julian oscillation (MJO) in Indonesian seas. *Jurnal Ilmu dan Teknologi Kelautan Tropis*, **7**(2).
3. Messié, M. & Chavez, F. (2011). Global modes of sea surface temperature variability in relation to regional climate indices. *J. Clim.*, **24**(16), 4314–4331.
4. Dipo, P., Nurjaya, I. W., & Syamsudin, F. (2011). Karakteristik oseanografi fisik di perairan Samudera Hindia Timur pada saat fenomena Indian Ocean dipole (IOD) fase positif tahun 1994/1995, 1997/1998 dan 2006/2007. *Jurnal Ilmu dan Teknologi Kelautan Tropis*, **3**(2), 71–84.
5. Zhou, Z. Q., Xie, S. P., & Liu, Q. (2013). Indian Ocean dipole response to global warming: A multi-member study with CCSM4. *J. Ocean Univ. China*, **12**, 209.

IPC

Indonesian Physics Communication

Department of Physics, Universitas Riau, Pekanbaru, Indonesia
p-ISSN 1412-2960 | e-ISSN 2579-521X

Vol. 22 | No. 1
March 2025

Web: https://kfi.ejournal.unri.ac.id
E-mail: kfi@ejournal.unri.ac.id

Visualization and simulation of ZnO microstructure with various crystal structures and doping compositions based on XRD patterns using VESTA

Dikri Aminnurdin*, Ari Sulistyo Rini
[1]Department of Chemical Engineering, Universitas Riau, Pekanbaru 28293, Indonesia
[2]Department of Physics, Universitas Riau, Pekanbaru 28293, Indonesia

*Corresponding author: dikri.aminnurdin3820@student.unri.ac.id

ABSTRACT

Crystal structure visualization and X-ray diffraction pattern simulation of various types of ZnO microstructures have been successfully carried out using the VESTA software program. The purpose of this study was to obtain the relationship between the shape of the structure, microstructure, and composition to changes in the pattern and peak diffraction. The software program produces information on the shape of the crystal structure and representative X-ray diffraction patterns for ZnO microstructures. This program requires input in the form of coordinates of each constituent atom, lattice parameters, and spatial symmetry. The output obtained is a graph of the diffraction pattern and crystal structure that provides an overview of the profile and type (phase) of the ZnO microstructure. The results showed that the peak position and intensity of the diffraction pattern were influenced by the arrangement of atoms in the unit cell. In variations in structure and microstructure, the position of the diffraction peak provides a different picture for each type of structure depending on the arrangement of atoms in the unit cell, where each crystal structure has a different position and spatial symmetry, resulting in different diffraction patterns. The nanorod structure has a monoclinic crystal system ($a \neq b \neq c$) with a space group of C 2 / c and lattice parameters a = 15.4170 Å, b = 25.3560 Å, and c = 14.3840 Å. The nanowire structure has a triclinic crystal system ($a \neq b \neq c$) with lattice parameters a = 12.0380 Å, b = 2.4910 Å, c = 16.8890 Å and a space group of P-1 and is the simplest form of symmetric lattice. The nanoflower structure has an orthorhombic crystal system ($a \neq b \neq c$) with lattice parameters a = 9.47310 Å, b = 13.52960 Å, c = 29.0220 Å and space group P b c a.

Keywords: RIETAN-FP; simulation; VESTA; visualization; X-ray diffraction

Received 14-11-2024 | Revised 07-02-2025 | Accepted 25-03-2025 | Published 31-03-2025

INTRODUCTION

Zinc oxide (ZnO) nanoparticles are one of the most widely used n-type semiconductor metal oxide materials due to their multifunctional morphological, photonic, and spintronic properties. This is characterized by a wide direct band gap of 3.37 eV and a high excitation energy of 60 meV. ZnO is widely used because of its characteristics [1].

The characteristics of the material structure are very important to know to analyze materials. The crystal structure of a material is closely related to the properties of the material. The properties of the material are built on two main concepts, namely the concept of the atomic structure of the crystal and the concept of material treatment. The concept of material treatment explains the interactions between atoms and changes in atomic structure. Knowledge of the crystal structure of a material can indirectly provide information on the properties of the material [2].

The crystal structure can be determined manually or with a computer program based on the X-ray diffraction pattern. Determination of the crystal structure manually is done by determining the lattice constant, the adopted space group, and the position of the atoms in the crystal unit cell based on X-ray Scattering data. However, sometimes problems arise when different atoms and very close atomic numbers have almost the same scattering so that their peaks overlap. Therefore, experts try to develop computer analysis methods to interpret the structure of the crystal based on Bragg's Law.

The advantage of using a computer program for analysis is that calculations can be done faster, saving time and the final results given by the computer are also reliable. The structural analysis that is often done is based on structural refinement using the Rietveld method [3].

The depiction of crystal structures is still very rarely reported. Simulation of X-ray diffraction patterns of various natural zeolite minerals has been carried out by [4]. The simulation results in the form of diffraction pattern profile graphs and crystal structure data information that were carried out showed significant and representative results from the seven zeolite phases simulated in previous studies by simulating X-ray diffraction patterns with the RIETAN-FP program. Visualization of crystal structures and simulation of X-ray diffraction patterns using VESTA have been carried out by [5], using perovskite $Ba_{1-x}Sr_xTiO_3$ ceramic crystals as the object of their research. The results of the study indicate that the peak position and intensity of the diffraction pattern are influenced by the arrangement of atoms in the unit cell. The addition of impurity atoms such as Sr on the Ba side in $BaTiO_3$ causes changes in the structure of $BaTiO_3$.

In this study, visualization of various ZnO crystal microstructures will be carried out using software by simulating X-ray diffraction patterns using the VESTA and RIETAN-FP software programs. The material targeted for the study is the ZnO microstructure. The visualization and simulation carried out were made with three different categories of variations including structural variations, composition variations, and microstructure variations. Based on the visualization of the ZnO microstructure obtained, it is expected to be used as a reference for research in analyzing the structure of materials whose crystal structure is not yet known.

LITERATURE REVIEW

Zinc Oxide (ZnO)

ZnO is an inorganic semiconductor that is generally in powder form and is non-toxic and has high electron mobility and thermal stability. ZnO is a semiconductor formed by a combination of group IIB (element Zn) and VIA (element O) groups. Its ionization energy lies between ionic semiconductors and covalent semiconductors [6].

Like most group II-VI materials, the ZnO bond is ionic ($Zn^{2+} – O^{2-}$) with a radius of 0.074 nm for Zn^{2+} and 0.140 nm for O^{2-}. This property explains the preferential formation of a hexagonal structure rather than zincblende and the strong piezoelectric properties of ZnO are caused by the polar Zn–O bond, where the zinc and oxygen planes are electrically charged.

ZnO has a structure that can crystallize into three main forms, namely wurzite, zincblende and rocksalt [7]. The cubic rocksalt structure has cubic crystals with lattice parameters a = b = c = 4.1440 Å and space group F-m3m. The diffraction pattern of cubic rocksalt ZnO produces maximum peak intensity at the three highest peaks I (200) > I (220) > I (111). The cubic rocksalt structure is formed at high temperatures. The ZnO structure in the form of cubic rocksalt has a band gap energy of 2.7 eV with a lattice constant between 4.271 – 4.294 Å. The structure of zinc blende is one of the various structures produced from ZnO semiconductor material, with characteristics where the sides are not the same as each other. In general, the zinc blende structure is formed at high pressure and high temperature conditions which have lattice parameters a = b = c = 5.39 Å and space group F43m. The wurtzite structure is the most thermodynamically stable ZnO crystal structure. The ZnO phase has a hexagonal crystal structure (space group P63mc) with lattice parameters a = b = 3.246 Å and c = 5.198 Å, $\alpha = \beta = 90^o$, and $\gamma = 120^o$.

Crystal Structure

The properties and characteristics of solids are determined by the crystal structure contained in the material. Crystals are a type of atomic structure in which atoms are regularly and periodically (repeatedly) arranged in a

three-dimensional arrangement. Each atom is bound to each other at the closest distance to each other. The basic pattern or pattern of the crystal structure can be shown in a simple form called a lattice. The lattice is the position of the atoms that form the crystal. The periodic lattice arrangement forms a three-dimensional crystal system or crystal structure.

The concept of the Bravais lattice is used to formally define the crystal arrangement and its boundaries (limited). Crystals consist of one or more atoms, called bases or motifs, at each lattice point. The basis can consist of atoms, molecules, or strings of solid polymers, and the lattice provides the location of the basis.

Currently, there are only 7 types of crystal systems and 14 Bravais lattices [8] which are classified based on the number of crystal axes, the location of the crystal axes in relation to each other, the parameters used for each crystal axis and the number of space groups adopted. The seven crystal systems are as shown in Table 1.

Table 1. Crystal systems, lattice parameters, Bravais lattices and number of space groups.

Crystal system	Lattice parameters	Bravais lattice	Number of room groups
Triclinic	$a \neq b \neq c$ $\alpha \neq \beta \neq \gamma$	P	2
Monoclinic	$a \neq b \neq c$ $\alpha = \beta = 90° \neq \gamma$	P, C	13
Orthorhombic	$a \neq b \neq c$ $\alpha = \beta = \gamma = 90°$	P, I, C, F	59
Tetragonal	$a = b \neq c$ $\alpha = \beta = \gamma = 90°$	P, I	68
Cube	$a = b = c$ $\alpha = \beta = \gamma = 90°$	P, I, F	36
Rhombohedral / Trigonal	$a = b = c$ $120° > \alpha = \beta = \gamma \neq 90°$	R	25
Hexagonal	$a = b \neq c$ $\alpha = \beta = 90°, \gamma = 120°$	P	27

X-Ray Diffraction (XRD)

XRD is a method used to determine crystal structure, phase changes and degree of crystallinity. X-ray diffraction by atoms arranged in a crystal will produce different patterns depending on the configuration formed by the atoms in the crystal [9].

The principle of XRD is based on X-ray diffraction, scattering of light with a wavelength of λ when passing through a crystal lattice with an angle of incidence of θ and a distance between crystal planes of d (Figure 2.3). The data obtained from the XRD characterization method are the scattering angle (Bragg angle) and intensity. Based on diffraction theory, the diffraction angle depends on the width of the lattice gap (distance between lattices) so that it affects the diffraction pattern, while the intensity of the diffracted light depends on how many crystal lattices have the same orientation.

The basic principle used to determine the crystal system is by using the Bragg's law equation:

$$2d \sin\theta = n\lambda \quad (1)$$

where, d is the distance between the lattice planes, θ is the measurement angle, n is the index, while λ is the wavelength of the X-ray.

The height of the diffraction peak on the Miller Index is determined by the ratio of the wavelength of the light to the distance between the crystal planes. The greater the difference between the refractive index value of the crystal and the refractive index value of the surrounding media, the shorter the wavelength of the light, so the higher the diffraction peak on the Miller Index. The greater the distance

between the crystal planes, the shorter the wavelength of the diffraction that will occur, so the higher the diffraction peak on the Miller Index. Therefore, the determinants of the height of the diffraction peak on the Miller Index are the refractive index value of the crystal and the distance between the crystal planes. In all crystal systems except the hexagonal crystal system, the crystallographic planes are determined using three Miller Indices, namely (hkl). Every two parallel planes have identical similarities and indices.

The hexagonal lattice parameters a and c are determined by calculations using the Cohen method based on the distance data between the crystal planes, d_{hkl}, obtained from the XRD peaks. For hexagonal structures using:

$$d_{hkl}^{-2} = \frac{4(h^2 + hk + k^2)}{3a^2} + \frac{l^2}{c^2} \quad (2)$$

Rietveld Analysis

The Rietveld method is a method published by Rietveld in 1967 to analyze diffraction patterns whose peaks overlap using the least squares principle. The Rietveld method can now be used to analyze neutron diffraction patterns and XRD on single crystal and polycrystalline samples. This method can also be used as a tool to characterize crystalline materials to extract various chemical and microstructural information, for example, analyzing phase composition and determining lattice parameters accurately [10].

Rietveld method software that can be used to analyze crystal structures includes XRS-82 (The X-rays Rietveld System-82). FullProf, RIETAN-FP and GSAS (general structure analysis system) software can be obtained from the internet for free and can be operated on a personal computer using the disk operating system (DOS) or Unix operating system.

VESTA

VESTA is a three-dimensional visualization system in the C++ programming language based on OpenGL technology for electronic and structural analysis developed by Koichi Momma and Fujio Izumi during 2001 – 2004. 3D visualizations that can be done include structural models, volumetric data ("voxel" data), and crystal morphology. Objects such as atoms, bonds, coordination polyhedra, isosurfaces can be rotated, scaled, and translated quickly in three dimensions. The scalability of VESTA is very high which allows it to handle an almost unlimited number of impractical objects such as atoms, bonds, polyhedra and polygons on isosurfaces as long as the memory capacity is sufficient. The image boundary is defined by the range along the x, y and z axes and the lattice plane [11].

VESTA can display crystal structures such as ball and stick, space-filling, polyhedral, wireframe, stick, and thermal-ellipsoid models with a variety of coloring features that indicate the quantity of each point on the surface. VESTA can be run on Microsoft Windows, Mac OS X, and Linux. The VESTA software program can handle multiple data in the same window, using a "tabbed" user interface. VESTA also supports multiple windows, each containing multiple tabs corresponding to files. VESTA can read files in 36 formats such as CIF, ICSD, and PDB and output files in 11 formats such as CIF and PDB.

VESTA can be directly connected to RIETAN-FP so that powder diffraction patterns can be simulated easily. Selecting the "Powder Diffraction Pattern" item under the "Utilities" menu causes a series of procedures to be run by VESTA as if they were implemented in VESTA such as the creation of input files, * .ins for RIETAN-FP, the execution of RIETAN-FP, and the graphical representation of the resulting data in * .itx files with graphic programs such as Igor Pro and gnuplot.

VESTA acts as a mediator between structural analysis and electronic structure calculations. All the advanced features and high performance contained in the VESTA software program are expected to contribute greatly to crystal and electronic structure investigations.

Crystal structures are visualized by placing atoms at specific positions in the unit cell. These positions are usually expressed in fractional coordinates (u,v,w), which are related to Cartesian coordinates by a transformation, e.g. r = (x,y,z) is the atomic position in Cartesian coordinates, r_frac = (u,v,w) is the position in fractional coordinates. Then the relationship between the two is:

$$\begin{pmatrix} x \\ y \\ z \end{pmatrix} = \begin{matrix} a & b\cos(\gamma) & c\cos(\beta) \\ 0 & b\sin(\gamma) & c\dfrac{\cos(\alpha)-\cos(\beta)\cos(\gamma)}{\sin\gamma} \\ 0 & 0 & \dfrac{cV}{} \end{matrix} \begin{pmatrix} u \\ v \\ w \end{pmatrix} \quad (3)$$

where, V is the volume of the unit cell given:

$$V = \sqrt{1-\cos^2(\alpha)-\cos^2(\beta)-\cos^2(\gamma)+2\cos(\alpha)\cos(\beta)\cos(\gamma)} \quad (4)$$

VESTA also utilizes crystal symmetry elements, such as rotation axes, mirrors, and inversion centers, which are described using symmetry matrices. These symmetries are important in determining the repetition of crystal structures in space.

RIETAN-FP

The RIETAN-FP simulator program was created by F. Izumi and Y. Hamaguchi and installed on a Macintosh Computer. The method used is structural analysis with the Rietveld technique by entering two types of data, namely crystal structure parameter data and intensity. Crystal structure parameter data is input data for a proposed calculation model, while intensity data comes from the X-ray diffraction intensity of a sample. For simulation analysis, intensity data from XRD does not need to be entered. The results of the RIETAN-FP program processing will provide information in the form of structural parameter data, calculated intensity data and diffraction pattern profiles.

The RIETAN-FP simulation process is carried out by assuming that each type of phase has its own lattice parameters, space groups, and atomic positions in the unit cell as input data. Complete data on crystal structure parameters are taken from the JCPDS database, which is a collection body for X-ray diffraction experimental data from various sources whose origins and data accuracy can be traced. This database can be found in software which is an easy-to-use software for phase identification from powder diffraction data. In the MATCH!4 software there is a database containing various reference patterns.

RESEARCH METHODS

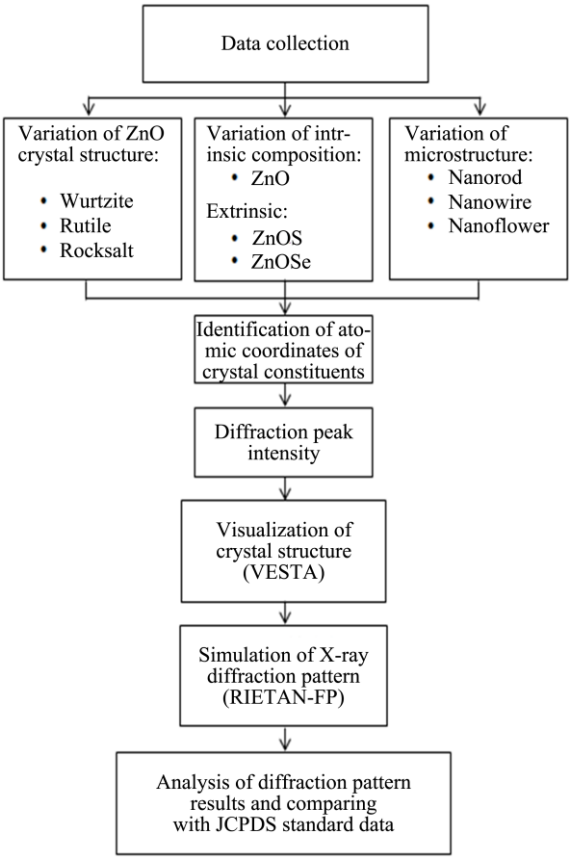

Figure 1. Research flow diagram.

Visualization was performed using VESTA Software with variations in crystal structure (wurtzite, rutile and rock salt), atomic composition (ZnO, ZnO;S and ZnO;Se) and microstructure (nanorod, nanowire and nanoflower). The visualization results were then simulated to obtain the diffraction pattern. The diffraction pattern was then compared with real data and the simulation results were analyzed in the form of crystal lattice parameters, structural shape, and diffraction peak positions.

RESULTS AND DISCUSSION

Crystallographic Data

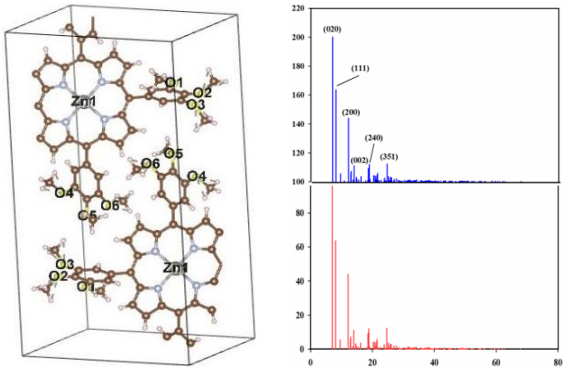

(a) (b)

Figure 2. (a) Visualization of the nanorod crystal microstructure and (b) its diffraction pattern.

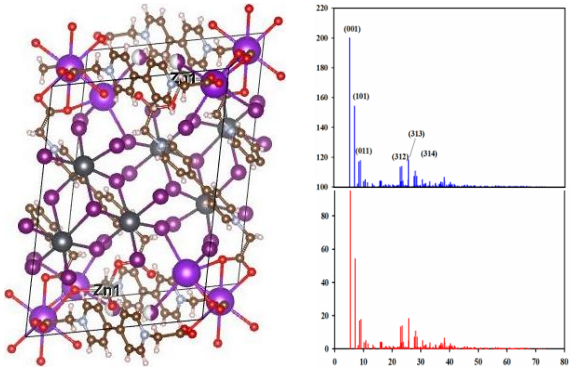

(a) (b)

Figure 3. (a) Visualization of the nanowire crystal microstructure and (b) its diffraction pattern.

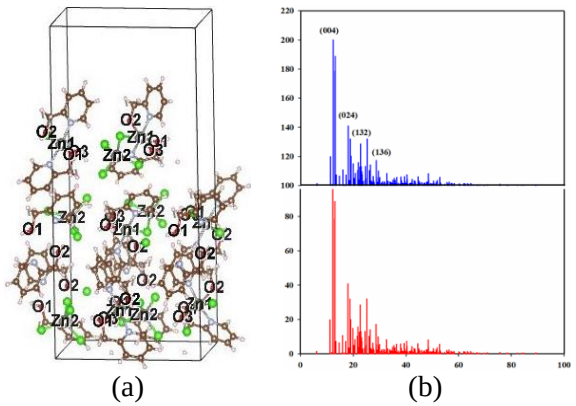

(a) (b)

Figure 4. (a) Visualization of the nanoflower crystal microstructure and (b) its diffraction pattern.

The discussion in this chapter presents the results of the crystal microstructure visualization and simulation of X-ray diffraction patterns of ZnO. The results of the crystal microstructure visualization for variations in composition and the shape of the X-ray diffraction pattern can be seen as follows Figure 2, 3, and 4.

Based on Figure 2, 3, and 4 above, the first column displays the visualization of the shape of the atomic structure that makes up a unit cell. The second column is a comparison of the diffraction pattern from the simulation with the JCPDS standard pattern from each crystal structure. The diffraction pattern shows that the peaks from the simulation match the peaks from the reference data in the JCPDS standard.

The nanorod structure has a monoclinic crystal system (a≠b≠c) with a space group C 2/c and lattice parameters a= 15.4170 Å b= 25.3560 Å c= 14.3840 Å producing maximum peak intensity with three highest peaks at I(020) > I(11-1) > I(200). The nanowire structure has a triclinic crystal system (a≠b≠c) with lattice parameters a= 12.0380 b= 2.4910 Å c= 16.8890 Å and a P-1 space group as in the picture which has 3 primary symbols and is the simplest form of symmetric lattice that produces maximum peak intensity with three highest peaks, namely I(001) > I(010) > I(001). The nanoflower structure has an orthorhombic crystal system (a≠b≠c) with lattice parameters a= 9.47310 Å b= 13.52960 Å c= 29.0220 Å and space group P b c a as shown in the figure which is included in the simplest symmetry lattice and produces maximum peak intensity with three highest peaks, namely I(004) > I (020) > I(112). Comparison of simulation lattice parameter prices with references can be seen in Table 2.

The positions of all diffraction peaks obtained from the simulation results are in accordance with the reference data for all structures that have been visualized. Each structure provides a different diffraction pattern according to the arrangement of atoms in the unit cell, spatial symmetry and field strengthening of each. This is in accordance with the theory of interaction and scattering of X-rays in crystals which states that the intensity of X-rays scattered by a crystal is determined

by the position of the atoms in the unit cell and the field strengthening (hkl) of the X-ray reflection, where each atom provides different electron scattering for each plane. Based on the data obtained with the reference, the visualization of a crystal structure can be tested for accuracy using this software so that it can be used to interpret XRD data correctly.

Table 2. Comparison of simulation lattice parameter prices with references.

Senyawa	Struktur	Parameter kisi	
		Referensi	Simulasi
Nanorod	Monoclinic *C 2/c*	a = 25.3330 Å b = 6.29900 Å c = 15.1610 Å	a = 15.4170 Å b = 25.3560 Å c = 14.3840 Å
Nanowire	Triclinic *P-1*	a = 18.9915 Å b = 18.9915 Å c = 12.5935 Å	a = 12.0380 Å b = 12.4910 Å c = 16.8890 Å
Nanoflower	Orthorhombic *P b c a*	a = 9.74700 Å b = 9.75100 Å c = 7.68900 Å	a = 9.47310 Å b = 13.5296 Å c = 29.0220 Å

CONCLUSION

In the variation of structure and microstructure, the position of the diffraction peak gives a different picture for each type of structure depending on the arrangement of atoms in the unit cell, where each crystal structure has a different position and spatial symmetry resulting in different diffraction patterns. The difference in the data value of the angle 2θ from the simulation results with the reference data is 0%, then the difference in the data value of the intensity of the simulation results with the reference is 8.87%.

Analysis of the simulation results in the form of crystal lattice parameters, structural shapes and diffraction peak positions shows that in the variation of structure and microstructure, the position of the diffraction peak gives a different picture for each type of structure depending on the arrangement of atoms in the unit cell, where each crystal structure has a different position and spatial symmetry resulting in different diffraction patterns. In the variation of composition, the ZnO compound has a hexagonal structure and its structure tends to change to monoclinic when added with S doping and its structure changes again to orthorhombic when doped with Se.

REFERENCES

1. Thema, F. T., Manikandan, E., Dhlamini, M. S., & Maaza, M. J. M. L. (2015). Green synthesis of ZnO nanoparticles via *Agathosma betulina* natural extract. *Materials Letters*, **161**, 124–127.
2. Surdia, T. & Saito, S. (2005). Pengetahuan bahan teknik. Jakarta: PT. Pradnya Paramita.
3. Rietveld, H. M. (1969). A profile refinement method for nuclear and magnetic structures. *Applied Crystallography*, **2**(2), 65–71.
4. Suminta, S. (2003). Simulasi pola difraksi sinar-X berbagai jenis mineral zeolit alam dengan program RIETAN. *Jurnal of Indonesia Zeolites*, **2**(1), 46–48.
5. Restiana, S. & Rini, A. S. (2018). Visualisasi struktur kristal keramik perovskite menggunakan VESTA. *Indonesian Physics Communication*, **15**(1), 46–50.
6. Abbas, A. M., Hammad, S. A., Sallam, H., Mahfouz, L., Ahmed, M. K., Abboudy, S. M., Ahmed, A. E., Alhag, S. K., Taher, M. A., Alrumman, S. A., Alshehri, M. A., Soliman, W. S., Abbasi, T., & Mostafa, M. (2021). Biosynthesis of zinc oxide nanoparticles using leaf extract of Prosopis juliflora as potential photocatalyst for the

treatment of paper mill effluent. *Applied Sciences*, **11**(23), 11394.
7. Wojnarowicz, J., Chudoba, T., & Lojkowski, W. (2020). A review of microwave synthesis of zinc oxide nanomaterials: Reactants, process parameters and morphologies. *Nanomaterials*, **10**(6), 1086.
8. Kittel, C. (1986). Introduction to Solid State 7th ed. New York: John Willey and Sons Inc.
9. Alfarisa, S., Rifai, D. A., & Toruan, P. L. (2018). Studi difraksi sinar-x struktur nano seng oksida (ZnO). *Risalah Fisika*, **2**(2).
10. O'Connor, B. H., & Pratapa, S. (2002). Improving the accuracy of Rietveld-derived lattice parameters by an order of magnitude. *Adv X-Ray Anal*, *45*, 158-165.
11. Momma, K., & Izumi, F. (2011). VESTA 3 for three-dimensional visualization of crystal, volumetric and morphology data. *Applied Crystallography*, **44**(6), 1272.

IPC

Indonesian Physics Communication

Department of Physics, Universitas Riau, Pekanbaru, Indonesia
p-ISSN 1412-2960 | e-ISSN 2579-521X

Vol. 22 | No. 1
March 2025

Web: https://kfi.ejournal.unri.ac.id
E-mail: kfi@ejournal.unri.ac.id

Modification of magnetic properties and morphology of iron oxide particles of natural sand from Rokan River through copper doping and preparation using ball milling method

Elika Gultom, Salomo Sinuraya*, Erwin Amiruddin, Awitdrus
Department of Physics, Universitas Riau, Pekanbaru 28293, Indonesia

*Corresponding author: salomo@lecturer.unri.ac.id

ABSTRACT

The magnetic susceptibility, magnetic properties, morphological properties, and composition of iron oxide nanoparticles of the natural sand in Rokan River, Rokan Hulu Regency, doped copper and prepared by the ball milling method. Processing of the magnetic and non-magnetic particle separation was carried out using iron sand separator (ISS). The ball milling process is ground in two stages for 70 hours and 30 hours and is divided into 3 parts and doped copper with concentrations (weight%) 0 wt%, 5 wt%, and 10 wt%, called BM_{2A}, BM_{2B}, and BM_{2C} products. The calculation of the magnetic susceptibility of the sample is carried out based on the values (B_T) and (B_0). The resulting magnetic susceptibility decreases as the percentage of copper doping increases. Vibrating sample magnetometer (VSM) shows the magnetic properties of iron oxide particles produced, namely magnetization saturation (M_S) decreases, coercivity value (H_C) and loop squareness (M_r/M_S) grow up, and remanent magnetization (M_r) and loop area (A) varies as doping concentration increases. Morphological properties and composition of iron oxide particles using a scanning electron microscope with energy dispersive X-ray (SEM-EDX). The average measurement of particles produced decreased with the increase in copper doping given, that is 121.960 ± 47.493 nm, 119.730 ± 37.03 nm, and 84.244 ± 34.392 nm. Copper element increased with the increase in doping concentrations given which were 0.76%, 7.11%, and 8.13%, while elements O, Si, and Fe decreased.

Keywords: Ball milling; copper; iron oxide; natural sand; Rokan River

Received 01-05-2023 | Revised 18-12-2024 | Accepted 15-03-2025 | Published 31-03-2025

INTRODUCTION

One of the mining products that are widely discovered in Indonesia is iron sand. Iron sand is often found in coastal areas or rivers, particularly in Java, Sumatra, Sulawesi and Nusa Tenggara [1, 2].

The utilization of iron sand in Indonesia can be said to have not been processed optimally. So far, iron sand has only been used as a building material and is generally exported in raw form [3-5]. In fact, the existence of iron sand that is easy to find can make it easier to process and make it into a material that has a high selling value [1]. The mineral content in iron sand depends on its local source, namely magnetite (Fe_3O_4), hematite (α-Fe_2O_3), maghemite (γ-Fe_2O_3) [1, 6, 7]. Iron sand has very broad applications and can be said to be the center of attention for researchers, where it has applications in industry, electronics, computing, and household equipment [8-10].

The size of iron oxide particles can be reduced to a nanometer scale using the ball milling method. Ball milling is a tool or machine that is useful for managing materials made of metal and has characteristics that are hard, not easily broken and corrosion resistant [11, 12]. This ball milling process is a powder crushing process carried out by a collision mechanism between steel balls and samples in order to produce finer particles up to nanometer size. Factors that affect ball milling performance include rotation speed, tube shape, time, temperature, pressure, and powder weight composition [13-15].

Preparation of iron oxide nanoparticles from natural sand from the Rokan River was carried

out using the ball milling method. The characterization test of the vibrating sample magnetometer (VSM) and scanning electron microscope with energy dispersive X-ray (SEM-EDX) was carried out by providing copper (Cu) doping to the sample in order to see changes in the magnetic properties and morphology of iron oxide particles.

RESEARCH METHODS

Natural sand from Rokan River, Ujung Batu, Riau Province, Indonesia is the sample used in this study. The separation process between magnetic and non-magnetic particles was carried out with the help of an iron sand separator (ISS) tool, referred to as the B_{ISS} product. The B_{ISS} product was then milled in the first stage of ball milling for 70 hours by mixing 16 iron balls with a diameter of 2 cm with the sample into a tube at a speed of 100 rpm, referred to as the BM_1 product. The BM_1 product was then milled in the second stage of ball milling for 30 hours and doped with copper elements with concentrations (weight%) of 0 wt%, 5 wt% and 10 wt%, referred to as the BM_{2A}, BM_{2B}, and BM_{2C} products. The magnetic susceptibility values of the samples, BISS products, BM_1, BM_{2A}, BM_{2B}, and BM_2 were calculated and the changes in magnetic properties in the samples were determined using a VSM and the morphological properties and composition of the samples were determined using a SEM-EDX.

RESULTS AND DISCUSSION

Magnetic Induction Measurement Data of Coreless Solenoid (B_0)

Table 1 and the graph in Figure 1 show the magnetic induction measurement data of the coreless solenoid (B_0).

The graph in Figure 1 explains that the magnetic induction value produced increases with the increase in the electric current given. The lowest magnetic induction value at a current of 200 mA is 3.398 mT and the highest induction value at a current of 1000 mA is 11.626 mT.

Table 1. B_0 measurement results.

Current (mA)	B_0 (mT)
200	3.398
400	5.508
600	7.584
800	9.601
1000	11.626

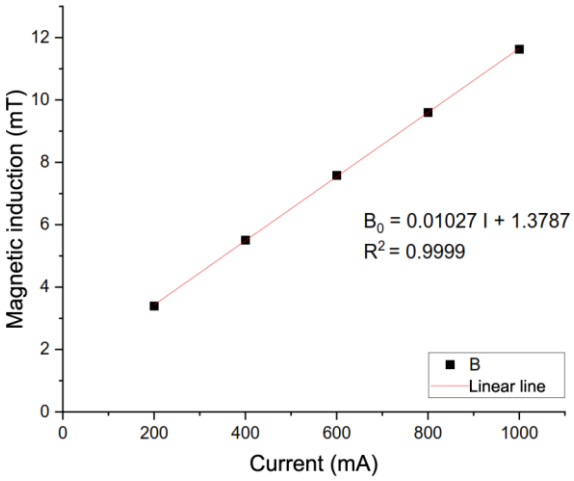

Figure 1. B_0 magnetic induction data graph.

Based on the linear equation obtained B_0 = 0.0103 I + 1.3787, R^2 = 0.9999, it shows that when the given current is eliminated I = 0 mA, the magnetic induction value produced is not immediately zero but B_0 is 1.3787 mT. This is due to the influence of the remaining energy and the earth's magnetic field on the solenoid. The R2 value has an interval of 0 – 1, when the value approaches 1, the resulting data is more accurate.

Solenoid Magnetic Induction Measurement Data with Natural Sand Sample Core (B_S)

Table 2 and the graph in Figure 2 show the solenoid magnetic induction measurement data with a natural sand sample core (B_S).

Table 2. B_S measurement results.

Current (mA)	B_0 (mT)
200	3.510
400	5.634
600	7.697
800	9.729
1000	11.931

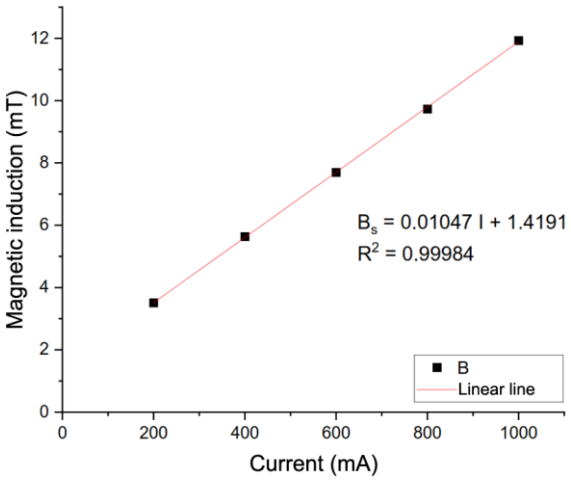

Figure 2. B_S magnetic induction data graph.

The graph in Figure 2 explains that the magnetic induction value produced increases with the increase in the electric current given. The lowest magnetic induction value at a current of 200 mA is 3.510 mT and the highest induction value at a current of 1000 mA is 11.931 mT.

Solenoid Magnetic Induction Measurement Data with ISS Product Sample Core (B_{ISS})

Table 3. B_{ISS} measurement results.

Current (mA)	B_0 (mT)
200	3.846
400	5.944
600	7.948
800	10.026
1000	12.204

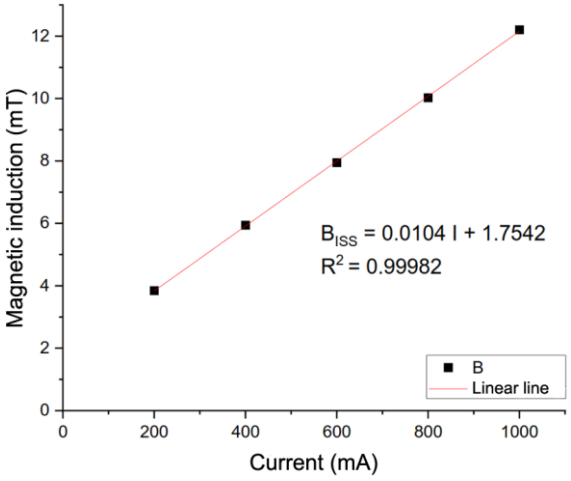

Figure 3. BISS magnetic induction data graph.

Table 3 and the graph in Figure 3 show the solenoid magnetic induction measurement data with an ISS product sample core (B_{ISS}). The graph in Figure 3 explains that the magnetic induction value produced increases with the increase in the electric current given. Based on Table 3. it can be seen that the magnetic induction value produced by the ISS product is greater than the magnetic induction value of the sample. This is because the ISS product has gone through a process of separating magnetic and non-magnetic particles, leaving more magnetic particles in it.

Solenoid Magnetic Induction Measurement Data with Multiple Product Sample Cores

The graphs in Figures 4, 5, 6, and 7 show the magnetic induction measurement data of the solenoid with the cores of the products BM_1, BM_{2A}, BM_{2B}, and BM_{2C}.

Figure 4 shows the graph of the magnetic induction value of the BM_1 product which is the first stage ball milling product for 70 hours using 16 iron balls with a diameter of 2 cm.

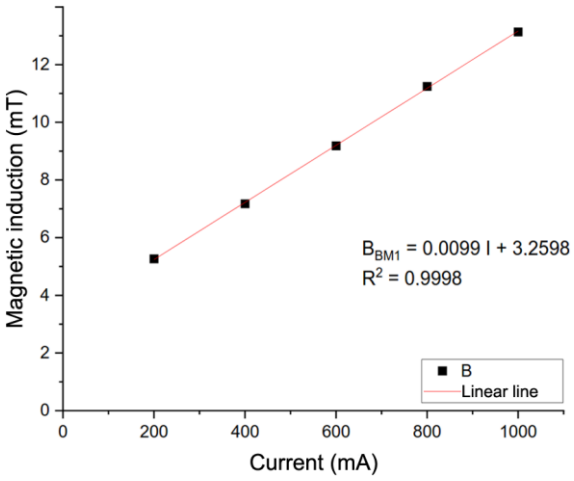

Figure 4. BM_1 magnetic induction data graph.

Figures 5, 6, and 7 show the magnetic induction graphs of the BM_{2A}, BM_{2B}, and BM_{2C} products which are the second stage ball milling products for 70 hours + 30 hours with 16 iron balls with a diameter of 2 cm and doped with copper elements with concentrations (weight%) of 0 wt%, 5 wt%, and 10 wt%. The magnetic induction values produced by the BM_{2A}, BM_{2B}, and BM_{2C} products are higher than the BM_1 product. This is due to the influence of the long

time of the ball milling process which results in a reduction in particle size that is getting smaller, thus increasing the number of iron oxide particles contained.

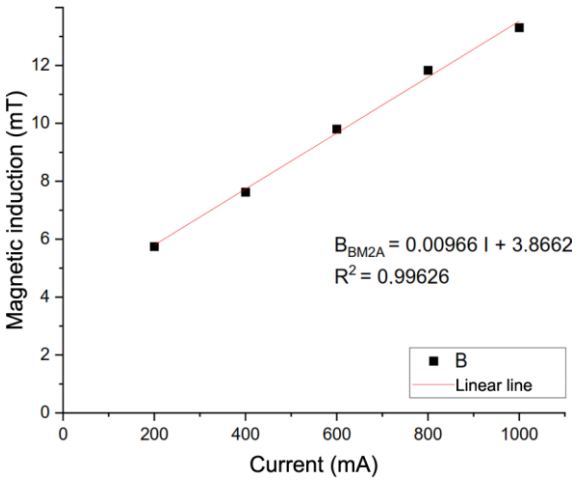

Figure 5. BM_{2A} magnetic induction data graph.

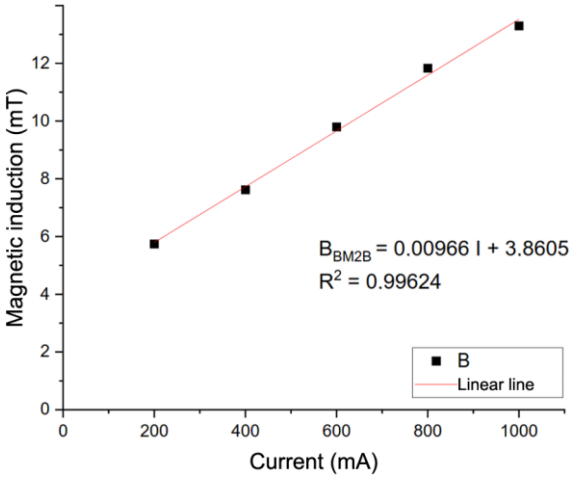

Figure 6. BM_{2B} magnetic induction data graph.

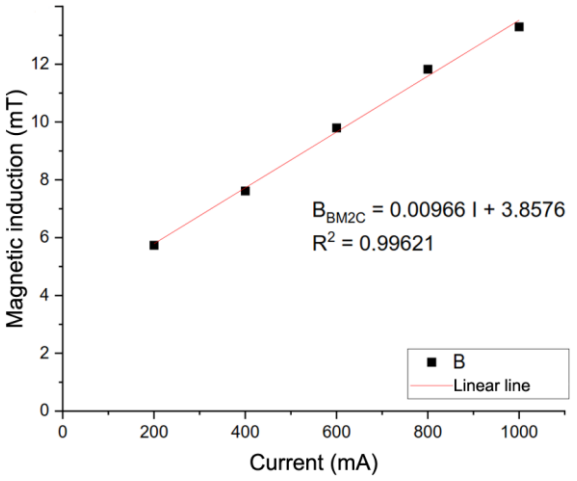

Figure 7. BM_{2C} magnetic induction data graph.

Magnetic Susceptibility Calculation Results (χ_m)

Table 4. Magnetic susceptibility data at a current of 1000 mA.

Sample	B_0 (mT)	B_T (mT)	χ_m (10^{-5})
Natural sand	11.626	11.931	2623.43
B_{ISS}	11.626	12.204	4791.61
BM_1	11.626	13.135	12979.52
BM_{2A}	11.626	13.305	14441.76
BM_{2B}	11.626	13.300	14398.76
BM_{2C}	11.626	13.296	14364.35

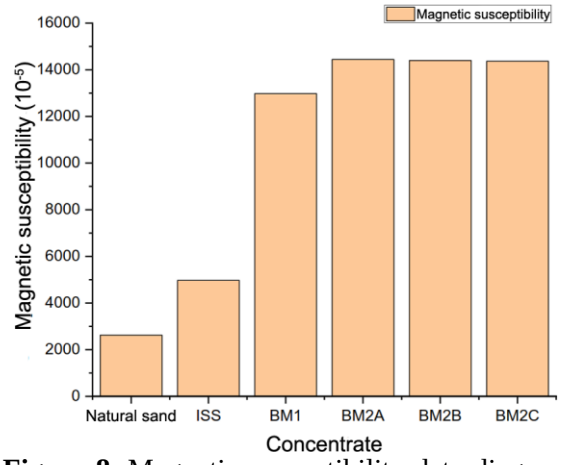

Figure 8. Magnetic susceptibility data diagram at a current of 1000 mA.

The results of the calculation of magnetic susceptibility data with a constant electric current of 1000 mA with a constant distance of 1 mm, on natural sand, ISS products, BM_1 products, BM_{2A} products, BM_{2B}, and BM_{2C} can be seen in Table 4 and the graph in Figure 8.

The data in Table 4. shows that the magnetic susceptibility value in natural sand samples has increased in the ISS product, this is because the ISS product has gone through a separation process between magnetic and non-magnetic particles so that more magnetic particles remain in it which causes the magnetic susceptibility value to be higher. The decrease in magnetic susceptibility value occurs in BM2A, BM2B, and BM2C products along with the increasing copper (Cu) doping given, because copper is a diamagnetic material that does not have a magnetic moment or its magnetism is weak, which causes the resulting susceptibility value to decrease along with increasing copper doping.

Scanning Electron Macroscope with Energy Dispersive X-Ray (SEM-EDX) Data

SEM characterization test was conducted to determine the changes in morphological properties found in BM_{2A}, BM_{2B}, and BM_{2C} products with a magnification of 5000 times as in Figure 9.

The SEM test results of BM2A, BM2B, BM2C products, namely the shape of the particles that vary and by using ImageJ software, the average size of the particles produced can be seen in Table 5. Basically, the shape of the hematite sample is or others. The results show that the magnetic nanoparticles produced are predominantly round, however, there are some magnetic nanoparticles produced that have irregular and asymmetric shapes. This is due to the ineffectiveness of destroying samples of the same size in ball milling process.

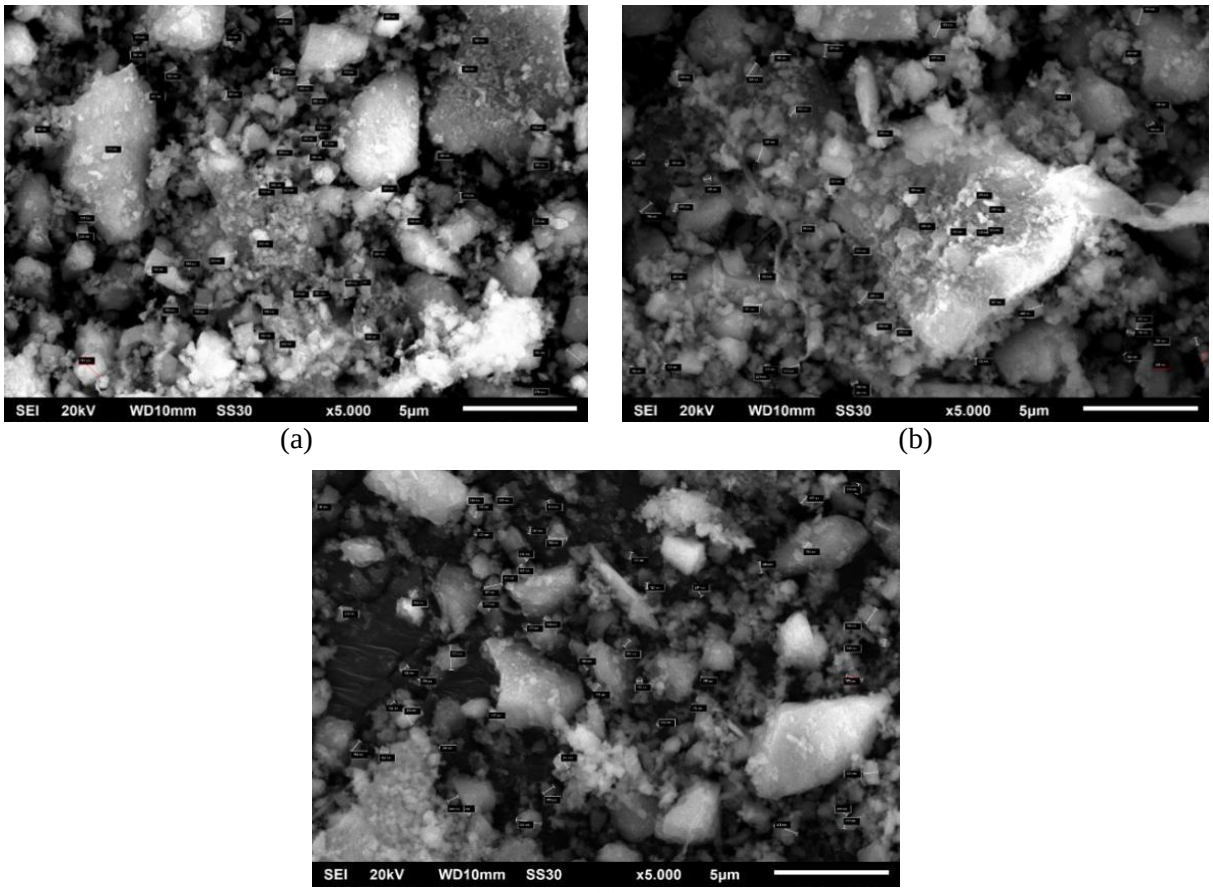

(a) (b)

(c)

Figure 9. Particle size of ball milling products at 5000 times magnification with copper doping (a) 0 wt%, (b) 5 wt%, and (c) 10 wt%.

Table 5. Average size of iron oxide particles.

Sample	Average size (nm)	Standard deviation
BM_{2A}	121.960	± 47.493
BM_{2B}	119.730	± 37.03
BM_{2C}	84.244	± 34.392

The EDX characterization test was carried out with the aim of determining changes in the elemental composition contained in the BM_{2A}, BM_{2B}, and BM_{2C} products as in Table 5.

The elements Fe and Si decreased as seen in Table 6. Along with the increase in copper doping given to BM_{2A}, BM_{2B}, and BM_{2C} products. This is because copper is a diamagnetic material that does not have a magnetic moment and its magnetism is weak, while Fe is a ferromagnetic that is strongly attracted by a magnet causing Fe to decrease, due to the influence of copper. Si decreased due to the influence of the length of the ball milling

process carried out which caused Si, which is a non-magnetic particle, to be removed from it.

Vibrating Sample Magnetometer Data

The results of the VSM characterization test were carried out to determine changes in the magnetic properties of the BM2A, BM2B, and BM2C products as shown in Figure 10 and Table 7.

The resulting magnetic properties are decreasing saturation magnetization (M_S), remanent magnetization (M_r) with a wide loop (A) that varies with increasing doping given to the BM_{2A}, BM_{2B}, and BM_{2C} products. Coercivity (H_c) and Loop squareness (M_r/M_S) increased.

Table 6. Elemental content in BM_{2A}, BM_{2B}, and BM_{2C} products.

Element	Mass (%)		
	BM_{2A}	BM_{2B}	BM_{2C}
C	17.52	18.40	47.6
O	23.88	18.98	13.03
Na	1.43	1.71	0.78
Mg	1.02	1.16	0.51
Al	5.26	5.48	2.36
Si	25.32	22.78	7.87
K	0.99	2.20	0.44
Ca	1.22	1.45	0.66
Ti	0.38	0.40	0.18
Fe	22.22	19.08	18.01
Cu	0.76	7.11	8.13
Zr	0.00	1.25	0.00
Zn	0.00	0.00	0.43
Total	100.00	100.00	100.00

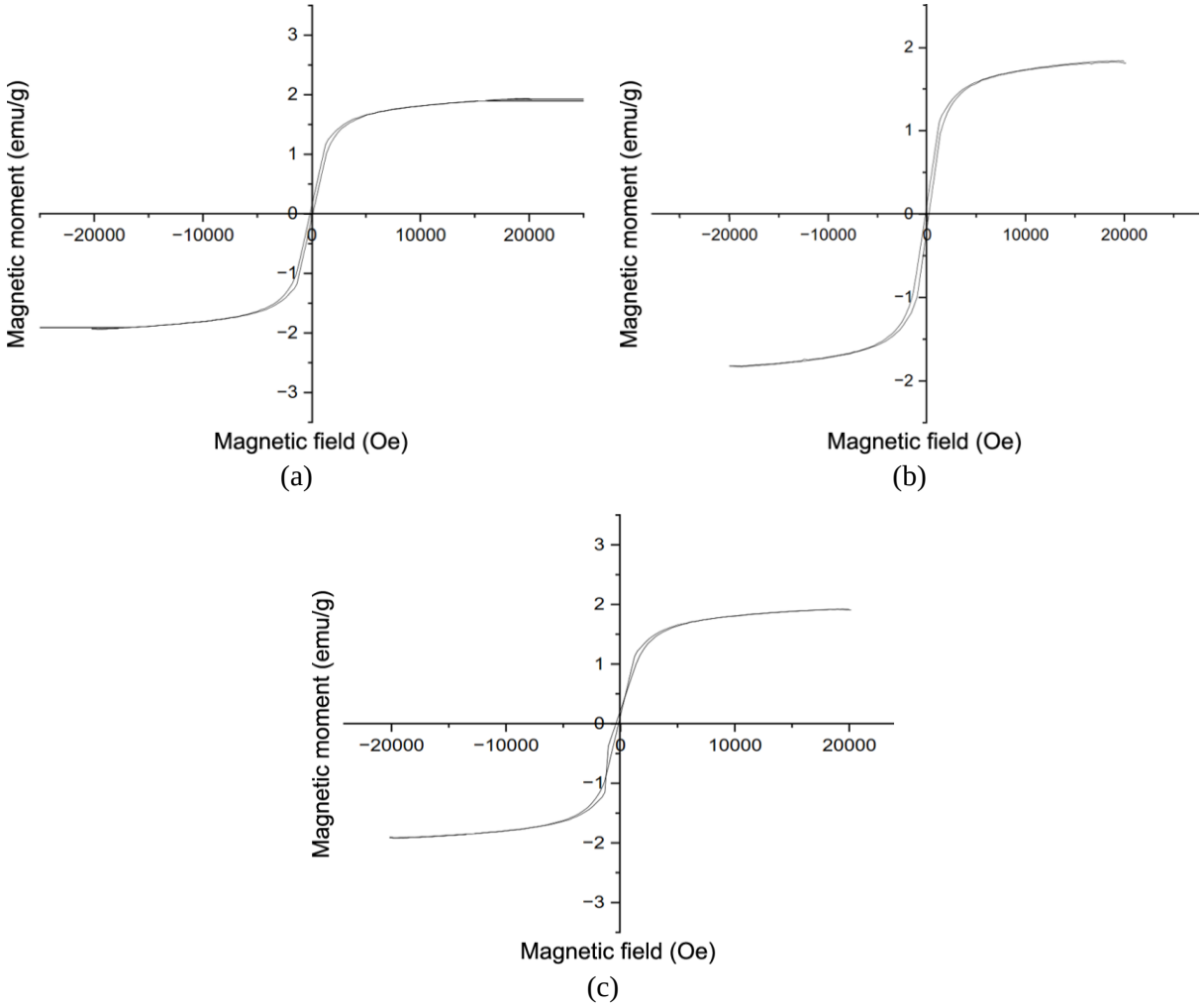

Figure 10. Hysteresis loop curve of the results of the ball milling characterization twith copper doping (a) 0 wt%, (b) 5 wt%, and (c) 10 wt%.

Table 7. Magnetic properties of the VSM characterization test results.

Parameter loop	BM_{2A}	BM_{2B}	BM_{2C}
M_S (emu/g)	1.904	1.817	1.804
M_r (emu/g)	0.1051	0.048	0.1432
H_C (Oe)	126.53	178.39	275.47
Loop squareness	0.055	0.066	0.079
Loop area (kOe.emu/g)	121.9	114.4	128.8

CONCLUSION

The results of this study can be concluded that the magnetic susceptibility value of α-Fe_2O_3 nanoparticles decreased, namely 14441.76×10^{-5}; 14398.76×10^{-5}; and 14364.35×10^{-5} along with the increase in copper doping (wt%) with values in the iron oxide interval. Changes in magnetic properties obtained through VSM are the saturation magnetization value (M_S) which decreased, the coercivity value (H_c) and loop squarness (M_r/M_S) obtained increased with the increase in copper doping given, while the remanent magnetization value (M_r) and the area of the hysteresis loop obtained varied. The results of SEM characterization show the size. The size of the iron oxide particles produced is getting smaller with the increase in copper doping (wt%) given. The copper element increases with the increase in doping concentration (wt%) given, namely 0.76%; 7.11%; and 8.13%. While the Fe element decreased along with the increasing doping concentration given, namely 22.22%; 19.08%; and 18.01%.

REFERENCES

1. Didik, L. A. & Wahyudi, M. (2020). Analisa kandungan Fe dan karakteristik sifat listrik pasir besi Pantai Telindung yang disintesis dengan beberapa metode. *Indonesian Physical Review*, **3**(2), 64–71.
2. Satria, B., Masrurah, Z., & Fajar, S. J. (2021). Magnetic susceptibility and grain size distribution as prospective tools for selective exploration and provenance study of iron sand deposits: A case study from Aceh, Indonesia. *Heliyon*, **7**(12).
3. Nengsih, S. (2018). Potensi nanopartikel magnetit pasir besi Lampanah Aceh Besar melalui studi kajian teknik pengolahan, sintesis dan karakteristik struktur. *CIRCUIT: Jurnal Ilmiah Pendidikan Teknik Elektro*, **2**(1).
4. Yudhawardana, H., & Lalus, H. F. (2023). Analysis of Chemical Compound Content and Magnetic Properties of Iron Sand in Rondo Woing Village, East Manggarai. *Jurnal Pendidikan Fisika Dan Teknologi*, **9**(1), 133–142.
5. Gani, A., Munawar, E., Mamat, R., & Rosdi, S. M. (2023). Investigation of the potential biomass waste source for biocoke production in Indonesia: A review. *Energy Reports*, **10**, 2417s–2438.
6. Royka, A. & Amiruddin, E. (2021). Penentuan nilai suseptibilitas dan ukuran partikel magnetik pasir alam Logas Kabupaten Kuantan Singingi menggunakan variasi ukuran ball milling. *Komunikasi Fisika Indonesia*, **18**(1), 42-47.
7. Widodo, R. D., Anis, S., Ilham, R. I., Firmansyah, H. N., & Wahyuni, N. (2021, March). Shrinkage, Density and Hardness of Hard Magnetic Material (BaFe12O19) Based on Iron Sand Produced by Conventional Solid-State Reaction Process. *IOP Conference Series: Earth and Environmental Science*, **700**(1), 012001.
8. Amiruddin, E., Awaluddin, A., Sihombing, M., Royka, A., & Syahrul, T. (2020). Morphology and structural properties of undoped and cobalt doped magnetic iron oxide particles for improving the environmental quality. *International Journal of Engineering and Advanced Technology (IJEAT)*, **9**(6), 2249–8958.
9. Jia, C., Das, P., Kim, I., Yoon, Y. J., Tay, C. Y., & Lee, J. M. (2022). Applications, treatments, and reuse of plastics from electrical and electronic equipment.

Journal of Industrial and Engineering Chemistry, **110**, 84–99.
10. Cenci, M. P., Scarazzato, T., Munchen, D. D., Dartora, P. C., Veit, H. M., Bernardes, A. M., & Dias, P. R. (2022). Eco-friendly electronics—A comprehensive review. Advanced Materials Technologies, **7**(2), 2001263.
11. Sari, M. N. (2018). *Analisa potensi pemanfaatan limbah pelepah kelapa sawit sebagai bahan dasar elektroda superkapasitor pada industri menengah masyarakat*. Doctoral dissertation, Universitas Islam Negeri Sultan Syarif Kasim Riau.
12. Wei, L. K., Abd Rahim, S. Z., Al Bakri Abdullah, M. M., Yin, A. T. M., Ghazali, M. F., Omar, M. F., Nemeș, O., Sandu, A. V., Vizureanu, P., & Abdellah, A. E. H. (2023). Producing metal powder from machining chips using ball milling process: A review. *Materials*, **16**(13), 4635.
13. Qiram, I. & Rubiono, G. (2021). Pengaruh Penambahan profil pada dinding silinder ball-Mill terhadap distribusi massa serbuk batu bata. *V-MAC (Virtual of Mechanical Engineering Article)*, **6**(2), 52–56.
14. Sitotaw, Y. W., Habtu, N. G., Gebreyohannes, A. Y., Nunes, S. P., & Van Gerven, T. (2023). Ball milling as an important pretreatment technique in lignocellulose biorefineries: A review. *Biomass conversion and biorefinery*, **13**(17), 15593–15616.
15. Bangar, S. P., Singh, A., Ashogbon, A. O., & Bobade, H. (2023). Ball-milling: A sustainable and green approach for starch modification. *International Journal of Biological Macromolecules*, **237**, 124069.

IPC

Indonesian Physics Communication

Department of Physics, Universitas Riau, Pekanbaru, Indonesia
p-ISSN 1412-2960 | e-ISSN 2579-521X

Vol. 22 | No. 1
March 2025

Web: https://kfi.ejournal.unri.ac.id
E-mail: kfi@ejournal.unri.ac.id

The effect of variations in the size of milling balls on the magnetic properties and morphology of natural sand particles in the Rokan River

Dini Afriyunita, Salomo Sinuraya*, Erwin Amiruddin, Juandi Muhammad
Department of Physics, Universitas Riau, Pekanbaru 28293, Indonesia

*Corresponding author: salomo@lecturer.unri.ac.id

ABSTRACT

Magnetic susceptibility, magnetic properties and morphological properties of natural sand from the Rokan river based on variations in milling ball size. Natural sand samples were put into the iron sand separator for separation between magnetic and non-magnetic particles which were then carried out in a ball milling process for 80 hours using iron balls with a diameter of 1, 2, and 3 cm. The results of the ball milling were then separated using NdFeB magnets, these products are called BM I, BM II, and BM III products. The susceptibility values generated in this study increased with increasing milling ball sizes, for milling ball sizes of 1, 2, and 3 cm the magnetic susceptibility values were 12906.293×10^{-5}, 13390.387×10^{-5}, and 14816.736×10^{-5}. The results of the VSM test showed that the saturation magnetization obtained by the BM I, BM II, and BM III products was 2.89, 2.28, and 4.71 emu/g, the remanent magnetization values obtained by 0.45, 0.35, and 0.27 emu/g and the coercivity obtained was 249.07, 263.89, and 275.85 Oe. The results of the SEM-EDX identification showed that Fe increased from 16.24% to 22.68%, while in non-magnetic elements Si decreased from 24.49% to 18.76% with an average particle size getting smaller with increasing size milling ball.

Keywords: Ball milling; magnetic susceptibility; natural sand; NdFeB; Rokan River

Received 29-04-2023 | Revised 15-12-2024 | Accepted 08-03-2025 | Published 31-03-2025

INTRODUCTION

Indonesia is rich in natural resources containing natural minerals. However, many of these natural resources have not been processed and utilized optimally [1].

The use of iron ore in Indonesia is still limited to being used as an additional material in cement factories. Iron ore is generally exported in the form of raw materials, but because iron ore can be further processed and used more efficiently, the price becomes higher [2]. This iron sand has a characteristic black color and is found in abundance on beaches, rivers and mountains. Iron sand contains magnetic minerals consisting of magnetite (Fe_3O_4), hematite ($\propto$-Fe_2O_3) and maghemite (γ-Fe_2O_3), widely used in the magnet manufacturing industry. The minerals contained in iron sand have excellent electromagnetic properties, so they can be used in the biomedical field such as heavy metal adsorption and magnetic sensors [3-5].

The sample used was natural sand from the Rokan River, in Ujung Batu, Riau Province. Magnetic and non-magnetic particles in natural sand were separated using iron sand separator (ISS), and iron sand was refined using ball milling, its magnetic properties were determined using vibrating sample magnetometer (VSM), and its morphological properties were determined using scanning electron microscope using energy dispersive X-rays (SEM-EDX).

RESEARCH METHODS

The sample was natural sand from the Rokan River in Ujung Batu, Riau Province. The sample was inserted into the ISS to separate magnetic and non-magnetic particles, then ground using ball milling for 80 hours using variations in the size of iron balls, namely, 100 pieces of 1 cm iron balls, 48 pieces of 2 cm iron balls, and 16 pieces of 3 cm iron balls with a tube rotation speed of 100 rpm. Furthermore,

the magnetic susceptibility value of natural sand samples, ISS products, and ball milling products was determined. The magnetic properties of the ball milling products were tested using the VSM test and the morphological properties of the ball milling products were tested using the SEM-EDX test.

RESULTS AND DISCUSSION

Magnetic Induction Measurement

Measurement of the magnetic induction of a coreless solenoid as a function of current, the amount of current given is 200 mA, 400 mA, 600 mA, 800 mA, 1000 mA with a fixed distance from the Pasco probe magnet to the solenoid of 1 mm.

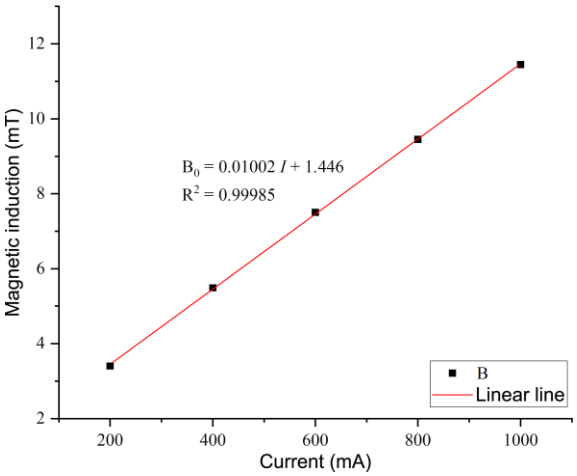

Figure 1. Graph of the magnetic induction of a coreless solenoid (B_0) as a function of current.

Figure 1 shows the magnetic induction value increases with increasing electric current given. The magnetic induction value at a current of 200 mA of 3.404 mT increases at a current of 1000 mA of 11.568 mA.

The B_0 value obtained is B_0 = 0.01002 I + 1.446 and R^2 = 0.99985 where R is the graph error value, if the R value approaches 1 then the graph can be said to be linear. The linear equation shows that when the electric current flow in the solenoid is stopped, the magnetic induction value of the solenoid is not immediately zero, but there is still a residual magnetic induction of 1.4466 mT. This happens because of the influence of the earth's magnetic field which is still stored in the solenoid.

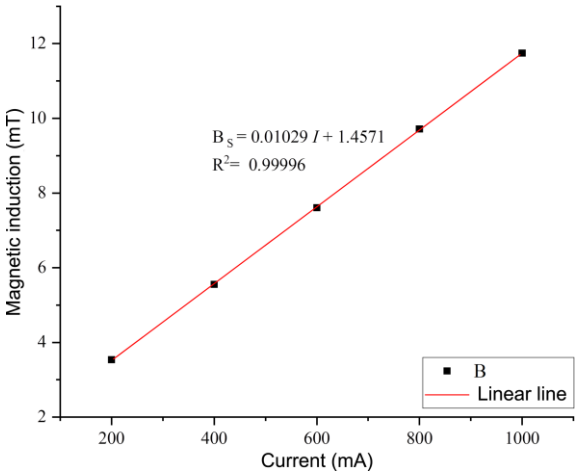

Figure 2. Magnetic induction graph of the solenoid with a natural sand core from the Rokan River (B_S) as a function of current.

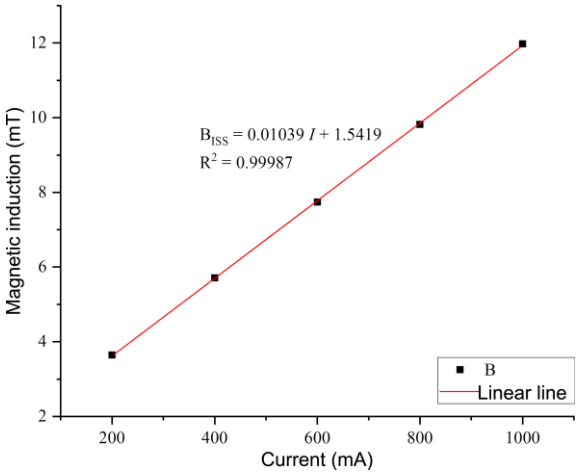

Figure 3. Magnetic induction graph of the ISS product sample (B_{ISS}) as a function of current.

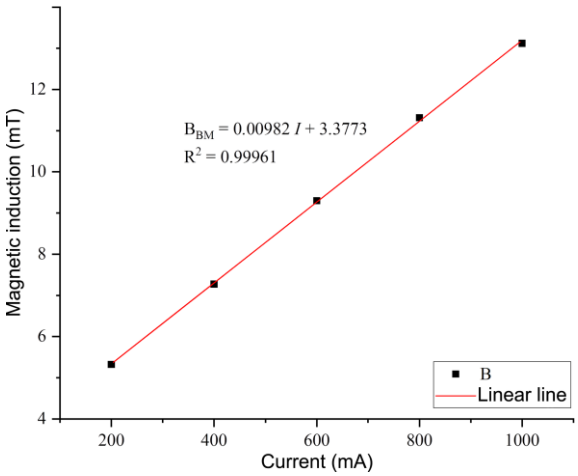

Figure 4. Magnetic induction graph of BM I product sample as a function of current.

The increase in the magnetic induction value for the ISS product sample contains more magnetic particles than the magnetic induction value of the natural sand sample. The increase in the induction value is due to the large number of non-magnetic particles that are separated from the iron sand particles during the separation process in the ISS. The magnetic induction value increases with the increase in the electric current given.

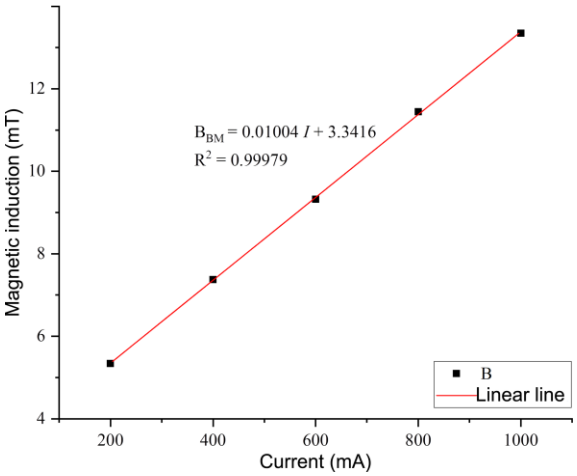

Figure 5. Magnetic induction graph of BM II product as a function of current.

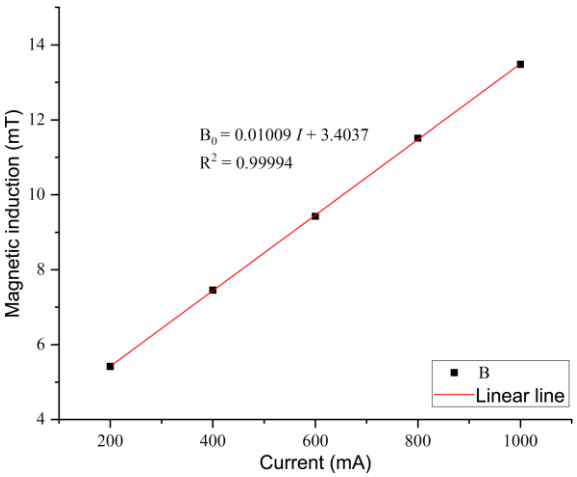

Figure 6. Magnetic induction graph of BM III product as a function of current.

The measurement of the magnetic induction of the solenoid of BM I, BM II, and BM III products shows a graph that increases linearly. The increase in this graph is influenced by the variation in the size of the milling ball where the iron ball used is 1, 2, and 3 cm. This is because the larger the ball used, the smaller the particles produced and the resulting induction value will increase.

Magnetic Susceptibility

Magnetic susceptibility is a quantity that describes the relationship between the magnetic susceptibility of a material and an external magnetic field (H). When an external magnetic field is applied, the magnetic moment is in the same direction as the external magnetic field, which is called magnetization (M).

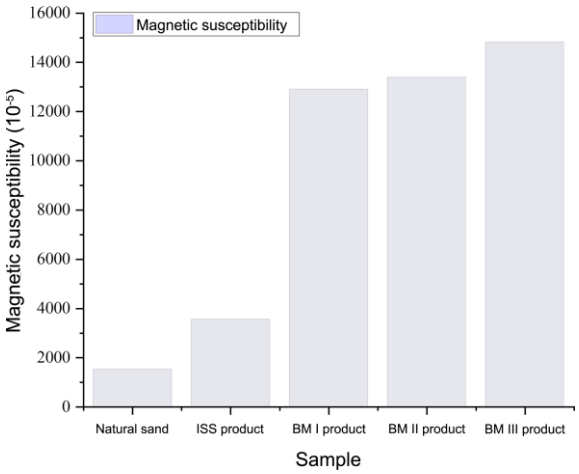

Figure 7. Graph of magnetic susceptibility values (χm) of natural sand, ISS products, BM I products, and BM II products, and BM III.

Figure 7 shows an increasing bar graph. The magnetic susceptibility value of the natural sand sample is 1521.439×10^{-5}, the ISS product is 3552.905×10^{-5}, the BM I product is 12906.293×10^{-5}, the BM II product is 13390.38×10^{-5} and the BM III product is 14816.736×10^{-5}.

Figure 7 shows the relationship between the size of the milling ball will affect the magnetic susceptibility value produced, where the larger the size of the ball used to smooth the particles, the greater the magnetic susceptibility value obtained. The resulting susceptibility value is directly proportional to the increasing size of the milling ball.

Magnetic Properties Using VSM

Magnetic properties testing using VSM produces saturation magnetization (M_S),

remanent magnetization (M_r), coercivity (H_c), loop square (M_r/M_S), and hysteresis loop area. Natural sand separated by ISS is smoothed for 80 hours in ball milling using iron balls with diameters of 1, 2, and 3 cm. Then testing is carried out using VSM and the VSM results are presented in the form of a hysteresis curve.

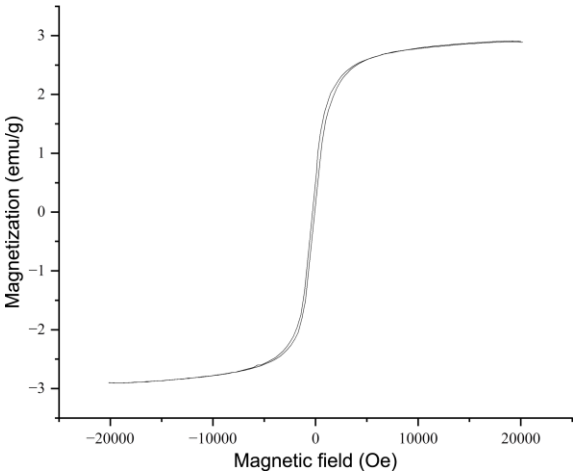

Figure 8. Hysteresis curve of BM I product.

Figure 8 shows the hysteresis curve obtained from magnetic properties testing using VSM of BM I product with a variation of 1 cm milling ball with a constant time of 80 hours. In the BM I product, the saturation magnetization value (M_S) was obtained at 2.89 emu/g, the remanent magnetization value (M_r) was 0.45 emu/g, the coercivity value (H_c) was 249.07 Oe, the loop squareness value (M_r/M_S) was 0.16 and the hysteresis loop area value (A) was 217.7 kOe. emu/g.

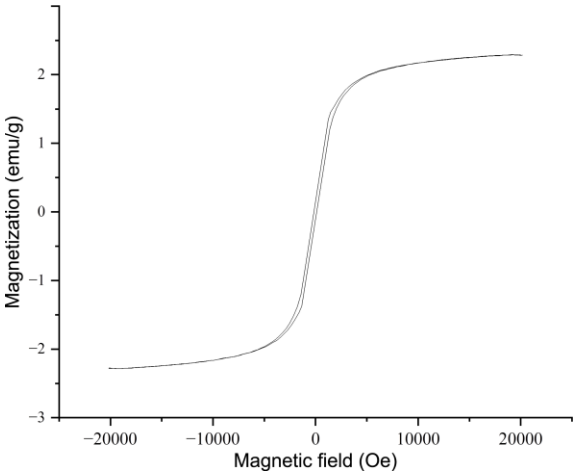

Figure 9. Hysteresis curve of BM II product.

Figure 9 shows that the BM II product obtained a saturation magnetization value (M_S) of 2.28 emu/g, the resulting remanent magnetization value (M_r) of 0.35 emu/g, the coercivity value (H_c) of the BM II product of 263.89 Oe, the loop squareness value (M_r/M_S) of 0.15 and the loop hysteresis area value (A) obtained of 195.9 kOe.emu/g.

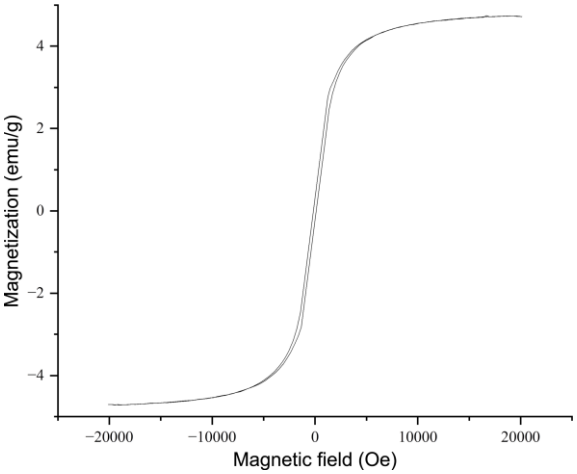

Figure 10. Hysteresis curve of BM III product.

Figure 10 shows that the BM III product obtained a saturation magnetization value (M_S) of 4.71 emu/g, the resulting remanent magnetization value (M_r) of 0.27 emu/g, coercivity value (H_c) of 275.85 Oe, loop squareness value (M_r/M_S) of 0.38 and hysteresis loop area value (A) obtained of 352.5 kOe.emu/g.

Based on the test results that have been obtained, the coercivity value of the 1 cm ball BM product is 249.07 Oe, the 2 cm ball BM product is 263.89 Oe, and the 3 cm ball BM product is 275.85 Oe. So the highest coercivity value (H_c) is owned by the 3 cm milling ball and the lowest coercivity value is on the 1 cm milling ball. This shows that the greater the coercivity value in a magnetic material, the more difficult it is to eliminate its magnetic properties.

Morphological Properties of Particles Using SEM-EDX

The results of the particle size test were used in SEM-EDX and ball milled for 80 hours with

variations in the size of the iron balls of 1, 2, and 3 cm with a magnification of 5000 times.

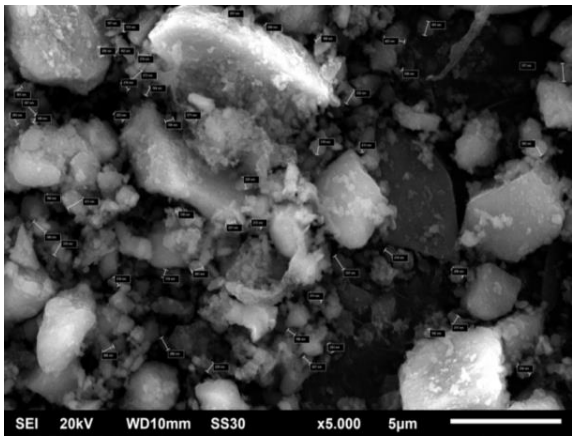

Figure 11. Particle size of BM I product with 5000 times magnification.

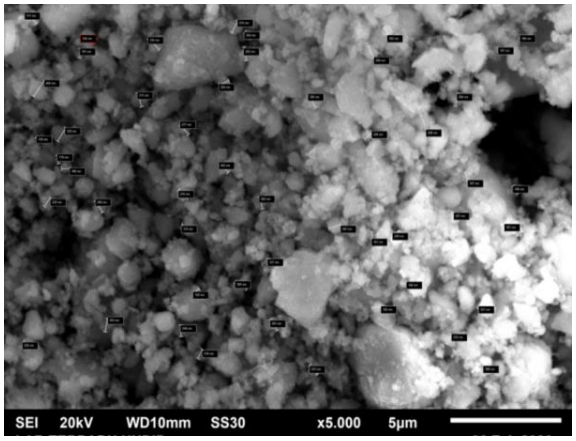

Figure 12. Particle size of BM II product with 5000 times magnification.

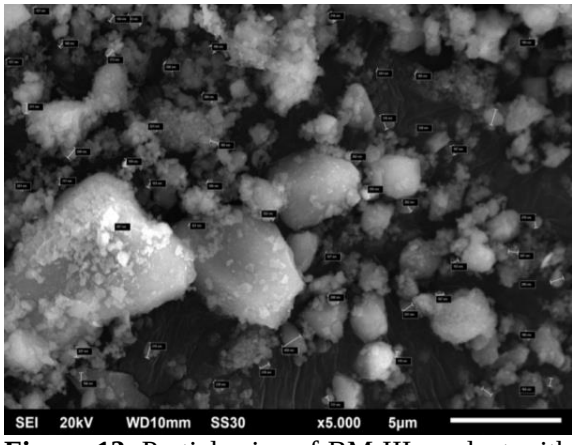

Figure 13. Particle size of BM III product with 5000 times magnification

The particle size of the natural sand sample from the Rokan River that had been ball milled for 80 hours using a 1 cm diameter iron ball was 378.18 ± 94.91 nm, on a 2 cm diameter iron ball it was 298.12 ± 86.67 nm and on a 3 cm diameter iron ball the particle size produced was 255.56 ± 68.25 nm. The results of particle size using a SEM-EDX showed that variations in the diameter of the milling ball used affected the particle size produced.

Table 1. Composition of BM I, II, and III products using SEM-EDX.

Element	Mass (%)		
	BM I	BM II	BM III
C	27.92	23.02	38.08
O	16.80	19.60	14.26
Na	1.13	1.71	0.67
Mg	1.18	1.55	0.45
Al	5.07	6.75	2.44
Si	24.49	20.59	18.76
K	0.89	1.45	0.93
Ca	2.11	2.13	0.58
Ti	1.80	0.58	0.25
Fe	16.24	21.56	22.68
Cu	1.65	1.06	0.90
Zn	0.72	0.00	0.00
Total	100.00	100.00	100.00

Table 1 shows the percentage composition contained in the natural sand samples of the Rokan River that have been ball milled for 80 hours with variations in the size of the iron balls of 1 cm, 2 cm, and 3 cm. There was an increase in the percentage of the magnetic element Fe in the BM I, BM II, and BM III products, respectively, namely 16.24%; 21.56%; 22.68%. In the composition of the non-magnetic element Si, there was a decrease in the percentage in the BM I, BM II, and BM III products, respectively, namely 24.49%; 20.59%; 18.76%. In the test of BM I, II, and III products using Scanning Electron Microscope with Electron Dispersive X-ray (SEM-EDX), it was shown that the ball milling product samples contained a lot of C, O, Fe and Si elements.

CONCLUSION

The magnetic susceptibility value increases with the increase in the electric current given in

proportion to the increase in the size of the iron ball used, the magnetic susceptibility value of the BM I product is 12906.293 × 10^{-5}, the BM II product is 13390.38 × 10^{-5}, and the BM III product is 14816.736 × 10^{-5}. The remanent magnetization value (M_r) decreases and the coercivity value (H_c) increases. While the saturation magnetization value (M_S), loop squerness (M_r/M_S) and the area of the hysteresis loop have varying values when the diameter of the ball increases. The variation in the diameter size of the milling ball used affects the size and composition of the particles, the larger the milling ball used, the smaller the particle size produced and the composition of the magnetic element Fe increases and the non-magnetic element Si decreases.

REFERENCES

1. Kunaifi, A. & Syah, A. F. (2023). Natural resource management in the perspective of fiqh rules: An Islamic State budget proposal for Indonesia. *Islamic Res.*, **6**(1).
2. Jégourel, Y. (2020). The global iron ore market: From cyclical developments to potential structural changes. *The Extractive Industries and Society*, **7**(3), 1128–1134.
3. Heryanto, H., Siswanto, S., Rahmat, R., Sulieman, A., Bradley, D. A., & Tahir, D. (2023). Nickel slag/laterite soil and nickel slag/iron sand nanocomposites: structural, optical, and electromagnetic absorption properties. *ACS omega*, **8**(21), 18591–18602.
4. Bhateria, R. & Singh, R. (2019). A review on nanotechnological application of magnetic iron oxides for heavy metal removal. *Journal of Water Process Engineering*, **31**, 100845.
5. Amiruddin, E., Awaluddin, A., Sihombing, M., Royka, A., & Syahrul, T. (2020). Morphology and structural properties of undoped and cobalt doped magnetic iron oxide particles for improving the environmental quality. *International Journal of Engineering and Advanced Technology (IJEAT)*, **9**(6), 2249–8958.

IPC

Indonesian Physics Communication

Department of Physics, Universitas Riau, Pekanbaru, Indonesia
p-ISSN 1412-2960 | e-ISSN 2579-521X

Vol. 22 | No. 1
March 2025

Web: https://kfi.ejournal.unri.ac.id
E-mail: kfi@ejournal.unri.ac.id

Making supercapacitor carbon electrodes from lemongrass leaf biomass with variations in physical activation temperature

Akmal Jaliaz, Awitdrus*
Department of Physics, Universitas Riau, Pekanbaru 28293, Indonesia

*Corresponding author: awitdrus@lecturer.unri.ac.id

ABSTRACT

Supercapacitor is energy storage device consisting of current collector, electrodes, separator, and electrolyte. Material selection and fabrication of the electrodes play an important role in improving the performance of the supercapacitor. In this research, carbon electrodes of supercapacitors were made from citronella leaves using variations in physical activation temperature. The preparation of carbon electrodes were starts from the pre-carbonization at temperature of 200℃ for 2 hours, chemical activation using 0.3 M KOH as activating agent, carbonization process using N_2 gas at temperature of 600℃ and physical activation using CO_2 gas with temperature variations of 750℃, 800℃, and 850℃. The highest of percentage density reduction at temperature 800℃ is 51.42%. Analysis using X-ray diffraction showed that the sample has a semicrystalline structure with the highest of ratio L_c/L_a and average number of microcrystalline layer (N_p) at temperature of 800℃, are 0.27 and 1.67 respectively. The highest of specific capacitance value is 122 F/g at temperature 800℃. The result show that the optimum physical activation temperature for carbon electrodes based on citronella leaves is 800℃.

Keywords: Carbon electrode; citronella leaves; physical activation; temperature; supercapacitor

Received 05-04-2023 | Revised 31-10-2024 | Accepted 09-03-2025 | Published 31-03-2025

INTRODUCTION

Technological developments have progressed over time, especially in energy storage systems. Current energy consumption still relies on natural gas, coal, and fossil fuels, which are non-renewable energy sources. Renewable energy such as water, wind, and solar have many shortcomings, including intermittent costs, regional nature, and inability to be widely applied [1]. Therefore, it is necessary to develop technology in the conversion and storage of alternative energy at this time [2].

The current energy storage device that is getting the attention of all countries, including Indonesia, is the li-ion battery. However, li-ion batteries have several disadvantages, including low power density, slow energy transfer processes, and long charging times [3]. Much research has been done to find alternative energy storage devices that can be used for a long time, are cost-effective, and easy to obtain, one of which is a supercapacitor. Supercapacitors have one of the main components, namely electrodes. The optimal capacitance value of a supercapacitor is influenced by the electrodes. The electrodes are in the form of activated carbon which can be produced from biomass that have gone through chemical and physical activation processes. Biomass usually comes from organic materials such as plants, animals, and industrial waste.

Biomass that has the potential to be used as a carbon electrode in supercapacitors is lemongrass waste. Lemongrass (*Cymbopogon nardus L.*) is a grass plant that has a leaf structure like thatch [4]. Lemongrass is widely found in Asia, especially Indonesia. Lemongrass waste that has passed the harvest period is usually used as animal feed and organic fertilizer [5].

Lemongrass leaves contain quite high lignocellulose, consisting of around 28.15% cellulose, 32.22% hemicellulose and 18.78% lignin [6]. This content makes lemongrass leaves have the potential to be used as carbon

electrodes in supercapacitor cells. This study focuses on the role of the influence of physical activation temperature on the density reduction and specific capacitance of the resulting supercapacitor cells.

RESEARCH METHODS

This research method explains the procedure for making carbon electrodes for supercapacitor cells made from citronella leaves. Citronella leaves are separated from the bones, then cut into 5 cm lengths and dried in the sun until constant mass. The pre-carbonization process uses an oven with a temperature of 200℃ for 2 hours and the sample is ground using ball milling for 24 hours with a rest period of 4 hours. The sample is sieved using a 53 μm sieve to standardize the particle size of the carbon powder. The chemical activation process uses 0.3 M KOH as an activating agent. The manufacture of pellets from carbon powder uses a hydraulic press with a pressure of 7.5 tons and is held for 2 minutes. The carbonization process is carried out by heating the pellets in a furnace at a temperature of 600℃ which is flowed with nitrogen gas (N_2). The physical activation process uses Carbon dioxide gas (CO_2) with temperature variations of 750℃, 800℃, and 850℃. The carbon electrode is soaked using distilled water until the pH is neutral. The manufacture of supercapacitor cells was carried out using several materials, namely carbon electrodes, current collectors, Teflon, separators (2nd layer of Softies surgical masks), and electrolytes (H_2SO_4) as much as 1 M. Each sample was subjected to density calculations and X-ray diffraction analysis, as well as electrochemical properties testing using the cyclic voltammetry method.

RESULTS AND DISCUSSION

Density Analysis

Figure 1 is a graph of the density reduction of carbon electrodes before and after the pyrolysis process. Density is related to the pores and surface area of the carbon electrode. Density reduction is caused by the evaporation of non-carbon compounds at the carbonization stage, the formation of new pores and opening old pores at the physical activation stage [2]. The density of each sample of SW-750, SW-800, and SW-850 after the carbonization-physical activation process is 0.702, 0.625, and 0.662 gr/cm^3 with a percentage of density reduction of 35.09%, 51.42%, and 42.29%, respectively. SW-800 has the lowest density compared to SW-750 and SW-850. A temperature of 800℃ is the optimum temperature for the formation of carbon pores in citronella leaf biomass. Density shrinkage is related to the porosity properties of the carbon electrode, because the lower the density, the carbon electrode will have high porosity. High porosity indicates that the carbon electrode has many pores and is able to improve the performance of the carbon electrode [7].

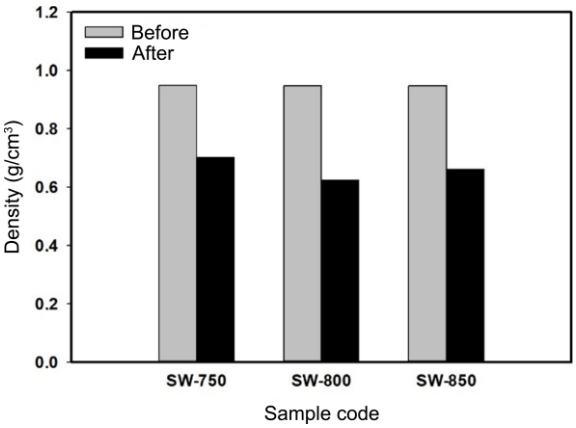

Figure 1. Graph of carbon electrode density shrinkage.

X-ray Diffraction Data Analysis

The resulting X-ray diffraction pattern is a typical activated carbon diffraction pattern, namely there are 2 gentle peaks in the diffraction angle range 2θ angle 24º – 25º with a reflection plane of 002 and an angle of 44º – 45º reflection plane 100. The two gentle peaks mark the scattering angles that correspond to the semicrystalline structure of carbon materials made from biomass [8].

The surface area of the carbon electrode is influenced by the values of L_a and L_c, the higher the L_c, the greater the surface area, because L_c is directly proportional and L_a is inversely proportional to the surface area [9]. In Table 1, the SW-800 sample has a higher Lc value of 6.10 nm and a lower La value of 22.46 nm compared to the SW-750 sample, therefore SW-800 has the highest L_c/L_a ratio and average layer (N_p) of 0.27 and 1.67.

Table 1. Interplane distance and microcrystalline dimensions of carbon electrode.

Sample code	2θ		Interplane distance		Microcrystalline dimensions		L_c/L_a	N_p
	002	100	d_{002} (°)	d_{100} (°)	L_c (nm)	L_a (nm)		
SW-750	23.26	44.98	3.82	2.01	5.16	30.37	0.17	1.35
SW-800	24.34	45.16	3.65	2.00	6.10	22.46	0.27	1.67

Cyclic Voltammetry Analysis

The cyclic voltammetry test curves of the SW-750, SW-800, and SW-850 samples with a scan rate of 1 mV/s are shown in Figure 2. The resulting CV curves have a curve and approach a rectangular shape, where this form is the ideal property of electrochemical double layer supercapacitors (EDLC) [10]. The CV curve on SW-750 has the smallest area and the CV curve on SW-800 has the largest area, this can affect the magnitude of the specific capacitance value in the supercapacitor cell. The wider the CV curve, the greater the charge-discharge current value, so the specific capacitance is high.

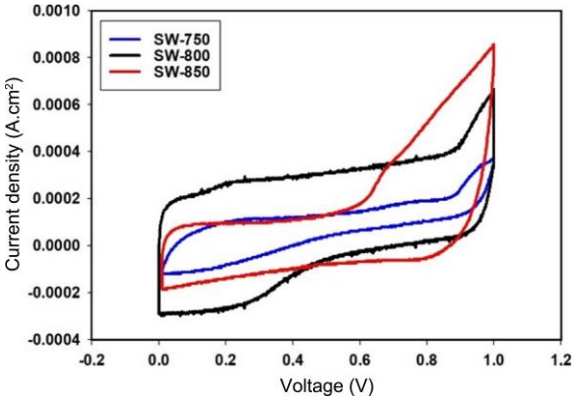

Figure 2. Cyclic voltammetry curve.

The specific capacitance values for each sample of SW-750, SW-800, and SW-850 are 29, 122, and 70 F/g. In the curve of each sample, there is a significant increase in current density. This increase in current density is due to the heteroatom content in the sample [11]. The high specific capacitance value in SW-800 is due to having the lowest density value after the pyrolysis process of the other samples. The low density value of the carbon electrode can increase porosity which indicates that there are many pores in the carbon electrode. Low physical activation temperature causes little formation of pores in the carbon electrode. While too high a physical activation temperature damages the pore structure of the carbon electrode [8, 12].

CONCLUSION

The results and discussion show that 800°C is the optimum physical activation temperature for lemongrass leaf samples. A temperature of 800°C can produce carbon electrodes with the highest density shrinkage percentage of 51.42%. The physical activation temperature of 800°C has high L_c, L_c/L_a, and N_p values so that it can increase the surface area of the carbon electrode. Analysis using cyclic voltammetry shows that a temperature of 800°C can produce a C_{sp} of 122 F/g.

REFERENCES

1. Wang, J., Zhang, X., Li, Z., Ma, Y., & Ma, L. (2020). Recent progress of biomass-derived carbon materials for supercapacitors. *J. Power Sources*, **451**, 227794.
2. Jiang, G., Senthil, R. A., Sun, Y., Kumar, T. R., & Pan, J. (2022). Recent progress on porous carbon and its derivatives from plants as advanced electrode materials for

supercapacitors. *J. Power Sources*, **520**, 230886.
3. Yu, Z., Tetard, L., Zhai, L., & Thomas, J. (2015). Supercapacitor electrode materials: nanostructures from 0 to 3 dimensions. *Energy Environ. Sci.*, **8**(3), 702–730.
4. Francisco, V., Figueirinha, A., Neves, B. M., García-Rodríguez, C., Lopes, M. C., Cruz, M. T., & Batista, M. T. (2011). Cymbopogon citratus as source of new and safe anti-inflammatory drugs: bio-guided assay using lipopolysaccharide - stimulated macrophages. *J. Ethnopharmacol.*, **133**(2), 818–827.
5. Gustiar, F., Munandar, M., Negara, Z. P., & Efriandi, E. (2020). Pemanfaatan limbah serai wangi sebagai pakan ternak dan pupuk organik di Desa Payakabung, Kabupaten Ogan Ilir, Sumatera Selatan. *Abdihaz: Jurnal Ilmiah Pengabdian pada Masyarakat*, **2**(1), 16–23.
6. Timung, R., Naik Deshavath, N., Goud, V. V., & Dasu, V. V. (2016). Effect of subsequent dilute acid and enzymatic hydrolysis on reducing sugar production from sugarcane bagasse and spent citronella biomass. *Journal of Energy*, **2016**(1), 8506214.
7. Zulkifli, Awitdrus, & Taer, E. (2018). Studi awal pemanfaatan purun tikus sebagai elektroda superkapasitor menggunakan aktivasi uap air. *J. Aceh Phys. Soc*, **7**(1), 30–34.
8. Awitdrus, A., Hanifa, Z., Agustino, A., Taer, E., & Farma, R. (2022). Perbandingan larutan elektrolit H2SO4 dan KOH pada kinerja elektrokimia bahan elektroda berbasis karbon aktif sabut kelapa muda. *Indonesian Journal of Industrial Research*, **12**(1), 15–20.
9. Qu, D. (2002). Studies of the activated carbons used in double-layer supercapacitors. *Journal of power sources*, **109**(2), 403–411.
10. Hanifa, Z. & Awitdrus, A. (2022). Pembuatan Elektroda Karbon dari Biomassa Sabut Kelapa Muda dengan Aktivator KOH Sebagai Aplikasi Sel Superkapasitor. *Indonesian Physics Communication*, **19**(1), 45–50.
11. Apriwandi, A., Taer, E., & Farma, R. (2021). Analysis of Cyclic Voltammetry dan Galvanostatic Charge Discharge Electrode Supercapacitor based on activated carbon from Kepok Banana Leaf (Musa balbisiana). *Journal of Aceh Physics Society*, **10**(4), 94–101.
12. Simanjuntak, M. T. & Awitdrus, A. (2022). Fabrikasi elektroda karbon dari sabut kelapa muda dengan aktivasi fisika sebagai aplikasi superkapasitor. *Indonesian Physics Communication*, **19**(2), 65–68.

IPC

Indonesian Physics Communication

Department of Physics, Universitas Riau, Pekanbaru, Indonesia
p-ISSN 1412-2960 | e-ISSN 2579-521X

Vol. 22 | No. 1
March 2025

Web: https://kfi.ejournal.unri.ac.id
E-mail: kfi@ejournal.unri.ac.id

Effect of coagulation and filtration in slow sand filters on iron absorption in groundwater

Ayu Cahyati*, Krisman
Department of Physics, Universitas Riau, Pekanbaru 28293, Indonesia

*Corresponding author: ayucahyati@gmail.com

ABSTRACT

The study was done to analyze the results of the filtration system of deep pearl housing groundwater using slow sand filtration methods. The analysis is based on the physical and chemical parameters of color/frequency, pH, iron and *Escherichia coli* with variations in coagulant, clay and alloy. The color/frequency of frequency before filtration has a value of 16.9 NTU, after value filtration declines 0.6%. The phasing of water before filtration was acid 6, having done filtration the pH of water down to 5.8 but had not reached a normal limit (6.5 – 8.5), so slow sand filters had not been effective in curbing the pH of water. The content of iron metals (Fe) before filtration was 0.1867 mg/l, after being made filtrating the content of iron metals (Fe) on the water was down to 0.021 mg/l. The content of *Escherichia coli* before filtration was 7 CFU / 100 ml, after exfiltration of the *Escherichia coli* content was reduced to zero CFU / 100 ml. The study suggests that slow sand filters use variations in coagulating and clay materials are effective in improving the quality of the groundwater in the high-yield housing projects.

Keywords: Clay; coagulation; groundwater; slow sand filter; soil water

Received 20-01-2023 | Revised 03-12-2024 | Accepted 08-03-2025 | Published 31-03-2025

INTRODUCTION

Water as a component of the environment will affect and be affected by other components. Poor quality water will result in a bad environment that will affect the health and safety of humans and other living things. Decreased water quality will reduce the utility, efficiency, productivity, carrying capacity and holding capacity of water resources which will ultimately reduce the wealth of natural resources [1].

The presence of iron (Fe) in water is available in dissolved conditions, ferrous (Fe^{2+}) and suspended, ferric (Fe^{3+}). This depends on the pH and dissolved oxygen conditions in the water. The presence of sufficient dissolved oxygen and neutral pH in water will oxidize Fe^{2+} to ($Fe(OH)_3$), where ($Fe(OH)_3$) is difficult to dissolve at neutral pH. Ferrous ions are often found in water sources that contain low dissolved oxygen such as groundwater and the bottom layer of lakes. The concentration of Fe in groundwater can reach around 1 – 10mg/1, while in surface water Fe levels exceeding 1 mg/1 are rarely found [2].

Acidity level (pH) is a physical parameter used to indicate the intensity of the acidic or basic state of a solution. Water is acidic if the pH is < 7, water with a pH value 7 is neutral, while pH > 7 is said to be basic [3]. The high or low pH of water does not affect health, but if water with a pH < 6.5 will cause corrosion of metals that dissolve toxic lead, copper, cadmium elements. Likewise, if the pH > 8.5 which is basic can form deposits (scale) on water pipes made of metal [4].

The pH of water will affect the iron content in the water, if the pH of the water is low it will cause corrosion which causes the dissolution of iron and other metals in the water and can result in the color of the water, causing the water to become colored, smelly and tasteless [2]. A pH meter is a tool for measuring pH, in addition to a pH meter, pH can also be measured using litmus paper [5].

Filtration is a water treatment process in which water is separated from colloids and

impurities, the number of bacteria is reduced and the chemical characteristics of the water change by passing it through a porous medium. Filtration is a water treatment process by flowing raw water through a filter media (porous layer) composed of granular materials with a certain diameter and thickness [6].

The Mentangor sub-district area is precisely in the Mutiara Tenayan Raya Housing (MTRH) complex, the community gets water resources from drilled wells managed by the housing complex. The water in the community's drilled wells is suspected of containing iron which has a negative impact when the community uses the water for a long period of time. As a result, the community is very disturbed by the negative impact on the water they use every day. The MTRH complex has oily and sedimentary water conditions, and the water is still used for daily needs. To find out whether the water meets the health requirements and clean water standards, an analysis is needed to determine the quality of groundwater in order to determine the exact cause of damage to the groundwater.

RESEARCH METHODS

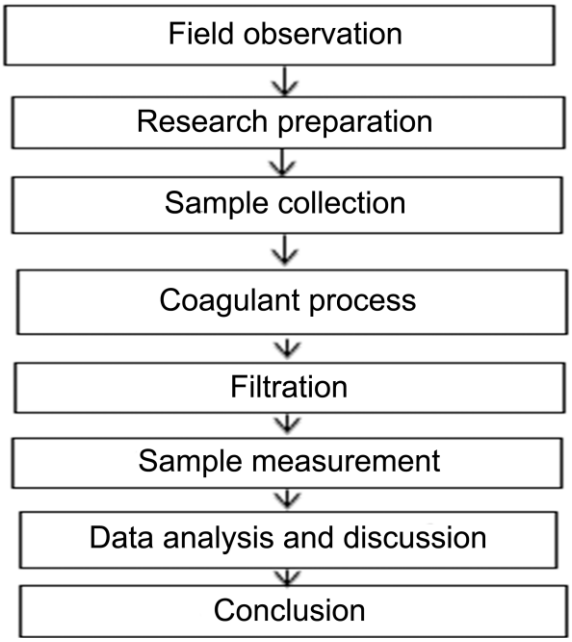

Figure 1. Research flow.

This research method (see Figure 1) begins with field observation to understand the context of the object being studied, followed by research preparation which includes planning the methodology and measuring instruments. Next, sampling is carried out from the target population to obtain representative data. The next process is coagulation, which may involve separating particles in the sample, followed by filtration to separate solid components from liquids or gases. After that, sample measurements are taken using measuring instruments according to research parameters. The measurement data are then analyzed in the data analysis and discussion stages, finally presenting a summary of the results and their implications in the conclusion stage, providing a comprehensive overview of important findings related to the initial hypothesis.

The samples used in this study were taken from the groundwater of MTRH which consisted of 4 sample points using GPS points. The first sample was taken in the south, the second sample was taken in the east, the third sample was taken in the north and the last sample was taken in the west with a distance of 100 m from the center point.

Then given treatment using a coagulation process with 3 variations of coagulants, namely alum, clay and a mixture of alum and clay using the slow sand filter method. The quality of water in this study was seen based on physical and chemical parameters, namely color/turbidity level, pH, heavy metal content of iron (Fe) and *Escherichia coli*.

RESULTS AND DISCUSSION

Color/Turbidity Level of Groundwater of MTRH Residents with Slow Sand Filter Filtration

The groundwater of MTRH is located on clay soil and has a clear color/turbidity level but will change color to yellowish if left for several hours. One of the requirements for good water quality is that the water is colorless. The results of the study on the turbidity of groundwater in MTRH through the coagulation process and using the slow sand filter method before and after filtration are shown in Figure 2.

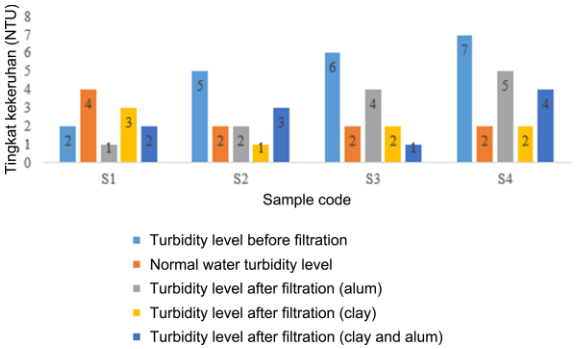

Figure 2. Graph of the color/turbidity level of well water in MTRH before and after filtration using slow sand filters.

Figure 2 shows the color/turbidity level of water before and after filtration using slow sand filters and variations in coagulation of alum, clay and mixtures. The highest value before filtration is in the fourth sample, which is 7 NTU which has a more yellow color because the fourth sample is located very close to the cliff land where there are no residential areas, the lowest value is in the first sample, which is 2 NTU. The decrease in color parameters is due to the addition of coagulants which produce chemical reactions where the negative charges that repel each other around the colloidal dissolved particles will be neutralized by the positive ions from the coagulant and the colloidal particles will attract each other and clump together to form flocs.

Groundwater pH Value of MTRH with Slow Sand Filter Filtration

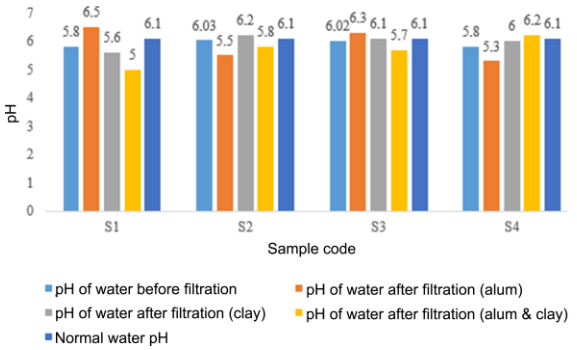

Figure 3. Graph of pH values before and after filtration using variations of alum, clay and mixed coagulants.

Figure 3 shows the pH values before and after filtration using alum, clay and mixed coagulants. The pH value before filtration in sample S1 was 5.8, S2 was 6.03, S3 was 6.02 and S4 was 5.8. The results of the values after filtration using alum coagulant increased and decreased in each sample. The first and third samples increased by 6.5 and 6.3 while the second and fourth samples decreased by 5.5 and 5.3. The results of the values after filtration using clay coagulant increased in the fourth sample by 6 while the first, second and third samples decreased by 5.6, 6.2, and 6.1. The results of the values after filtration using a mixture of alum and clay coagulants have decreased values in the first, second and third samples, namely 5, 5.58, and 5.7, while in the fourth sample there was an increase of 6.2.

Heavy Metal Concentration Content of Iron (Fe) in Groundwater of MTRH with Slow Sand Filter Filtration

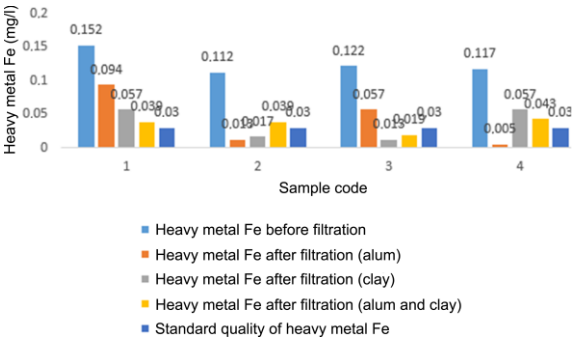

Figure 4. Graph of heavy metal content of Fe in groundwater of MTRH before and after filtration using a variety of coagulants.

Figure 4 shows the concentration value of iron metal (Fe) before and after filtration using a slow sand filter along with variations in alum, clay and mixed coagulants. Before filtration in sample S1 it was 0.152 mg/l, S2 was 0.112 mg/l, S3 was 0.122 mg/l, and S4 was 0.117 mg/l. Sample S1 before filtration has the highest iron (Fe) content of 0.152 mg/l because sample S1 before filtration was very new so that the iron content in the water was very high. After being filtered using a variety of coagulants, the value of each sample decreased by 0.094 mg/l to 0.005 mg/l.

***Escherichia coli* Content of Groundwater in MTRH with Slow Sand Filter Filtration**

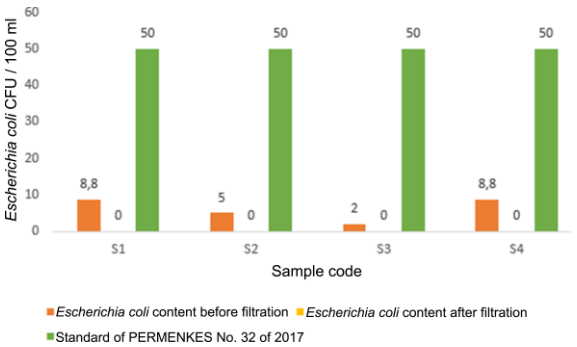

Figure 5. Graph of *Escherichia coli* content of groundwater in MTRH with slow sand filter filtration.

Figure 5 shows the *Escherichia coli* content before and after filtration using a slow sand filter. The *Escherichia coli* content before filtration had values of 8.8, 5, 2, and 8.8 CFU/100ml respectively and were still below the threshold set by PERMENKES, No. 32 of 2017 amounting to 50 CFU / 100 ml. After filtration using the slow sand filter method, the E-Coli content value decreased by 0 CFU / 100 ml.

CONCLUSION

Groundwater of MTRH when filtered using slow sand filter on alum coagulant, clay and mixture has different treatment so that different results are obtained. In each sample, alum coagulant is inserted for 3 to 10 minutes until sediment is seen at the bottom of the water tank used as a filter or catcher of fine particles in the water and replaces it with sediment that helps the groundwater filtration process. While clay functions to reduce toxins in the water.

The parameter value of heavy metal (Fe) sample S1 is 0.152 mg/l, sample S2 is 0.112 mg/l, sample S3 is 122 mg/l and sample S4 is 117 mg/l. Sample S1 before filtration has the highest iron metal (Fe) content of 0.152 mg/l because sample S1 before filtration the water condition is very new so that the iron content in the water is very high. The results of this study indicate that the *Escherichia coli* parameter value and the heavy metal parameter value of iron (Fe) decreased after slow sand filter filtration with variations of alum and clay coagulants, compared to the pH value which only increased and decreased in each sample due to the addition of high levels of alum, if dissolved it will reduce the pH level in water.

ACKNOWLEDGMENTS

Thanks are due to the Directorate General of Higher Education, Ministry of Education and Culture (Kemendikbud), Institute of Education and Community Service (LPPM), University of Riau and the Author's Parents who have facilitated the implementation of this research.

REFERENCES

1. Kusnoputranto, H. (1997). *Pengantar kesehatan lingkungan*. Jakarta: Direktorat Jenderal Pendidikan Tinggi Departemen Pendidikan dan Kebudayaan.
2. Rahman, A. & Hartono, B. (2004). Penyaringan air tanah dengan zeolit alami untuk menurunkan kadar besi dan mangan. *Makara Kesehatan*, **8**(1), 1–6.
3. Effendi, H. (2003). *Telaah Kualitas Air: Bagi Pengelolaan Sumber Daya dan Perairan*. Indonesia: PT Kanisius.
4. Sudadi, P. (2003). Penentuan kualitas air tanah melalui analisis unsur kimia terpilih. *Buletin Geologi Tata Lingkungan*, **13**(2),
5. Mahida, U. N. (1986). *Pencemaran dan pemanfaatan limbah industri*. Jakarta: Rajawali Press.
6. Huisman, L. & Wood, E. W. (1974). *Slow sand itration*. Geneva: World Health Organixation.

IPC

Indonesian Physics Communication

Department of Physics, Universitas Riau, Pekanbaru, Indonesia
p-ISSN 1412-2960 | e-ISSN 2579-521X

Vol. 22 | No. 1
March 2025

Web: https://kfi.ejournal.unri.ac.id
E-mail: kfi@ejournal.unri.ac.id

Interpretation of groundwater potential based on the Cooper Jacobs method combined with Schlumberger geoelectricity in Simpang Tiga Village, Pekanbaru City

Joko Kurniawan*, Juandi Muhammad
Department of Physics, Universitas Riau, Pekanbaru 28293, Indonesia

*Corresponding author: joko.kurniawan@unri.ac.id

ABSTRACT

This study aims to analyze the aquifer parameter values including storativity, transmisivity, and hydraulic conductivity in Simpang Tiga Village, Pekanbaru City. This research is motivated by the community's increasing need for water due to higher population growth, and the Simpang Tiga Village which is close to the city center. Pumping test results using the Cooper Jacobs method showed an aquifer transmisivity value of 247.21 m^2/day in the high category and a storativity value of 0.0845. The results of the geoelectrical test with the Schlumberger configuration obtained that the aquifer layer is in the fourth layer with a thickness of 11 m. The hydraulic conductivity obtained is 22.473 m/day and is included in the fast category.

Keywords: Aquifer; hydraulic conductivity; storativity; transmissivity; underground water

Received 21-01-2023 | Revised 10-12-2024 | Accepted 06-03-2025 | Published 31-03-2025

INTRODUCTION

Water is the most needed resource for the survival of life, be it for humans, animals, or plants, all need water for their survival. The availability of water on earth is very limited both in terms of the availability of storage space, time, quality and quantity [1]. An aquifer is a geological formation that can store and pass water in large quantities. The water stored in this aquifer is called groundwater [2].

The activity of finding and utilizing groundwater to meet both domestic and industrial needs, it is necessary to know the geometric structure or characteristics of the water-bearing layer below the surface. One approach taken to investigate the potential of aquifers for groundwater exploitation is by analyzing pumping test data. Pumping tests are carried out to measure the value of the decrease in the groundwater level, which is produced from the pumping process in the well [3]. The pumping test data can then be analyzed using statistical models such as the Cooper Jacob to determine the aquifer parameters [4].

The Simpang Tiga sub-district area is the area with the lowest population density in the Bukit Raya sub-district with a figure of 2116 residents/km^2 of its area. However, its location which is not far from the city center will certainly accelerate progress in the sub-district. Currently, one star-rated hotel and a BPR bank have been recorded in this sub-district. With the growth of industry, economy, and population density growth, of course, it will be directly proportional to the increasing amount of water needed. In this case, the policy of exploration and exploitation of water properly is needed so that the water in this sub-district remains fulfilled but does not burden the aquifer in the area. Investigating the characteristics of the aquifer in this sub-district is important to do. One way is to conduct a pumping test using the Cooper Jacobs method and combined with the Schlumberger configuration geoelectric method so that the aquifer parameters are obtained.

LITERATURE REVIEW

Groundwater

Groundwater is different from soil water. Groundwater is water that is in the aquifer layer

or saturated zone. While soil water is water that is in the unsaturated zone.

Aquifer

An aquifer is a geological formation that is saturated so that it can be used as a supplier of water in economical quantities because this formation is able to store and pass water. Todd (1955), stated that etymologically aquifer comes from Latin, namely from the word aqui or aqua which means water and the word ferre which means to carry, so etymologically aquifer can be interpreted as a water-bearing layer [5].

Aquifer Characteristics

An aquifer is a geological formation that is able to store and carry water which is very useful for human life needs. However, the ability to store or carry water for each aquifer in each place is different. This ability is influenced by the type of rock that makes up the aquifer. Some characteristics or parameters of aquifers that determine the potential for groundwater in an aquifer include hydraulic conductivity, transmissivity, and storativity.

Hydraulic conductivity can be defined as a coefficient value that indicates the ability of rocks to pass unit volumes of water along permeable media through pore cavities in unit time. Transmissivity is the ability of an aquifer to pass or transmit water through a vertical plane as thick as an aquifer with a width of one unit length and one unit hydraulic gradient. Storativity is a coefficient that indicates the volume of water that can be released or stored by an aquifer area per unit change in the position of the groundwater table.

RESEARCH METHODS

The research method (see Figure 1) begins with a literature study to understand the relevant theories, followed by a field survey to collect initial data on the location. Next, field data collection was carried out through direct measurements and geoelectric experiments to obtain information about the subsurface structure of the land. Pump tests were carried out to evaluate the characteristics of the aquifer, after which the data obtained were processed using the Cooper-Jacobs method to determine parameters such as transmissivity and storativity. Interpretation of the aquifer layers was carried out using special software (Progress Software), where hydraulic conductivity was calculated as a measure of the soil's ability to conduct water. Finally, all data were thoroughly analyzed and conclusions were drawn based on the findings of the entire research process.

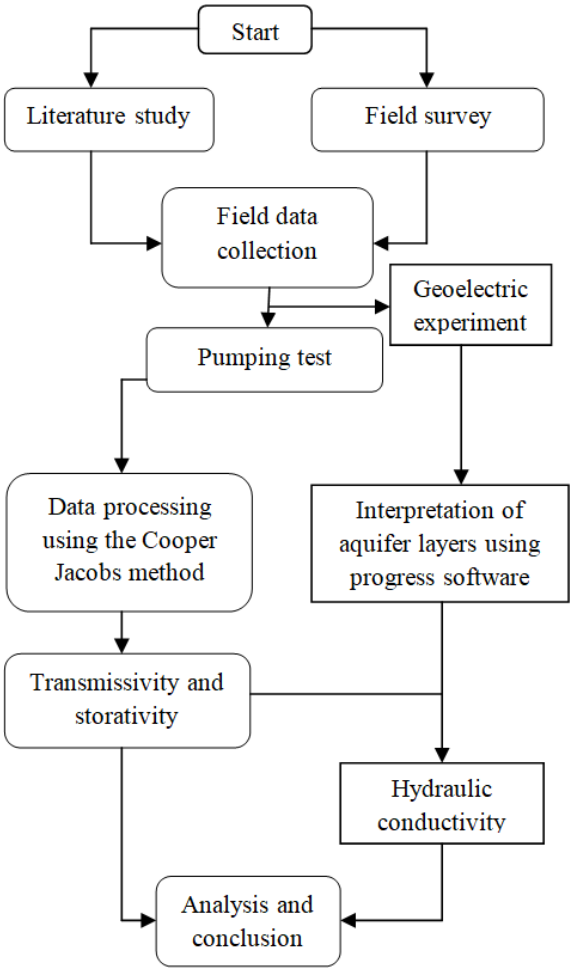

Figure 1. Research flow.

RESULTS AND DISCUSSION

This research was conducted in two stages, the initial stage of the pumping test. The pumping test was conducted with a constant discharge of Q = 0.005625 m^3/s and the distance between the test well and the

monitoring well was 5.4 m. The pumping test data was then plotted into a semi-log graph and the results were as follows Figure 2.

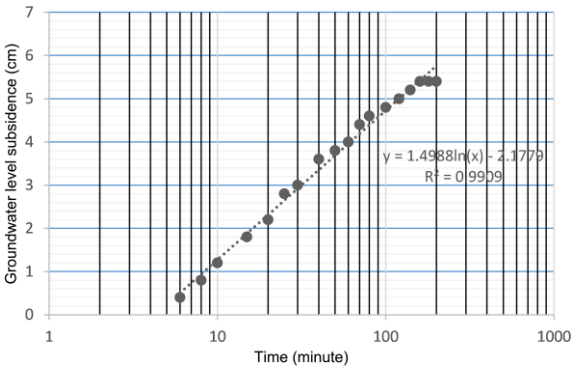

Figure 2. Semilog graph s vs t.

Based on the graph, the decrease in groundwater level during one log period Δs = 3.6 cm and the line equation s = 1.4988 ln (t_0) – 2.1779. From this line equation, t_0 can be calculated when s = 0 as follows:

s = 1.4988 ln (t_0) – 2.1779
0 = 1.4988 ln (t_0) – 2.1779
t_0 = 4.28 minutes = 0.00297 days

Furthermore, the aquifer transmissivity value can be calculated as follows:

$T = (2.3 \times Q) / (4 \times \pi \times \Delta s)$
$T = (2.3 \times 0.0005625) / (4 \times 3.14 \times 0.036)$
$T = 0.002861\ m^2/s$
$T = 247.21\ m^2/day$

Based on the calculation results, the transmissivity of the aquifer layer in the Simpang Tiga sub-district, Pekanbaru city is 247.21 m^3/day. From the transmissivity coefficient value obtained, the aquifer in the Simpang Tiga sub-district, Pekanbaru city has a high category of transmissivity value, with groundwater potential for smaller important areas, and an estimated water discharge of 5 – 50 liters/s. Furthermore, the aquifer storativity can be calculated as follows:

$S = (2.25 \times T \times t_0) / r^2$
$S = (2.25 \times 247.21 \times 0.00297) / (5.4)^2$
$S = 0.0566$

Based on the calculation above, the aquifer storativity in the Simpang Tiga sub-district, Pekanbaru city is 0.0566. The size of the aquifer storativity affects the depression of the groundwater table due to pumping. Aquifers with large storativity, the depression of the groundwater table will tend to be smaller and its influence is also not extensive, conversely aquifers with small storativity, the depression of the groundwater table due to pumping tends to be larger and its influence is wider.

The second stage of the research is to conduct a Schlumberger configuration geoelectric experiment. The geoelectric path data obtained in the field is then processed using Microsoft Excel to obtain the geometry factor and apparent resistivity values, then processed using Progress 3.0 Software to interpret the layer material below the path. The results of the appearance of subsurface material along the path as seen in the following image:

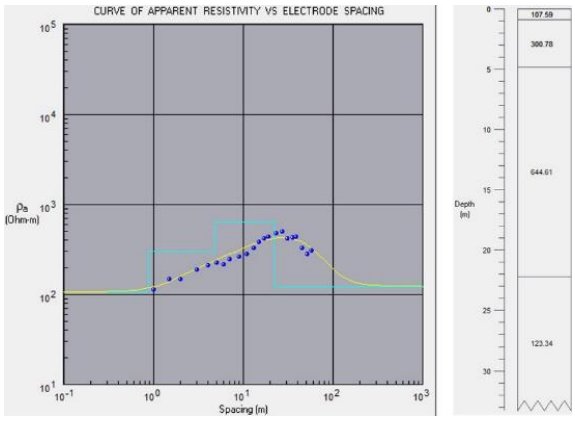

Figure 3. Schlumberger configuration geoelectric path data graph.

The image (see Figure 3) above explains the subsurface conditions along the path. The depth of the layer read by Progress Software is 33 m, with an RMS error value of 12.10%. The first layer of the subsurface with a thickness of 1 m has a resistivity value of 107.59 Ωm, which can be interpreted as the first layer containing sand, the second layer with a thickness of 4 m has a resistivity value of 300.78 Ωm, which can be interpreted as the second layer containing sandstone.

The third layer obtained a resistivity value of 644.61 with a layer thickness of 18 m, the third layer is interpreted as containing rock and sand, the fourth layer with a thickness of 11 m and a resistivity of 123.34, this fourth layer is interpreted as an aquifer or layer containing groundwater.

Based on the transmissivity and thickness of the aquifer, the hydraulic conductivity of the aquifer can be calculated as follows:

K = T / D
K = 247.21 / 11
K = 22.473 m/day

Based on the calculation results, the hydraulic conductivity value was obtained as 22.473 m/day. These results explain that the aquifer has a fast hydraulic conductivity category, and show that the rocks that make up the aquifer are hard sand and/or sand mixed with gravel.

CONCLUSION

The results of the pumping test using the Cooper Jacob method obtained an aquifer transmissivity of 247.21 m^2/day so that it is included in the category of aquifers with high transmissivity, and a storativity of 0.0566. The results of resistivity measurements in Simpang Tiga Village, Pekanbaru City with Progress Software show that the aquifer is in the fourth layer at a depth of 22 m, with a thickness of 11 m, and a resistivity value of 123.34 ohm-meters. The hydraulic conductivity value is 22.473 m/day so that the hydraulic conductivity of the aquifer is included in the fast category.

ACKNOWLEDGMENTS

Thanks are due to the Directorate General of Higher Education, Ministry of Education and Culture (Kemendikbud), Institute of Education and Community Service (LPPM), University of Riau and the Author's Parents who have facilitated the implementation of this research.

REFERENCES

1. Bouwer, H. (1978). *Groundwater hydrology*. Int. Student Ed. McGraw-Hill Kogakusha Ltd.
2. Purnama, S. (2000). *Bahan ajar geohidrologi*. Yogyakarta: Fakultas Geografi UGM.
3. Maliva, R. G. (2016). *Aquifer characterization techniques*. New York: Springer.
4. Kasenow, M. (2001). *Applied ground-water hydrology and well hydraulics*. Water Resources Publication.
5. Todd, D. K. (1980). *Groundwater hydrology*. New York: Jhon Wiley & Sons.